INVESTIGATIONS OF THE PHOTOPHYSICAL PROPERTIES OF FLUORESCENT PROTEINS AND THEIR IMPLICATIONS FOR ANALYSIS OF FÖRSTER RESONANCE ENERGY TRANSFER MEASUREMENTS

by

Dhruba Prasad Adhikari

A Dissertation Submitted in

Partial Fulfillment of the

Requirements for the Degree of

Doctor of Philosophy

in Physics

at

The University of Wisconsin-Milwaukee

May 2024

ABSTRACT

INVESTIGATIONS OF THE PHOTOPHYSICAL PROPERTIES OF FLUORESCENT PROTEINS AND THEIR IMPLICATIONS FOR ANALYSIS OF FÖRSTER RESONANCE ENERGY TRANSFER MEASUREMENTS

by

Dhruba Prasad Adhikari

The University of Wisconsin-Milwaukee, 2024
Under the Supervision of Professor Valerică Raicu

Understanding the photophysical properties of fluorescent proteins (FPs), such as emission and absorption spectra, molecular brightness, photostability, and photoswitching, is critical to the development of criteria for their selection as tags for fluorescence-based biological applications. My overall goal has been to study the photophysical properties of FPs under various excitation conditions, quantify the contributions that photophysical effects make to Förster resonance energy transfer (FRET) measurements, and provide appropriate experimental guidelines for FRET studies.

Over the past two decades, we have witnessed a mounting interest in the study of protein localization and interactions using two-photon excitation (TPE) of fluorescently labeled proteins. While there is a plethora of information available regarding the photophysical and photochemical properties of commonly used fluorescent proteins when subjected to single-photon excitation, unfortunately, there is still very limited information regarding these properties under TPE. Therefore, I started my research by investigating the photophysical properties of several widely used fluorescent proteins using two-photon microscopy with

spectral resolution in both excitation and emission. The results provided in the first part of this dissertation indicate that a number of properties, including the excitation and emission spectra, the relative brightness, and the extent of photobleaching and photoswitching, are markedly different under TPE when compared to single-photon excitation.

The second part of this dissertation describes a detailed study of the nature and degree of the contributions to FRET of the photophysical effects exhibited by FPs used as fluorescent tags for the proteins of interest. FRET is a widely used technique to study the quaternary structure of protein complexes (i.e., intermolecular distances and binding interfaces) in living cells. Critical to the interpretation of the results of such studies is the theoretical treatment of oligomers comprised of more than one donor and one acceptor that may exchange electronic excitations via FRET. The question has been theoretically addressed by developing the kinetic theory of FRET. However, there is no detailed analysis how FRET and the kinetic theory of FRET respond to photophysical effects such as photobleaching of the donor and acceptor tags. Herein, we have presented a comparative analysis of different protocols for calculation of the FRET efficiency. We studied the effects of changing the laser excitation power on FRET measurements by quantifying the deviations from the kinetic theory of FRET, which does not include photobleaching currently. We also used a simple but effective numerical method to estimate the degree to which photobleaching of donors and acceptors was responsible for the observed discrepancies between the two sets of FRET efficiencies. We found that under low excitation power, and with carefully selected excitation wavelengths, the FRET efficiency of an obligate trimeric construct, made by fusing one FRET donor and two FRET acceptors to one another, is in agreement within less than 2% with the FRET efficiency predicted by the kinetic theory of FRET. However, at higher excitation powers, the FRET efficiencies changed

significantly, due to the photobleaching of both the donor, through direct excitation, and the acceptor, mostly through FRET-induced excitation.

If ignored, these effects could cause systematic and random errors as large as 15% or more in the FRET efficiency values obtained from experiments, which would cause significant uncertainties regarding the quaternary structure to be determined. This study therefore provides critical information for selecting appropriate fluorescent proteins and experimental conditions for reliable FRET measurements in oligomeric complexes of associating molecules in living cells.

Dedicated with love,

to my family

TABLE OF CONTENTS

LIST OF FIGURES

LIST OF TABLES

ACKNOWLEDGEMENTS

Foremost, I would like to express my profound gratitude to Professor Valerică Raicu, my advisor, for his constant support and guidance throughout my Ph.D. study and research. From the very beginning, he encouraged me to learn thoroughly, if possible, by starting with manual data analysis, which helped me grasp the subtle knowledge and come up with better ideas for automatic protocols and spot any flaws. He has motivated me to come out of my comfort zone and try new challenges. It has been a great honor to be his student. I am genuinely grateful to have him as my mentor, to complete my Ph.D. under his exceptional advisory and supervision. His immense knowledge, motivation, and care shaped the path for my successful research and study. Without his persistent help and guidance, I would not be an experimentalist with sufficient theoretical skills.

Also, I am hugely thankful to Dr. Michael Stoneman and Dr. Gabriel Biener, with whom I got the opportunity to learn and enhance my skills in every step of research. They have provided me with their support and help to get the correct way out when there were unsolved questions and confusion. I truly appreciate their time and help. They have been my ideal figures who motivated me on the path to becoming a better scientist.

Moreover, I would like to thank Prof. Popa for the great opportunity to work with him and the constant support and guidance he provided me during our collaborative single-molecule project. As part of this, I have not only learned the complex analytical methods of single-molecule detection, but also developed algorithms for image data processing tools. I would also like to extend my deepest appreciation to my committee members: Prof. David Frick, Prof. Marius Schmidt, and Prof. Peter Schwander who have been immensely supportive with their

constructive suggestions and feedback. I am very thankful for their valuable time and support they have given me in assessing my research and providing helpful insights.

Additionally, I would like to thank Prof. Paul Park (Case Western Reserve University) who has contributed his time and support during one of my collaborative projects. I would like to acknowledge Annie Eis, who, although no longer with us, trained me as well as shared materials and knowledge for protein purification process.

I also wish to express my heartfelt appreciation to colleagues/friends within the lab, Joel David Paprocki and Dammar Nath Badu for being helpful and supportive during research works; Justin Anthony Trujillo, Aliyah Sephrah Khan, Sadia Rahman, and Thomas David Killeen for the scientific talks and for being wonderful friends. I would like to thank Sabita Sharma and Dr. Smrithika Subramani for their help and support during the collaborative research. Also, I would like to say thank you to my colleagues Ishwor, Netra, Suraj, Manish, Narayan, Naresh, Sanam, Tek, Rabin, Prabin, Sishir, and Chetanath for being wonderful friends. I am thankful for the opportunity to learn and grow together with all of them.

Furthermore, I am grateful to the Department of Physics University of Wisconsin Milwaukee, which provided me with scholarships and a great platform to pursue my education and research work in the field of Biophysics. I would like to thank our administrative staff, Steve Kennedy, Kate Valerius, Reba Sinha, Linda Randolph, and Elle Cochrane for being cooperative and supportive and for their help during this journey.

Finally, I extend my heartfelt gratitude to my parents and siblings for their unwavering support and motivation throughout this journey. Last but not least, I am deeply thankful for my wife, Darshan Subedi, whose caring and supportive presence has been a constant source of strength, accompanying me through every challenge and triumph of this journey.

Chapter 1. Introduction

After the discovery of the wild-type green fluorescent protein (wtGFP) from the jellyfish *Aequorea Victoria* [1], researchers have engineered a significant palette of wtGFP variants [2], which possess diverse color characteristics, i.e., wavelength-shifted absorbance and/or emission spectra as well as other photophysical properties such as quantum yield and excitation coefficient. In addition to those proteins which have been derived from *Aequorea Victoria,* there are many other fluorescent proteins (FPs) with different spectral properties have been isolated from other species, e.g., Anthozoa corals [3] and Clavularia coral [4]. The continued development of this vast array of FPs has made fluorescence imaging one of the foremost techniques in cell biology research.

Access to a large FP library with many different spectral variants has enabled researchers to continuously develop and refine advanced fluorescence-based techniques for the study of complex biophysical and biochemical processes. As such, those methods that rely on Förster resonance energy transfer (FRET) have proved to be very effective in probing protein-protein interactions in living cells [5-7]. A more recent addition to the family of FRET methods, FRET spectrometry [8, 9], can estimate the size and geometrical parameters of the underlying quaternary structure of the receptor of interest [6, 10]. In such applications, FPs with different spectral properties [11-14] help advance life science research by allowing researchers to judiciously choose suitable FPs to minimize technical hurdles that may arise in their particular application.

The main objective of this chapter is to establish a general background for the research presented in this dissertation, which ultimately focuses on the photophysical effects of FPs and their implication in FRET studies. This chapter presents a brief overview of the green

fluorescent protein and its structure, along with the development of variants of the green fluorescent protein and analogous fluorescent proteins derived from different species. In addition, the basic principles underlying the concepts of fluorescence and Förster resonance energy transfer (FRET) are presented.

1.1. Green fluorescence protein (GFP)

The green fluorescent protein (GFP) was discovered by Shimomura et al. [1] as a chemiluminescent protein from the jellyfish Aequorea Victoria. In exposure to blue or violet light, GFP exhibits green fluorescence. Along with the discovery of the GFP, the same group confirmed that the emission spectrum of GFP has a peak at 508 nm. In 1979, the first chemical structure model of the fluorophore in Aequorea GFP was proposed by isolating the fluorophore and analyzing its components [15]. Later, a modified chemical structure model of the fluorophore in Aequorea GFP was proposed by Ward et al. [16] and Cody et al. [17], which confirmed that the functional portion of the chromophore is a 4-(p-hydroxybenzylidene)-5-imidazolidine. Following those discoveries, the widespread use of this molecule was triggered by the cloning [18] and demonstration of heterologous expression, i.e., expression in different species [19], which confirmed that GFP could be used as a marker of gene expression and protein localization in living cells [20-22]. The heterologous expression suggested that GFP could be mutated to produce FPs with different fluorescence properties, for example, fluorescence intensity, photostability, and shifted excitation and emission spectra.

1.1.1. Crystal structures of GFP

The crystal structure of GFP was first revealed in 1996 by Ormö et al. [23] using the techniques such as multiple isomorphous replacements and anomalous scattering. Their approach involved utilizing solvent flattening, phase combination, and crystallographic refinement to improve experimental electron density maps. The three-dimensional structure of GFP consists of 11 stranded β-sheets wrapped around a single central helix forming a nearly perfect cylinder of 24 Å diameter and 42 Å long [23]. The chromophore p-hydroxybenzylidene-5-imidazolidine is located centrally inside the cylinder, as shown in figure 1.1.

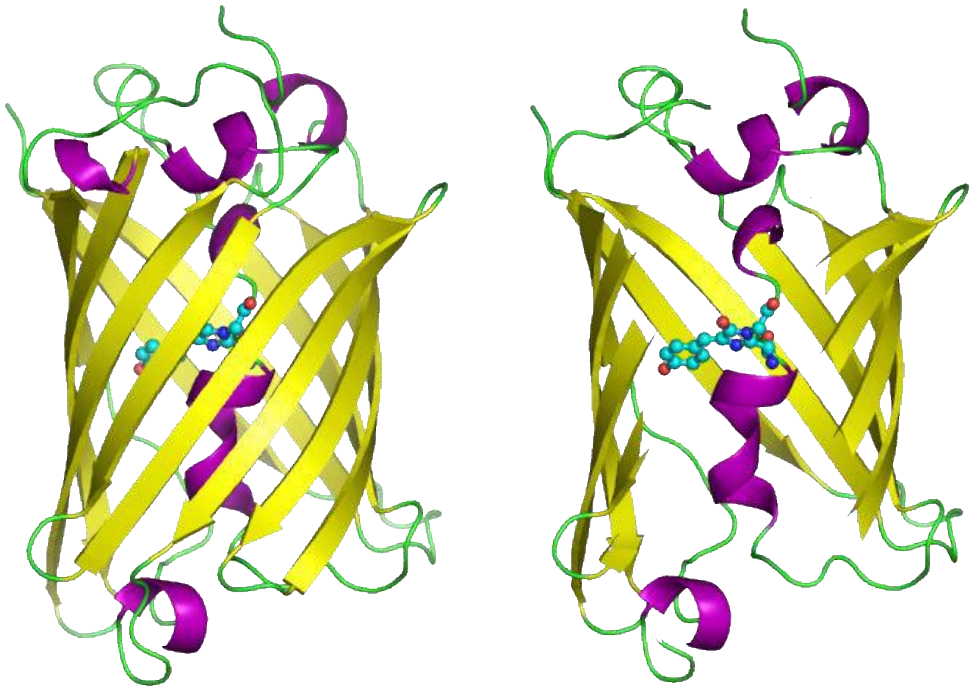

Figure 1.1. Stereo-view of the three-dimensional structure of GFP. The image on the left represents the structure of GFP with a fluorophore at the center of the hollow cylindrical structure. The image on the right is the same image on the left with a cut-away portion β-sheet to show central fluorophore distinctively. The β-sheets are represented with the yellow ribbons and α-helices are represented with pink helices, respectively. The centrally located multicolor ball-and-sticks represent the chromophore. The figure is adapted from Wikipedia at https://en.wikipedia.org/wiki/Green_fluorescent_protein.

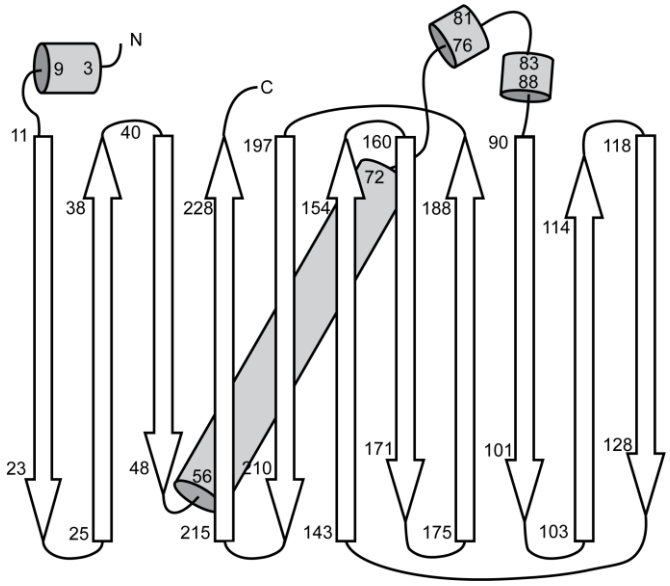

Figure 1.2. Schematic representation of the overall fold of GFP and position of amino acids. The structure comprises 11 stranded β- sheets, each consisting of approximately 9 to 13 residues. The number marks at the base and arrowhead of each strand give beginning and ending amino acid residue number of that strand. The diagonal cylinder extending from amino acid number 56 to 72 represents the central alpha-helix that contains the chromophore-peptide of the GFP. The three helices on the top end of the β-sheet are represented with short cylinders. Figure is adapted from Ormö et al. [23].

1.1.2. Chemical structure of chromophore in GFP

The chromophore, responsible for the green fluorescence of Aequorea green fluorescent protein (AGFP), is formed from the primary amino acid sequence of the protein and located at the center of the β- sheet. The first chemical structure model of the chromophore (i.e., the model structure of fluorophore sequence) in AGFP was proposed by Shimomura et al. [15]. According to Shimomura et al., the core of AGFP chromophore was identified as a substituted 4-p-hydroxy-benzylidene-5-imidazolidine based on amino-acid component analysis of fluorophore-containing peptide and the comparison of the absorption spectra of the peptide [15, 24]. Later, a modified chemical structure model of the chromophore in AGFP was proposed by

Cody et al. [17], which confirmed the structure, but modified the overall structure of the chromophore peptide as in figure 1.3.

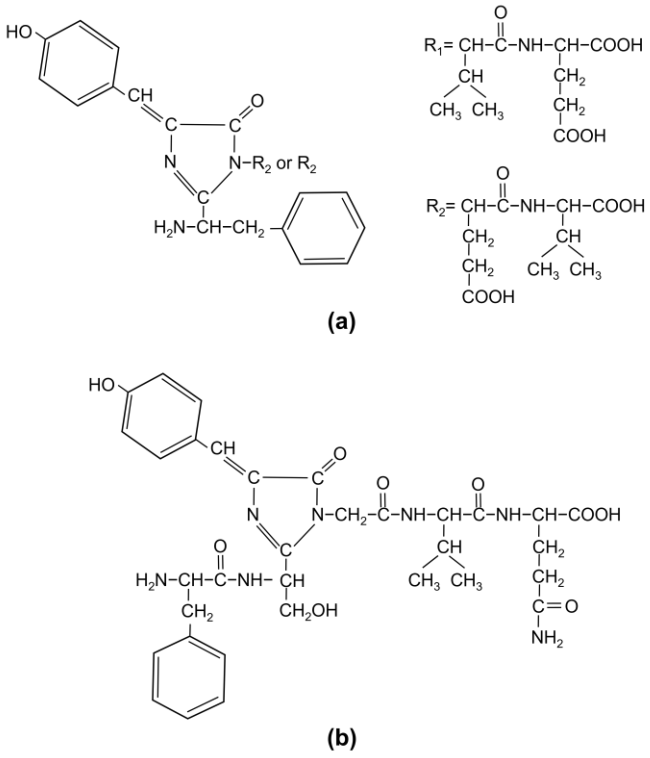

Figure 1.3. Proposed structure of the chromophore peptide of AGFP: (a) from Shimomura [15]; (b) from Cody et al. [17].

Later, Tsien's lab reported [23, 25, 26] that the autocatalytic chromophore formation in AGFP is oxygen-dependent and proposed the biosynthetic scheme for chromophore formation shown in Figure 1.4. According to Tsien [2], first, AGFP folds into a nearly native conformation, then the imidazoline is formed by nucleophilic attack of the amide of Gly67 on the carbonyl of residue 65, followed by dehydration. Finally, molecular oxygen dehydrogenates the α-β bond of residue 66 to put its aromatic group into conjugation with the imidazolinone. At this stage, the chromophore acquires visible absorbance and fluorescence [2].

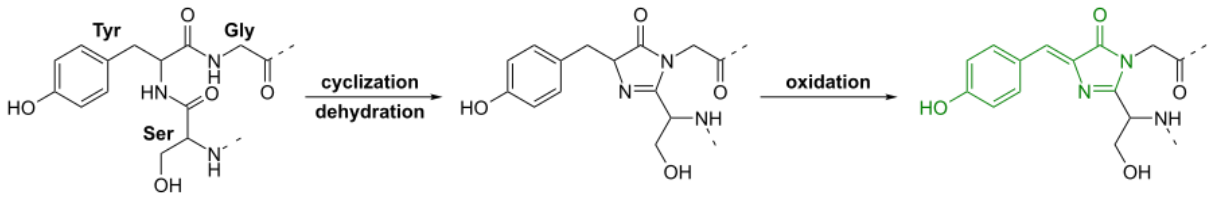

Figure 1.4. Schematic representation of the chromophore formation in AGFP. The cyclization of the carboxyl carbon of the Ser65 followed by dehydrogenation reactions at the Tyr66 residue results in the formation of the imidazoline-5-one ring. Thereafter, oxidation of the tyrosine (Tyr66) α-β carbon bond by molecular oxygen causes the occurrence of fluorescence in AGFP. Figure adapted from https://www.wikiwand.com/en/Green_fluorescent_protein.

1.1.3. Spectral characteristics of GFP

AGFP has two absorption maxima: major at about 395 nm and minor at 475 nm [27]. The excitation at the primary absorption peak of 395 nm gives an emission maximum at 508 nm with a quantum yield of 0.72 to 0.85 [1, 23, 26, 28]. The spectral properties of the AGFP can be affected by concentration, temperature, and the ionic strength of its environment (pH) [16]. Self-association is favored at higher concentrations resulting in amplification of absorption peak at 395 nm and suppression of the 477 nm absorption shoulder. The peaks at 395 nm and 477 nm correspond to the neutral and anionic states of the fluorophores, respectively. As such, in a neutral aqueous buffer solution, AGFP lost half of the fluorescence at the temperature of 78^{o}C. Increasing temperature from 15 to 65 ^{o}C decreases the excitation amplitude at 395 nm and increases the excitation amplitude at 477 nm [16], whereas, at high pH AGFP loses absorbance and excitation amplitude at 395 and gains amplitudes at 477 nm [16]. The emission spectrum, i.e., the fluorescence intensity of AGFP measured as a function of wavelength when the excitation wavelength is fixed, and the absorption spectrum of AGFP is shown in figure 1.5.

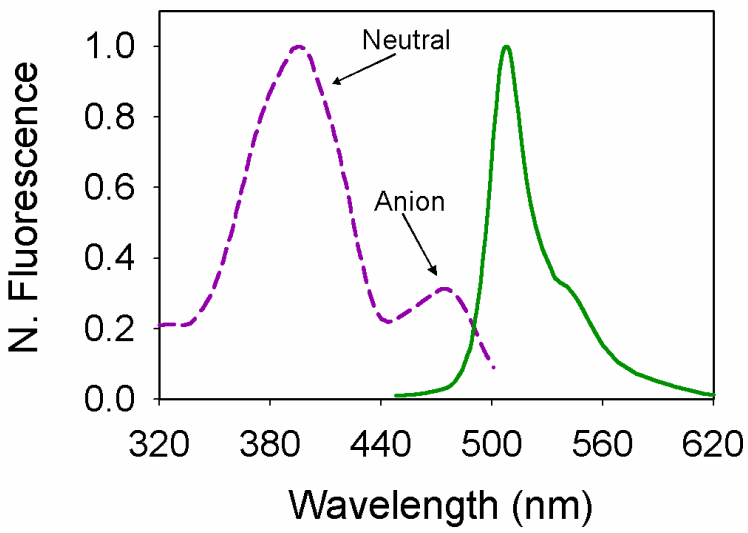

Figure 1.5. Absorption spectrum (dashed line) and emission spectrum (solid line) of AGFP. The adsorption spectrum of AGFP has a major peak at 395 nm and a minor peak at 477 nm, which correspond with a protonated (neutral) chromophore and a deprotonated (anion) chromophore.

1.2. Variants of GFP and associated mutations

With the expansion of the fluorescence technique, scientists have been able to modify elements of the chromophore yielding a wide variety of mutations that create opportunities for researchers to assemble compatible fluorescent proteins for their potential application. Most of the mutations are designed to obtain shifted emission and excitation spectra and improved intensity; however, they are sometimes also designed for different pH sensitivity, dimerizing or non-dimerizing modifications, etc. The main goal of these mutated fluorescent proteins is to provide appropriate fluorescent markers for the desired measurements. In the case of GFP, the hydrogen-bonding network and electron-stacking interactions with the sidechains of the barrel influence the color, intensity, and photostability of GFP and its various derivatives [29].

1.2.1. Variants for shifted emission and excitation wavelengths

A broad range of GFP variants was created with fluorescence emission ranging from blue to yellow regions of the visible spectrum. For example, enhanced green fluorescent protein (EGFP) is a widely used variant of GFP, which contains two-point mutations: Ser65 to Thr (S65T) and Phe64 to Leu (F64L) [25, 30]. These changes in the GFP coding sequence reduce the excitation spectrum from a major peak at 395 nm and a minor peak at 477 nm to a single peak at 488 nm. The mutations result in an enhanced GFP, which is 35 times brighter than wild-type GFP with relatively more stable molecular brightness [31].

Yellow mutants of the green fluorescent protein (YFP) are another group of GFP variants created by mutating Thr203 in the *Aequorea victoria* green fluorescent protein (GFP) [2]. With that mutation, the resulting π-π stacking and increased local polarizability adjacent to the chromophore are believed to be responsible for the ~20 nm shift to longer excitation and emission wavelength [32]. However, the changes due to the internal hydrogen bonding and electron stacking also made the fluorescent protein vulnerable to photobleaching [33, 34] and photoswitching by protonation [35-37].

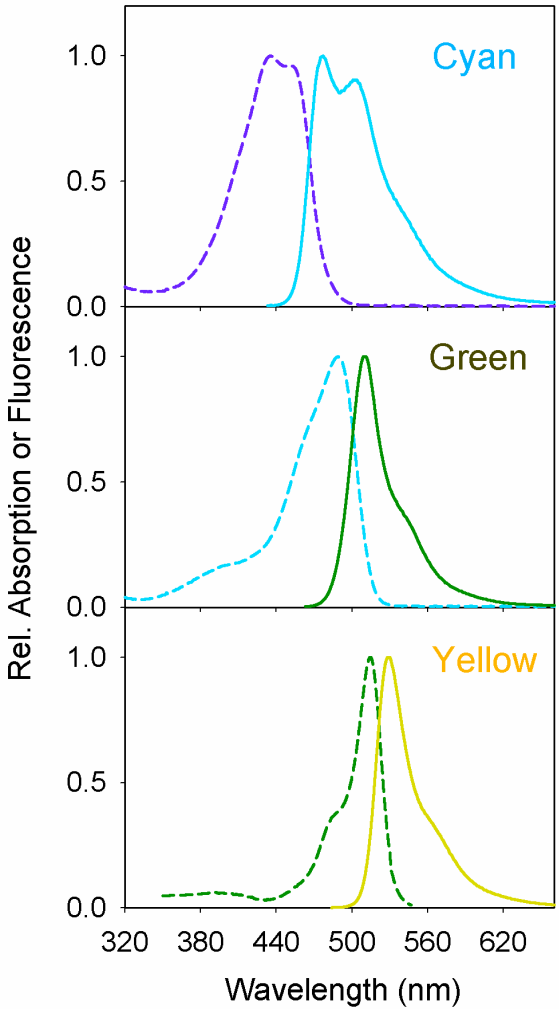

Figure 1.6. Representative spectra of main spectral classes of variants of GFP: Cyan (ECFP), Green (EGFP), and Yellow (EYFP). The absorption spectra (dash lines) and emission spectra (solid lines) were measured under single-photon excitation. Data is taken from the fluorescent protein database (i.e., fpbase.org).

The cyan variants of the green fluorescent protein, CFP, carrying a tryptophan-base chromophore, provide many desirable features, such as increased pH balance and suitability for stable transfection [38]. These features make CFP appealing to use as a fusion tag in many life science applications, as such in vivo FRET measurements. The tryptophan accounts for the blue shift in the absorption spectra to a single peak at 434 nm and indole formation that improves luminosity [39, 40]. CFP variants have a unique emission spectrum that best fits a double

Gaussian. Along with these features, many of these variants of CFP may have several disadvantages, such as a low quantum yield, a low extinction coefficient [38, 41], and low photostability [14, 42]. The absorption and emission spectra of three main spectral variants of GFP, cyan, green, and yellow fluorescent proteins are shown in figure 1.6.

1.2.2. Variant with pH sensitivity

Numerous variants of GFP have been identified as visual indicators of intracellular pH in living cells [36, 43]. It has been found that the fluorescence absorption and emission of variants of GFP is strongly pH-dependent in aqueous solutions and the intracellular compartments of living cells. An investigation of the high-resolution crystal structure of GFP S65T variant at pH 8.0 and 4.6 revealed changes in the hydrogen bond pattern with the chromophore [44]. This suggests that the pH sensitivity derives from the protonation of the chromophore phenolate. That study claims that the chromophore at the ground state of S665T consists of a pH-dependent equilibrium between the neutral and anionic form with the heterocyclic ring nitrogen deprotonated. Hence, the change in pH can change the state of chromophore from neutral (protonated) to ionic (deprotonation) state, which causes major effects on the spectral emission and absorption characteristics. It was observed that the S65T exhibits comparatively low fluorescence upon excitation with UV light in the protonated state, i.e., at low pH value of ~ 4.6. In the same investigation, mutations were designed in yellow fluorescent protein (S65G/V68L/S72A/T203Y) to change the solvent accessibility (H148G) and to modify polar groups (H148Q, D22Q) near the chromophore. The pH titrations of these variants indicate that the pKa value of chromophore can be modulated over a broad range from pH 5 to pH 9.

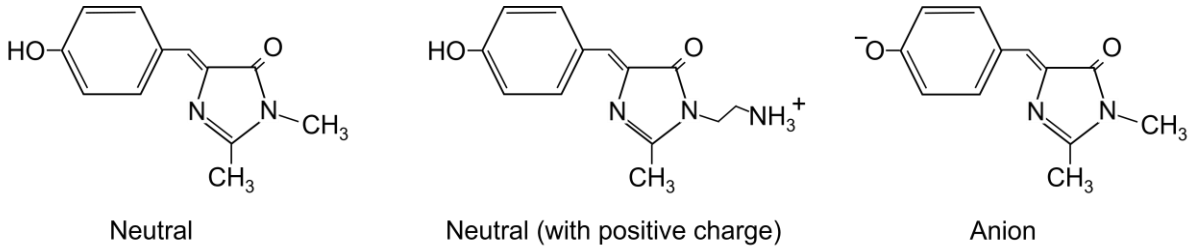

Figure 1.7. Chromophore model of GFP: Protonated "neutral" chromophore model (left), the "neutral" chromophore model with a positively charged side group (middle), and deprotonated "Anion" model chromophore. Figure is adapted from L. Lammich et al [45].

1.2.3. Variants with monomeric or dimeric properties

Several observations, including spectral perturbations induced by changes in concentration [16], yielded translational diffusion coefficients based on fluorescence correlation microscopy measurements [46]. The molecular structure of GFP [24] and structural analysis of dimeric mutants [47] suggest that protein tends to monomerize at low concentrations and dimerizes at high concentrations. It was found that the structure of wtGFP is dimeric [24]. According to Tsien [2], the dimer interface included hydrophobic residues Als206, Leu221, and Phe223 and hydrophilic contacts involving Tyr39, Glu142, Asn144, Ser147, Asn149, Tyr151, Arg168, Asn170, Glu170, Glu172, Tyr200, Ser202, Gln204, and Ser208. However, the same wtGFP could still be crystallized as a monomer with the substitution of S65T mutation [48]. Likewise, a truly monomeric mutation, A206K, has been introduced into most of the widely used variants of GFP that produce a very minimal effect on the spectroscopy properties [47]. In the case of cyan variants of GFP containing Y66W and N146I mutation prevents dimerization at high concentrations.

Monomeric variants of GFP are advantageous in fluorescence imaging, for example, to image homo-oligomerization in living cells. The dimerization tendency of FPs may lead to

artifacts in fluorescence imaging by producing unwanted clustering events. Hence monomeric FPs are more desirable in fluorescence imaging applications.

1.3. Photophysical properties of fluorescent proteins (FPs)

The genetically modified (or mutated) FPs have been broadly used as fluorescent tags in many fluorescence applications based on their photophysical properties. Different FPs have different photophysical properties, such as maximum emission and excitation wavelength, quantum yield (QY), extinction coefficient (ε), brightness, pH sensitivity, photostability, etc. These properties make them unique and appropriate for specific applications. For example, brightness is one of the most desirable features of FPs in most of the fluorescence applications like FRET and FIF. While the substantial overlap between the emission spectrum of one FP (donor) with the excitation spectrum of another FP (acceptor) is highly desirable for FRET measurements. The photostability of a fluorescent protein determined by its ability to undergo photoconversion between different emission or excitation states and its susceptibility to photobleaching. Some FPs possess photophysical properties that can be modified by light irradiation at specific wavelengths. Irreversible photoconversion is a permanent modification where a non-fluorescent state may get permanently photoactivated to a bright state or a bright state may change to another with different emission wavelength (see Fig. 1.8). Reversible photoswitching occurs when a chromophore switches between two molecular conformations [49], while photobleaching is the permanent loss of fluorescence in a fluorescent molecule due to prolonged exposure to high-intensity light.

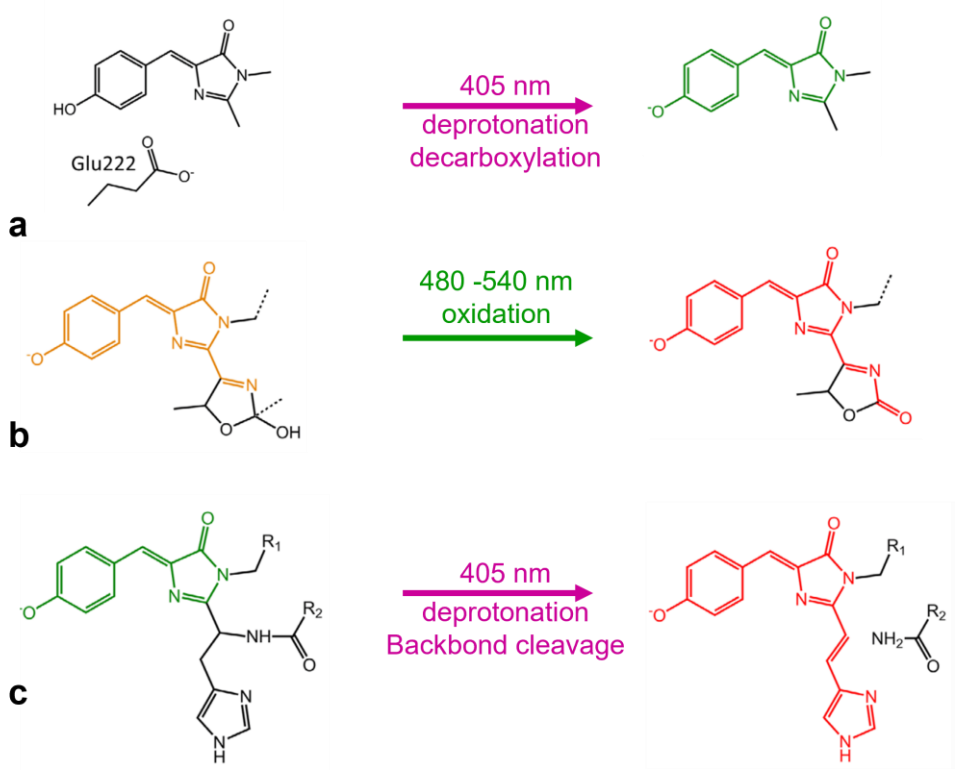

Figure 1.8. Light-induced irreversible photoconversion of various GFP-type chromophore. a. In photoactivatable GFP (PA-GFP), decarboxylation of the Glu22 side chain stabilizes the anionic state of chromophore. **b.** In mOrange, oxidation expands the chromophores π-electron system. **c.** In EosFP, deprotonation and backbone cleavage extend the π-electron system that causes shift in emission wavelength green to red. Figure is adapted from K. Nienhaus et al [49].

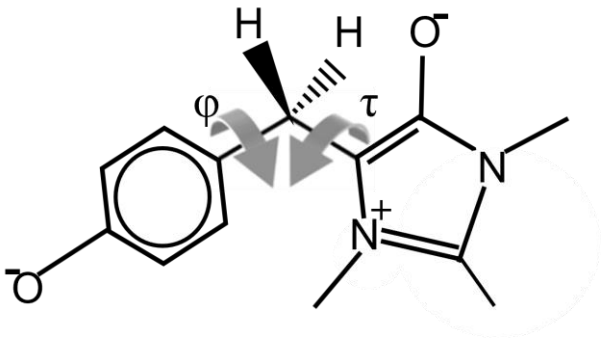

Figure 1.9. Proposed chromophore structure of the doubly reduced/protonated IrisFP chromophore CαN photobleached under high-intensity illumination. Figure is adapted from C. Duan et al [50].

Table 1.1 presents a summary of the photophysical properties of some widely used GFP variants under single-photon excitation, showing the excitation and emission wavelengths, extinction coefficient (ε, capacity for light absorption), quantum yield (QY, the number of photons emitted per excitation photon absorbed), fluorescence lifetime and Förster-radius (R_0) [51] of some commonly used FRET pairs. A comparison of photophysical effects of these widely used FPs under two-photon excitation will be presented later in chapter 3.

Table 1.1. Summary of the photophysical properties of some widely used FPs under single photon excitation. The lifetimes of the FPs are taken from the fluorescent protein database (fpbase.org) and all other information are obtained from the literature (indicated in the column for FPs).

FP	λ_{ex} (nm)	λ_{em} (nm)	$\varepsilon(m^{-1}M^{-1})$	QY	Lifetime (ns)	Donor/Acceptor Förster-radius, R_0 (nm)
wtGFP **[1, 15]**	395	509	25,000	0.79	2.5	-
EGFP **[26, 51]**	488	507	56,000	0.6	2.6	EGFP/YFP (5.6)
GFP2 **[5, 52]**	395	507	21,000	0.55	-	GFP2/YFP (5.5)
YFP **[5, 26]**	514	527	83,400	0.61	3.1	CFP/YFPP (4.7)
Venus **[53, 54]**	515	528	92,200	0.57	3.0	Cerulean/Venus (5.2)
SYFP2 **[55, 56]**	515	529	101,000	0.68	2.9	SCFP3/SYFP2 (5.4)
Citrine **[55]**	516	529	77,000	0.76	3.6	ECFP /Citrine (4.8)
Cerulean3 **[57]**	433	475	40,000	0.84	4.1	Cerulean3/Venus (5.7)
mTurquoise **[58]**	434	474	30,000	0.86	3.7	mTurquoise/Venus (5.7)
mTFP1 **[4, 59]**	464	492	64,000	0.85	3.2	mTFP1/Citrine (5.7)

1.4. Physical underpinnings of fluorescence

1.4.1 Jablonski diagram for fluorescence

The emission of light from any fluorescent molecule in the electronically excited state is categorized into two categories: fluorescence and phosphorescence (see Figure 1.10 for an illustration), based on the time it takes from excitation to emission. The electron in its singlet ground state (S_0) absorbs the photon of appropriate energy and jumps to one of the excited singlet states (S_1 or above, depending on the amount of photon observed). Absorption is a very fast process; it takes on the order of 10^{-15} seconds. Thereafter, the excited electron in the higher excitation state starts dissipating energy to transit to the lowest vibrational level of the first excitation state (S_1) through several different mechanisms. One pathway is by dissipating energy to its surrounding, i.e., vibrational relaxation; however, this can't occur for the isolated molecules. The second pathway can be the coupling between a vibrational level of an electronically higher excitation state and a vibrational level of a lower excitation state, which is called internal conversion (IC). The transit from the higher electronic state to the lower electronic state during internal conversion causes the emission of heat. Both the internal conversion and the vibrational relaxation are non-radiational processes; these processes can take 10^{-14} to 10^{-11} seconds. After the transition to the lowest vibrational level of the excitation state, the system loses energy and transits to the ground state by emitting red-shifted photons. This process of emission of photons is called fluorescence and occurs after 10^{-9} to 10^{-7} seconds. If the energy difference in the transit between two energy states is ΔE, then the planks relation states that ΔE is equal to the product of the frequency of the emitted photon (ν) and the Planck's constant (i.e., $\Delta E = \nu h$, where $h = 6.624 \times 10^{-34}$ Js). During the fluorescence process, the average lifetime of a fluorophore is the time between its excitation and return to the ground state, i.e.,

fluorescence lifetime depends only on the radiative de-excitation rate of the fluorophore from S_1 to S_0.

Another pathway of transition to the lowest vibrational level is intersystem crossing (ISC). In this process, the electron from the excited singlet state transits to a state with a different spin multiplicity, the triplet state (T_1), which is forbidden by the selection rules. ISC is also a non-fluorescence process that takes 10^{-8} to 10^{-3} seconds. This transition of the electron to a state with different spin multiplicity led to the phenomenon of phosphorescence. The phosphorescence is the slowest process in the Jablonski diagram, and it can take 10^{-4} to several seconds to occur.

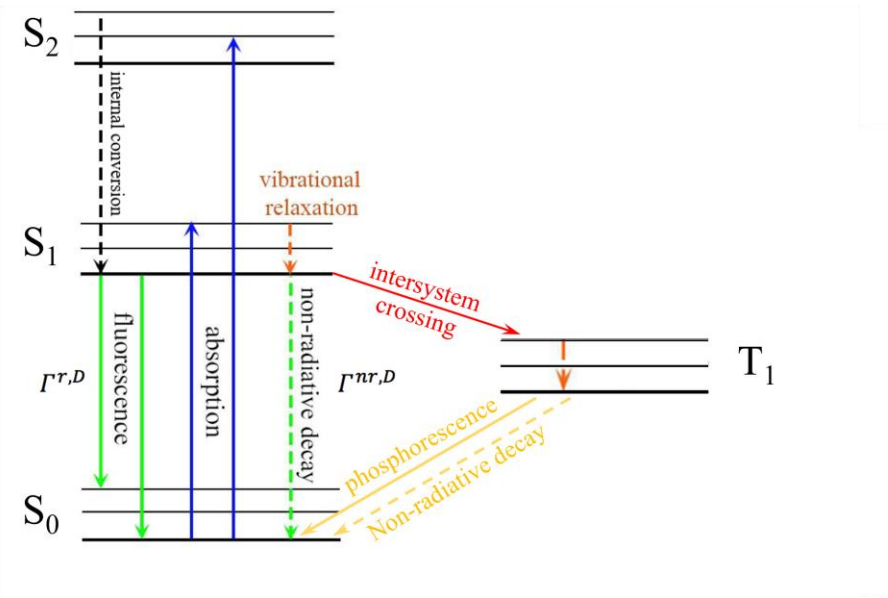

Figure 1.10. Jablonski diagram to describe the electronic transition between energy levels for fluorescence and phosphorescence processes. The horizontal black solid lines represent singlet (S) and triplet (T) energy states with the different vibrational energy levels depicted by thinner solid black lines. The subscripts are given for different excitation states, such as 0 for the ground state, 1 for the first excitation state, etc. Vertical solid blue line, solid green, dashed green line, and dashed black line represent absorption, radiative emission, non-radiative decay, and internal conversion, respectively, whereas solid red line, dash orange line, solid yellow line, and yellow dashed line represent Inter-system Crossing (ISC), vibrational relaxation, phosphorescence and non-radiative de-excitation from triplet state.

1.4.2. Fluorescence lifetimes and quantum yields

Fluorescence lifetimes and quantum yields are perhaps some of the most important characteristics of a fluorophore. The fluorescence lifetime, τ, of the fluorophore determines the time for the fluorophore to be present in the excited state prior to its return to the ground state [60]. The fluorescence lifetime is typically in the order of 10 ns, which needs a highly sophisticated system to measure. Theoretically, it can be expressed in terms of de-excitation (decay) rates of all the de-excitation pathways that occurred in the process. If Γ^{r} and Γ^{nr} are the de-excitation rate for the radiative and non-radiative processes that occurred in the Jablonski diagram, the lifetime of the fluorophore is given by

$$\tau = \frac{1}{\Gamma^{r} + \Gamma^{nr}}. \qquad [1.1]$$

The lifetime of the fluorophore in the absence of non-radiative decay is called the intrinsic or the natural lifetime, which is given by

$$\tau_{n} = \frac{1}{\Gamma^{r}}. \qquad [1.2]$$

The quantum yield (Q) of a fluorophore determines the efficiency of emission of the photon. Theoretically, we can determine quantum yield as the fraction of de-excitation through radiative decay and winch is given by

$$Q = \frac{\Gamma^{r}}{\Gamma^{r} + \Gamma^{nr}}. \qquad [1.3]$$

Combining Eq. 1.1 and Eq. 1.2, we get,

$$\tau_{n} = \frac{\tau}{Q}. \qquad [1.4]$$

Hence, the intrinsic lifetime of the given fluorophore can be express in term of fluorescence lifetime, τ, and the quantum yield, Q, of the fluorophore with Eq. 1.4. The

fluorescence lifetime and quantum yield of the fluorophore in the present FRET will be described in in Chapter 2.

Chapter 2. Förster resonance energy transfer (FRET)

Following the basic introduction to FRET in Chapter 1, this chapter presents a detailed derivation and describes the underlying principle of FRET and the kinetic model of FRET, as it has been applied and verified both experimentally and theoretically later in Chapter 4. The overall chapter has been organized into several sections; the first section is associated with the elementary theory of FRET. The second section describes the classical derivation of energy transfer efficiency by Perrin with necessary components and Förster's modifications on the classical derivative of energy transfer. The third section describes methods of FRET measurement for different oligomeric complexes using various experimental procedures. The fourth section describes the underline concept of the kinetic theory of FRET and its derivation with a brief history coupled with the theory. Finally, in the fifth section, it offers a theoretical guideline to address potential systematic errors in FRET measurements. This guideline connects the theoretical foundations of FPs with their practical application in experimental biology, especially in the study of protein structure and their interactions in living cells.

2.1. Overview of Förster resonance energy transfer (FRET)

Förster Resonance Energy Transfer is named after the German professor Theodor Förster. He developed the theory for non-radiative resonance energy transfer and predicted the distance-dependent rate of energy transfer and the theoretical/experimental value of Förster distance (R_0) [61] using his predecessor's (Kallman and London's) knowledge in dipole-dipole interactions [62] and resonance concepts [63].

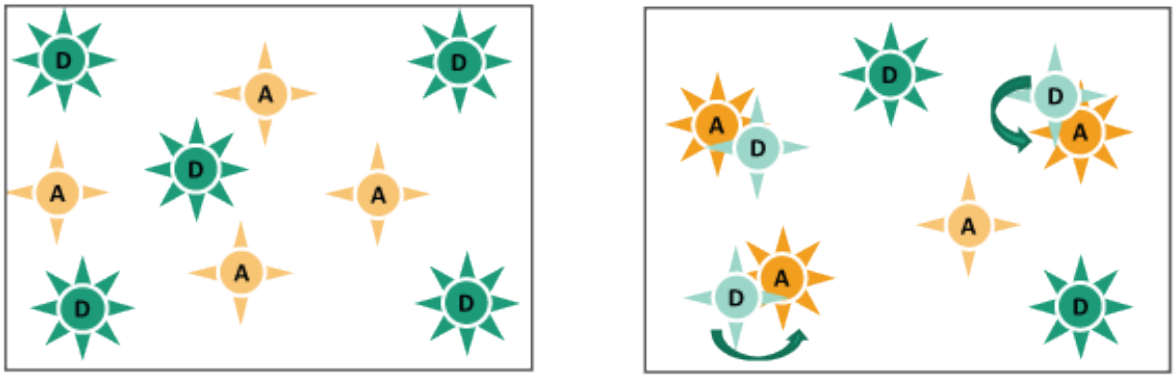

Figure 2.1. Illustration of the non-radiative energy transfer from an excited donor molecule to a nearby acceptor molecule. (a) Donor (D) and acceptor (A) fluorescent molecules are separated by large distances (greater than 10 nm), the excited donors emit as a result. **(b)** As the donor is brought closer to an acceptor (less than 10 nm), FRET may occur, and the acceptor gets excited and emits photons.

In FRET, energy from an excited donor molecule transfer non-radiatively to a nearby acceptor chromophore via dipole-dipole interaction [60, 63-65]. The fraction of the radiation energy observed by a donor molecule transferred to an acceptor molecule during the FRET interaction is called FRET efficiency. The elementary theory of FRET and associated derivation for FRET will be presented thoroughly in the next sections. In brief, the efficiency of energy transfer is inversely proportional to the sixth power of the distance between donor and acceptor chromophore, which makes FRET extremely sensitive to distance and can only be observed when the distance between the excited donor and acceptor is less than 10 nm. The distance between the interacting donor and the acceptor is also much smaller than the wavelength of the emitted light. Figure 2.1. the nonradiative energy transfer that may occur when a donor molecule is close to an acceptor molecule.

In recent years FRET experiments have been designed to study the structure, dynamics, and interaction of biological macromolecules in living cells using fluorescence microscopy [66].

2.1.1. Elementary theory of FRET

Förster resonance energy transfer (FRET) is a non-radiative transfer of energy from an excited donor molecule to a nearby acceptor chromophore via dipole-dipole interaction [60, 63-65]. In 1946, Förster developed the theory for non-radiative resonance energy transfer and predicted the distance-dependent rate of energy transfer. This extremely sensitive process can be observed when the distance between the excited donor and acceptor is less than 10 nm (see Fig. 2.2). A detailed derivation of Förster's equation for FRET will be presented later in section 2.2.

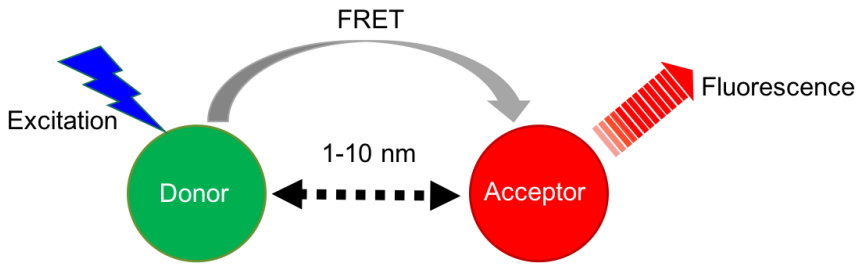

Figure 2.2. Non-radiative energy transfer from an excited donor molecule to a nearby acceptor molecule. As donor (D) and acceptor (A) fluorescent molecules are brought closer to each other (less than 10 nm), FRET may occur, and the acceptor gets excited and emits photons.

2.1.2. Jablonski diagram for FRET and Quantum Yields

A schematic representation of the process of energy transfer from an excited donor molecule to a nearby unexcited acceptor molecule through FRET, also known as the Jablonski diagram for FRET, is shown in Fig. 2.3. S_{D0}, S_{D1}, and S_{D2} are the ground, first, and second electronic states of the donor, and S_{A1} and S_{A2} are the ground state and the first excited state of the acceptor, respectively. In the presence of an acceptor (i.e., fluorophore with lower excitation energy than the emission energy of the donor) in proximity (<10 nm) to the excited donor, energy can

transfer from the excited donor to the acceptor through dipole-dipole coupling. In this process, the donor molecule loses its excitation energy through a non-radiative coupling between the transition dipole of the excited donor to that of an unexcited acceptor. Hence, the acceptor molecule gets excited non-radiatively from the ground to the first excited state and then de-excites to the lowest vibrational energy state of the first excitation level via vibrational relaxation from where it de-excites to the ground state either non-radiatively or with the fluorescence emission.

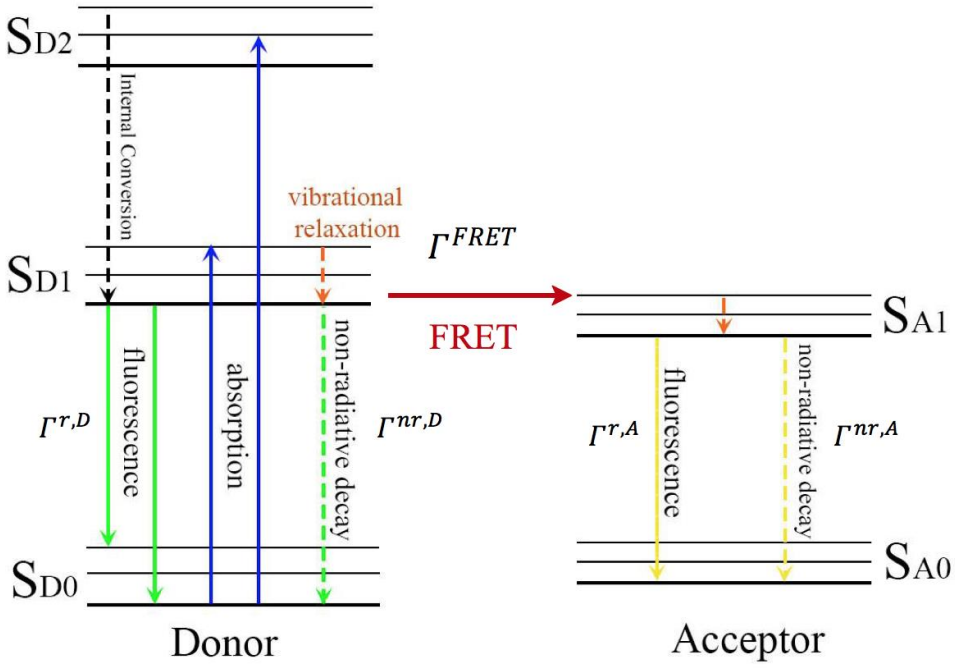

Figure 2.3. Jablonski diagram describing fluorescence resonance energy transfer (FRET) between an excited donor (D) and a nearby acceptor (A) molecules. The horizontal black solid lines represent singlet (S) states with the different vibrational energy levels depicted by thinner solid black lines. The subscripts D is given for donors and A is given for acceptors with the different excitation states: such as 0 for the ground state, 1 for the first excitation state, etc. The solid red arrow pointing from D to A represents the FRET. The terms $\boldsymbol{\Gamma^{r,D}}$ and $\boldsymbol{\Gamma^{nr,D}}$ are the rate constants of radiative, non-radiative decay, whereas $\boldsymbol{\Gamma^{FRET}}$ is the rate constant for resonance energy transfer (RET) between the single pairs of donor and acceptor.

The quantum yield (Q) of a fluorophore is the fraction of de-excitation (energy decay) through radiative decay that determines the efficiency of the emission of the photon. If Γ^r and Γ^{nr} the rate constants of radiative, non-radiative decay, then the quantum yields of a donor, Q^D, and an acceptor, Q^A, can be written as:

$$Q^D = \frac{\Gamma^{r,D}}{\Gamma^{r,D} + \Gamma^{nr,D}}, \tag{2.1}$$

$$Q^A = \frac{\Gamma^{r,A}}{\Gamma^{r,A} + \Gamma^{nr,A}}, \tag{2.2}$$

where the sum of Γ^r and Γ^{nr} is equal to the inverse of the lifetime of the excited states of a given fluorescence molecule, i.e., the excited state lifetime of donor (τ_D) and acceptor (τ_A) can be expressed as:

$$\tau_D = \frac{1}{\Gamma^{r,D} + \Gamma^{nr,D}} \tag{2.3}$$

and

$$\tau_A = \frac{1}{\Gamma^{r,A} + \Gamma^{nr,A}}. \tag{2.4}$$

In the presence of FRET, it causes an additional pathway for de-excitation of the donor (see Fig. 2.3). Thus, in the presence of FRET (i.e., acceptor) the quantum yield of the donor (Q^{DA}) and lifetime of the donor (τ_{DA}) can be expressed as:

$$Q^{DA} = \frac{\Gamma^{r,D}}{\Gamma^{r,D} + \Gamma^{nr,D} + \Gamma^{FRET}}, \tag{2.5}$$

$$\tau_{DA} = \frac{1}{\Gamma^{r,D} + \Gamma^{nr,D} + \Gamma^{FRET}}, \tag{2.6}$$

where Γ^{FRET} is the rate constant of the energy transfer. This shows that in the presence of FRET both the quantum yield and lifetime of donor decrease from that in the absence of FRET.

2.2.2. Distance dependence transfer of energy

The rate of energy transfer from an excited donor (D) to a nearby unexcited acceptor (A) is given by:

$$\Gamma^{\mathrm{FRET}} = \frac{1}{\tau_D}\left(\frac{R_0}{r}\right)^6, \tag{2.7}$$

where $\tau_D = (\Gamma^{r,D} + \Gamma^{nr,D})^{-1}$ is the lifetime of the donor in the absence of acceptor; r is the distance between the donor and the acceptor and R_0 is the Förster distance. Förster distance is the distance between excited donor and nearby acceptor when the rate of energy transfer between the donor and acceptor is equal to the decay rate of the excited donor in the absence of the acceptor, i.e., the distance at which the efficiency of energy transfer becomes half [64, 67-70]. Derivation of Eq. 2.7 will be presented in section 2.2.

The efficiency of energy transfer can be defined as the fraction of donor de-excitation through FRET. In terms of decay rate constant, the efficiency of energy transfer can be expressed as:

$$E = \frac{\Gamma^{FRET}}{\Gamma^{r,D} + \Gamma^{nr,D} + \Gamma^{FRET}}. \tag{2.8}$$

Substituting Eq. 2.3 and Eq. 2.6 in Eq. 2.8, we obtain:

$$E = 1 - \frac{\tau_{DA}}{\tau_D}. \tag{2.9}$$

Similarly, by substituting Eq. 2.3 and Eq. 2.7 in Eq. 2.8, we obtain:

$$E = \frac{\frac{1}{\tau_D}\left(\frac{R_0}{r}\right)^6}{\frac{1}{\tau_D} + \frac{1}{\tau_D}\left(\frac{R_0}{r}\right)^6} = \frac{R_0^6}{R_0^6 + r^6}. \tag{2.10}$$

Hence, Eq. 2.10 shows that the FRET efficiency decreases rapidly as the separation between donor and acceptor, r, increases (see Fig 2.4). Using Eq. 2.9, we can determine the FRET efficiency by measuring the lifetime of donor in the presence and absence of the acceptor, which in turn allows us to estimate the donor and acceptor distance using Eq. 2.10.

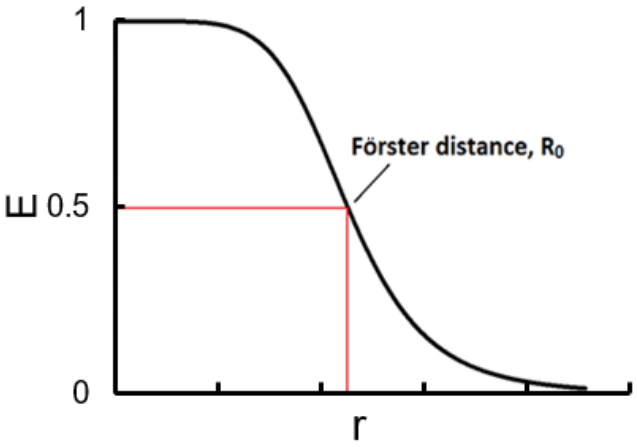

Figure 2.4 Graphical representation of FRET efficiency (E) versus distance (r) between excited donor and acceptor. R_0 is the Förster distance. Figure is inspired from reference [71].

Förster distances are typically in the range of 1.5 to 6 nm, which is comparable to the size of many proteins and thickness of membranes. Thus, FRET is an ideal tool to see protein interaction and their distances both in solution and inside the living cells. When the distance between donor and acceptor (r) is equal to Förster distance (R_0), the FRET efficiency becomes half, where τ_{DA} is half of τ_D.

2.3. Classical derivation of Förster resonance energy transfer rate constant

2.3.1. Perrins' theory of energy transfer

In 1927, the Nobel laureate J. Perrin provided the first theoretical explanation that energy could be transferred from an excited molecule, called a donor (D), to a nearby unexcited molecule, called an acceptor (A) via dipole-dipole interactions [72]. His theoretical explanation began

with considering two electrically charged oscillators interacting through electrostatic force; when the two oscillators share the resonant frequency, they exchange energy. In his classical interpretation of energy transfer, he considers two identical oscillating dipoles Donor (D) and Acceptor (A), with corresponding dipole moments $\vec{\mu}_D$ and $\vec{\mu}_A$ separated by a distance $\vec{R}$ as in Fig. 2.5.

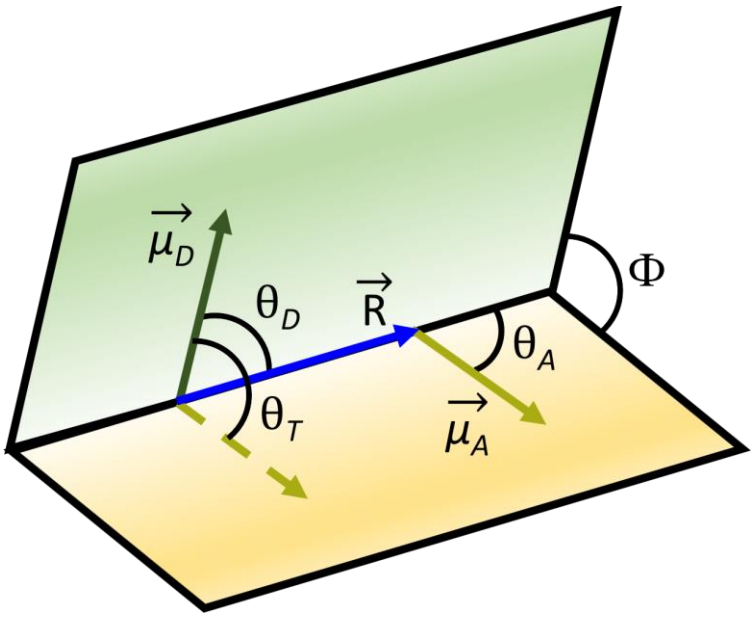

Figure 2.5. Schematic representation of the orientation of donor dipole moment ($\vec{\mu}_D$) and acceptor dipole moment ($\vec{\mu}_A$). Φ represents the angle of intersection between the donor orientation plane (green surface) and the acceptor plane (yellow surface). The solid green and yellow arrows represent the dipole moment of the donor ($\vec{\mu}_D$) and acceptor ($\vec{\mu}_A$), whereas θ_D and θ_A represent the angle made by the separation vector, $\vec{R}$, with the dipole moment of the donor (μ_D) and acceptor (μ_A), respectively, and θ_T represents the angle between $\vec{\mu}_D$ and $\vec{\mu}_A$. Figure is inspired from reference [73].

The electric field (E_D) due to the dipole moment of the donor ($\vec{\mu}_D$) in the above configuration can be expressed as:

$$\vec{E}_D = \frac{1}{n^2 R^3}\left(3\left(\vec{\mu}_D.\hat{R}\right)\hat{R} - \vec{\mu}_D\right), \tag{2.11}$$

where $\hat{R}$ is the unit vector along the separation vector $\vec{R}$ and n is the refractive index of the medium. Now, in the presence of acceptor, dipole moment $\vec{\mu}_A$ in the electric field $\vec{E}_D$, the interaction energy E_{int} can be expressed as,

$$E_{int} = -\vec{\mu}_A.\vec{E}_D = \frac{1}{n^2R^3}\left[(\vec{\mu}_D.\vec{\mu}_A) - 3\left(\vec{\mu}_D.\hat{R}\right)\left(\vec{\mu}_A.\hat{R}\right)\right]. \quad (2.12)$$

Consider the dipoles are identical, i.e., $|\vec{\mu}_D| = |\vec{\mu}_A| = \mu$, with this Eq. 2.12 becomes

$$E_{int} = \frac{\kappa\mu^2}{n^2R^3}, \quad (2.13)$$

where $\kappa = \left[(\hat{\mu}_D.\hat{\mu}_A) - 3\left(\hat{\mu}_D.\hat{R}\right)(\hat{\mu}_A.\hat{R})\right]$ is the orientation factor of donor and acceptor dipole moments. Now, using Planck's quantum theory, i.e., $E = h\nu$, we can write

$$E_{int} = \frac{\kappa\mu^2}{n^2R^3} = h\nu_{int} = \hbar\omega_{\text{int}} \sim \frac{\hbar}{\tau_{\text{int}}},$$

where h is Planck's constant and $\hbar = h/2\pi$, ω_{int} is the angular frequency associated with the interaction energy E_{int}, and τ_{int} is the period of the dipole oscillation. Rearranging above equation we get:

$$\tau_{int} = \frac{\hbar n^2R^3}{\kappa\mu^2}. \quad (2.14)$$

According to the theory of Hertzian oscillation dipole, the energy of radiation and radiation time constant can be expressed as [67, 74]:

$$E_{rad} = \frac{\mu^2\omega^3}{3\,c^3}, \quad (2.15)$$

$$\tau_{rad} = \frac{3\hbar\,c^3}{\mu^2\omega^3}, \quad (2.16)$$

where c is the speed of light and ω is the frequency of the dipole oscillation. Now, the expression for the distance between the oscillating dipoles, R_0, at which radiational decay of

the energy is equal to non-radiative transfer of energy, can be obtained by equating Eq. 2.16 and 2.14 (i.e., $\tau_{rad} = \tau_{int}$,), we get:

$$\frac{3\hbar\, c^3}{\mu^2\omega^3} = \frac{\hbar n^2 R_0^3}{\kappa\mu^2}.$$

Rearranging above equation, we obtain:

$$R_0^3 = \frac{3\kappa c^3}{n^2\omega^3} = \frac{3\kappa}{n^2(2\pi)^3}\lambda^3 \approx 0.01\lambda^3\,, \tag{2.17}$$

where $c = \omega\lambda/2\pi$ and roughly $R_0 \approx 0.2\,\lambda$, which means that half of the donor's energy that would have been emitted radiatively is transferred non-radiatively to the acceptor at a distance roughly one-fifth of the wavelength radiating from the oscillating dipole.

2.2.2. Förster correction to Perrin's theory

Förster found that the calculated value of R_0 by Perrin's model of energy transfer was overly estimated because of the assumption of perfect resonance between the emission and absorption spectrum of donor and acceptor. He noted that the spectra of the donor and acceptor are vastly different, and he correctly took into account the broadened spectra and overlapped frequencies of the excited donor and acceptor in the energy transfer calculation. The spectral overlap between the emission spectrum of donor and absorption spectrum of acceptor occurs only in a range of wavelengths, as shown in Fig. 2.6a. This suggests that the probability of occurrence of resonance between a donor and acceptor is less than that when there is complete spectral overlap.

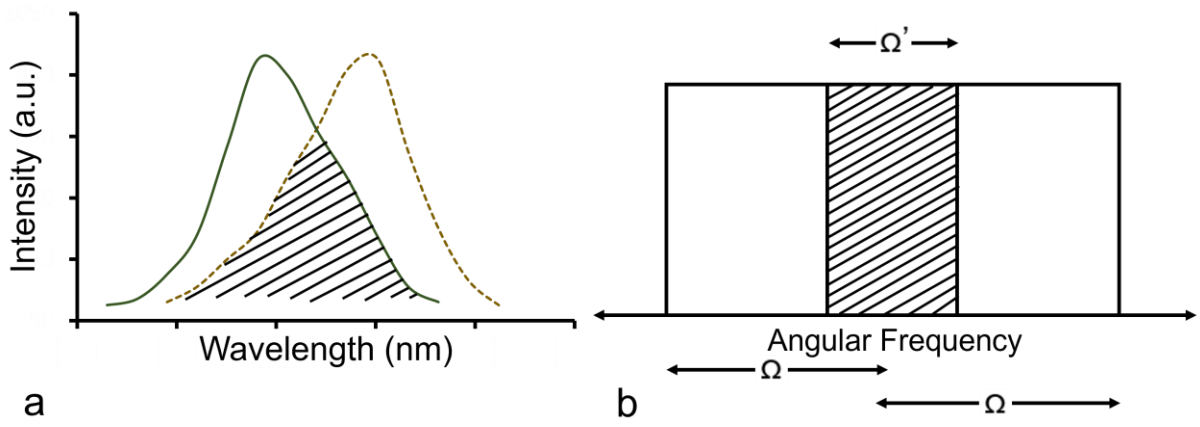

Figure 2.6. Spectra overlap between donor emission spectrum and acceptor absorption spectrum. **a**. Spectral overlap represented with intensity vs. wavelength plot. The solid green line represents the donor emission spectrum, and the dash yellow line represents the acceptor absorption spectrum. b. Spectral overlap between donor emission and acceptor absorption in rectangular form. The shadow region represents the spectral overlap between donor emission and acceptor absorption spectra. The width of each spectrum is Ω and the width of the overlapped rectangular area is Ω'.

Förster assumed that the spectra width of donor and accepter is similar and equal to Ω and the spectral overlap between donor emission and acceptor absorption spectra is Ω' as. in Fig 2.6b. Then the probability spectral overlap of donor and acceptor can be written as Ω'/ Ω. Similarly, the probability of falling the bandwidth Ω within a narrow coupling bandwidth of $E_{int}/\hbar$ is $(E_{int}/\hbar)/\Omega$. Now the probability of simultaneous occurrence of the above two events is given by $\frac{\Omega'}{\Omega}\frac{E_{int}}{\hbar\Omega}$.

Using this probability of simultaneous occurrence of spectral overlap and the spectral bandwidth within coupling bandwidth of $E_{int}/\hbar$, the interaction energy is corrected to the following expression [75].

$$E'_{int} = \left(\frac{\Omega'}{\Omega}\frac{E_{int}}{\hbar\Omega}\right)E_{int.} \tag{2.18}$$

Now, pugging $E_{int} = \frac{\kappa\mu^2}{n^2R^3}$ from Perrin's calculation, i.e., from Eq. 2.13 in above Eq. 2.18, we get:

$$E'_{int} = \left(\frac{\kappa^2\mu^4}{\hbar n^4 R^6}\frac{\Omega'}{\Omega^2}\right). \tag{2.19}$$

This equation shows that the interaction energy (energy transfer) is $\frac{1}{R^6}$ dependent. Now, using $E'_{int} \sim \frac{\hbar}{\tau'_{\text{int}}}$, we can express:

$$\tau'_{int} = \frac{\hbar^2 n^4 R^6}{\kappa^2\mu^4}\frac{\Omega^2}{\Omega'}. \tag{2.20}$$

Now, to obtain the expression for the corrected distance, also called Förster, between the oscillating dipoles, R_0, at which radiational decay of the energy is equal to the non-radiative transfer of energy, i.e., $\tau_{rad} = \tau'_{int}$, equating equations 2.16 and 2.20, we get:

$$\frac{3\,c^3}{\mu^2\omega^3} = \frac{\hbar^2 n^4 R_0^6}{\kappa^2\mu^4}\frac{\Omega^2}{\Omega'}.$$

Rearranging above equation, we get:

$$R_0^6 = \frac{3\kappa^2\mu^2 c^3}{\hbar n^4\omega^3}\frac{\Omega'}{\Omega^2}. \tag{2.21}$$

Using $\tau_{rad} = \frac{3\hbar\,c^3}{\mu^2\omega^3}$ and $c = \omega\lambda/2\pi$ in above equation, we get:

$$R_0^6 = 9\left(\frac{\lambda}{2\pi}\right)^6\left(\frac{\kappa^2}{n^4}\right)\frac{\Omega'}{\Omega^2}\left(\frac{1}{\tau_{rad}}\right). \tag{2.22}$$

For an experimental situation with $\lambda = 600\ nm$ and the spectra overlap ratio, $\Omega'/\Omega \sim 1/10$, the Förster distance, $R_0 \sim 10\ nm$.

2.2.3. Förster's quantum mechanical theory of FRET

After the earlier works by J. Perrin and F. Perrin, Förster corrected the expression of the energy transfer by addressing the broadened spectra and overlapping frequencies of excited donors and unexcited acceptor molecules. The effect of broadened energy distributions had to be considered when calculating a rate of a kinetic process between two quantum states [76]. Utilizing quantum theory, Förster derived quantitatively the correct expression of the probability of energy transfer between the donor and acceptor molecules following the Fermi Golden Rule, which quantitatively relates the rate of transition between quantized stated of a perturbed system by an oscillating electromagnetic field.

Let us consider two separate molecules, a donor (D) and acceptor (A). Initially, if the donor molecule is in an excited state and the acceptor molecule is in the ground state, the antisymmetrized electronic wavefunctions for the initial state wavefunction, $\phi_{i,}$ in which only the donor is excited, and the final state ϕ_f in which only the acceptor is excited can be expressed as follows [77]:

$$\phi_i = \frac{1}{\sqrt{2}} \left(\phi_{D^*}(1)\phi_A(2) - \phi_{D^*}(2)\phi_A(1)\right), \tag{2.23}$$

$$\phi_f = \frac{1}{\sqrt{2}} \left(\phi_D\,(1)\phi_{A^*}(2) - \phi_D(2)\phi_{A^*}(1)\right), \tag{2.24}$$

where 1 and 2 stand for the electrons and the asterisk refer to the excited state. The D and A in subscripts stand for donor and acceptor, respectively.

The Hamiltonian of the system is given by

$$\mathcal{H} = \mathcal{H}_D + \mathcal{H}_A + V_{int}, \tag{2.25}$$

where $\mathcal{H}_D$ and $\mathcal{H}_A$ are the unperturbed Hamiltonians of the donor and the acceptor molecules, respectively, whereas V_{int} is the interaction energy between the two molecules. The interaction matrix element describing the coupling between the initial and final state can be expressed as:

$$U = \langle \phi_f (|V_{int}| \phi_i \rangle. \tag{2.26}$$

With Eq. 2.23 and 2.24, Eq. 2.26 becomes,

$$\begin{aligned} U &= \langle \phi_D\,(1)\phi_{A^*}(2)|V_{int}|\phi_{D^*}(1)\phi_A(2)\rangle - \langle \phi_D(2)\phi_{A^*}(1)|V_{int}|\phi_{D^*}(1)\phi_A(2)\rangle \\ &= U_c - U_{ex} \end{aligned} \tag{2.27}$$

where U_c is the Coulombic field term that describes the initially excited electron of the donor returns to the ground state while the electron of the acceptor gets excited, whereas U_{ex} is the exchange term that describes when two electrons of D and A are physically exchanged. This exchange of electrons is a quantum effect due to the symmetric properties of the electronic wavefunctions, which causes the interaction between the electron clouds. This only happens when the donor and acceptor are in contact or when their electron clouds overlap. Because the electron density decays exponentially outside a molecule, the exchange of electrons is considered only at short distances, which is not the case with FRET. Therefore, only the Coulombic field term is considered for the energy transfer.

Now, the initial and excited state can be generalized in terms of original state energies and the transfer energy E. Under the Born-Oppenheimer approximation, we can express the initial and final wave functions of the system in terms of electronic and vibrational components, as follows:

$$\Psi_i = \Psi_{D^*A}(E_D^*, E_A) = \phi_D^* \phi_A \chi_D^*(E_D^*)\chi_A(E_A), \tag{2.28}$$

$$\Psi_f = \Psi_{DA^*}(E_D, E_A^*) = \phi_D \phi_A^* \chi_D(E_D^* - E)\chi_A^*(E_A + E), \quad (2.29)$$

where E_D and E_A are the energies of donor and acceptor, respectively, whereas ϕ^* and ϕ are the excited and unexcited electronic wave function and χ^* and χ are the excited and unexcited vibrational wave function of the molecules. Subscript D and A stand for donor and acceptor.

The energy difference between the final ($i.e., E_f = E^*{}_A + E_D$) and initial (i.e., $E_i = E_D^* + E_A$) can be expressed as:

$$\Delta E = E^*{}_A + E_D - E_D^* - E_A. \quad (2.30)$$

Since the energy lost by the donor due to de-excitation is equal to the energy gained by the acceptor to its excited state, we can express:

$$E = \frac{1}{2}[E_D^* - E_D + E_A^* - E_A]. \quad (2.31)$$

Now, using the initial and final wavefunction of the system (i.e., with Eq. 2.28 and 2.29), the Coulombic field term can be expressed as:

$$U_c = \langle \phi_D \, \phi_A^* | V_{int} | \phi_D^* \, \phi_A \rangle \langle \chi_D(E_D^* - E) | \chi_D^*(E_D^*) \rangle \langle \chi_A^*(E_A + E) | \chi_A(E_A) \rangle,$$

$$U_c = W S_D(E_D^*, E_D^* - E) S_A(E_A, E_A + E), \quad (2.32)$$

where W=$\langle \phi_D \, \phi_A^* | V_{int} | \phi_D^* \, \phi_A \rangle$ is the electronic interaction matrix, and

$S_D(E_D^*, E_D^* - E) = \langle \chi_D(E_D^* - E) | \chi_D^*(E_D^*) \rangle$ and $S_A(E_A, E_A + E) = \langle \chi_A^*(E_A + E) | \chi_A(E_A) \rangle$ are the vibrational overlap integral, which is also known as Franck-Condon factor.

The electronic interaction matrix can be expended using multipole-multipole interactions, but it is generally approximated using dipole-dipole interactions between the transition dipole moments, which can be expressed as:

$$\vec{\mu} = -e\sum_{k}\langle\phi_f|\overrightarrow{r_k}|\phi_i\rangle, \tag{2.33}$$

where $\overrightarrow{r_k}$ is the position vectors of the electrons. Now, in the presence of the transition dipole moments of donor and acceptor (i.e., $\vec{\mu}_D$ and $\vec{\mu}_A$, respectively) the electronic interaction matrix, W_{dd} can be expressed as (using Eq. 2.11)

$$W_{dd} = \frac{1}{n^2}\left[\frac{\vec{\mu}_D.\vec{\mu}_A}{r^3} - 3\frac{(\vec{\mu}_D.\vec{r})(\vec{\mu}_A.\vec{r})}{r^5}\right]$$

$$= \frac{\kappa\vec{\mu}_D\vec{\mu}_A}{n^2r^3}, \tag{2.34}$$

where n is the refractive index of the medium and $\kappa = [(\hat{\mu}_D.\hat{\mu}_A) - 3(\hat{\mu}_D.\hat{r})(\hat{\mu}_A.\hat{r})]$ is the orientation factor of donor and acceptor dipole moments. If θ_D and θ_A, are the angle between the dipole moment the vector position vector $\vec{r}$ and the transition dipole moments of the donor and acceptor, respectively, and θ_{DA} is the angle between the dipole moments, the orientation factor of donor and acceptor can be written as:

$$\kappa = cos\theta_{DA} - 3cos\theta_D cos\theta_A. \tag{2.35}$$

Note, the dipole-dipole approximation is valid only when the donor-acceptor distance is much larger than the molecule's dimensions.

Now, according to time-dependent perturbation theory, the transition probability between $\Psi_{D^*A}(E_D^*, E_A)$ to $\Psi_{DA^*}(E_D, E_A^*)$ for a large interaction time, that is, for a very coupling can be expressed as [78].

$$P(D^*A \to DA^*) \cong \frac{\pi t}{\hbar^2}\iint U_C^2(E_D, E_A^*)\lim_{t\to\infty}\frac{\sin^2\left[\frac{\Delta Et}{2\hbar}\right]}{\pi\left(\frac{\Delta Et}{2\hbar}\right)^2 t}dE_D dE_A^*. \tag{2.36}$$

Let's define Dirac delta function,

$$\delta(x) = \lim_{t\to\infty} \frac{\sin^2[tx]}{\pi t x}. \tag{2.37}$$

After, applying Dirac delta function (i.e., Eq. 2.37) in the expression of transition probability (i.e., in Eq. 2.36) and solving we can obtain [78]:

$$P(D^*A \to DA^*) \cong \frac{2\pi t}{\hbar^2} \int U_C^2(E,0)\mathrm{dE}. \tag{2.38}$$

By substituting U_C from Eq. 2.32a and W_{dd} from Eq. 2.34, in Eq. 2.38, we obtain:

$$P(D^*A \to DA^*) = \frac{2\pi t}{\hbar^2} \frac{\kappa^2 \mu_D^2 \mu_A^2}{n^4 r^6} \int S_D^2(E_D^*, E_D^* - E) S_A^2(E_A, E_A + E)\mathrm{dE}. \tag{2.39}$$

According to Fermi's Golden Rule, the rate of transition per unit time is equal to the rate of energy transfer, which can be expressed as:

$$\begin{aligned} \Gamma^{\mathrm{FRET}} &= \frac{2\pi t}{\hbar^2} \frac{\kappa^2 \mu_D^2 \mu_A^2}{n^4 r^6} \int S_D^2(E_D^*, E_D^* - E) S_A^2(E_A, E_A + E)\mathrm{dE}, \\ &= \frac{\kappa^2 \mu_D^2 \mu_A^2}{n^4 r^6 \hbar^2} \int S_D^2(E_D^*, E_D^* - E) S_A^2(E_A, E_A + E)\mathrm{d\nu}, \end{aligned} \tag{2.40}$$

where $\nu = E/2\pi\hbar$ is the transition frequency. This expression is for the energy transfer from an excited donors with energy E_D^* to unexcited acceptors in the ground state with energy E_A. If the molecules are in thermal equilibrium, the energy transfer rate can be obtained by introducing the Boltzmann factor, $\int g(E)dE$= 1.

where $g(E) = \frac{1}{k_B T} \exp\left(-\frac{E}{\mathrm{k_B} T}\right)$, and k_B is the Boltzmann constant. With this Eq. 2.40 becomes,

$$\begin{aligned} \Gamma^{\mathrm{FRET}} = \frac{\kappa^2}{n^4 r^6 \hbar^2} \int \mu_D^2 \left[\int g(E_D^*) S_D^2(E_D^*, E_D^* - E) dE_D^*\right] \\ . \left[\mu_A^2 \int g(E_A) S_A^2(E_A, E_A + E) dE_A\right] \mathrm{d\nu}. \end{aligned} \tag{2.41}$$

The interactions between transition dipole moments of molecules and quantized energies in spontaneous de-excitation and stimulated excitation can be defined with Einstein's

A and B coefficients [79]. The normalized fluorescence emission spectrum of donors, $f_D(v)$, and absorption spectrum of acceptor $\mathcal{E}_A(v)$, can be written as:

$$f_D(v) = \frac{2^5 n\tau_n \pi^3 v^3 \mu_D^2}{3c^3 \hbar} \int g(E_D^*) S_D^2(E_D^*, E_D^* - E) dE_D^*, \tag{2.42}$$

$$\mathcal{E}_A(v) = \frac{2^2 \pi^2 v\, \mu_A^2 N_A}{3000 In(10) nc\, \hbar} \int g(E_A) S_A^2(E_A, E_A + E) dE_A, \tag{2.43}$$

where τ_n is lifetime of the donor and N_A is the Avogadro's number.

After substituting $f_D(v)$ from Eq. 2.41 and $\mathcal{E}_A(v)$ from Eq. 2.42 into Eq. 2.41, we get:

$$\Gamma^{\text{FRET}} = \frac{9000\kappa^2 In(10) c^4}{128\pi^5 n^4 N_A \tau_n r^6} \int \frac{f_D(v)\mathcal{E}_A(v)}{v^4} dv. \tag{2.44}$$

Let us introduce the spectral overlap integral is defined as follow,

$$J = \frac{f_D(v)\mathcal{E}_A(v)}{v^4}. \tag{2.45}$$

By combining Eq. 2.45 and Eq. 2.44, we can get the expression for the rate of energy transfer as follows,

$$\Gamma^{\text{FRET}} = \frac{9000\kappa^2 In(10) c^4 J}{128\pi^5 n^4 N_A \tau_n r^6}, \tag{2.46}$$

where τ_n is the fluorescence lifetime of donor, in order to express the fluorescence lifetime of donor in term of experimentally measurable quantities, the following relation can be used.

$$\tau_n = \frac{Q^D}{\tau_D}, \tag{2.47}$$

where Q^D is the quantum yield of the donor molecule, whereas τ_D is the lifetime of the donor in terms of de-excitation rated as defined in Eq. 2.4. With Eq. 2.47 and Eq. 2.46, the rate of energy transfer becomes,

$$\Gamma^{\mathrm{FRET}} = \frac{9000\kappa^2 Q^D In(10) c^4 J}{128\pi^5 n^4 N_A \tau_D r^6}. \tag{2.48}$$

By introducing the Förster distance (R_0) as follow,

$$R_0^6 = \frac{9000\kappa^2 Q^D In(10) c^4 J}{128\pi^5 n^4 N_A}. \tag{2.49}$$

Then Förster came up with the following expression for the rate constant of energy transfer between the donor and acceptor because of dipole-dipole interaction.

$$\Gamma^{\mathrm{FRET}} = \frac{1}{\tau_D}\left(\frac{R_0}{r}\right)^6. \tag{2.50}$$

This expression is also known as the Förster energy transfer rate.

2.3. Methods of FRET efficiency measurement

In this section, we present the expressions of different fundamental quantities of FRET measurements in terms of experimentally observable quantities, which have been derived previously by Dr. Valerică Raicu [80].

2.3.1. Kinetic model of fluorescence and FRET

The relationships between the different rates of excitations, de-excitations, and the probabilities of fluorescence molecules being in their excited state can be derived using a simple kinetic model presented in Fig. 2.7. Based on the model, for donors in the absence of acceptors (see Fig. 1a), the rate of change of probability of donor in an excited state (p_{D^*}) can be expressed as,

$$\gamma^{ex,D} p_D - (\gamma^{r,D} + \gamma^{nr,D}) p_{D^*} = \frac{dp_{D^*}}{dt}, \tag{2.51}$$

where p_D and p_{D^*} are the probabilities of finding donors in its ground state and excited state, respectively, $\gamma^{ex,D}$ is the rate of excitation of donors initially in the ground state (D), $\gamma^{r,D}$ and $\gamma^{nr,D}$ are de-excitation of donors in the excitation state through radiative (emission of photons) and non-radiative (internal conversion) process, respectively.

Similarly, for acceptors in the absence of donors (see, Fig. 2.7.b), the rate of change of probability of j[th] acceptor to be in an excited state (p_{A^*}) can be expressed as,

$$\gamma^{ex,A} p_A - (\gamma^{r,A} + \gamma^{nr,A}) p_{A^*} = \frac{dp_{A^*}}{dt}, \tag{2.52}$$

where p_A and p_{A^*} are the probabilities of finding acceptors in its ground state and excited state, respectively. $\gamma^{ex,A}$ is the rate of excitation of acceptors initially in the ground state (A), $\gamma^{r,A}$ and $\gamma^{nr,A}$ are de-excitation rate of acceptor in the excitation state through radiative (emission of photons) and non-radiative (internal conversion) process, respectively.

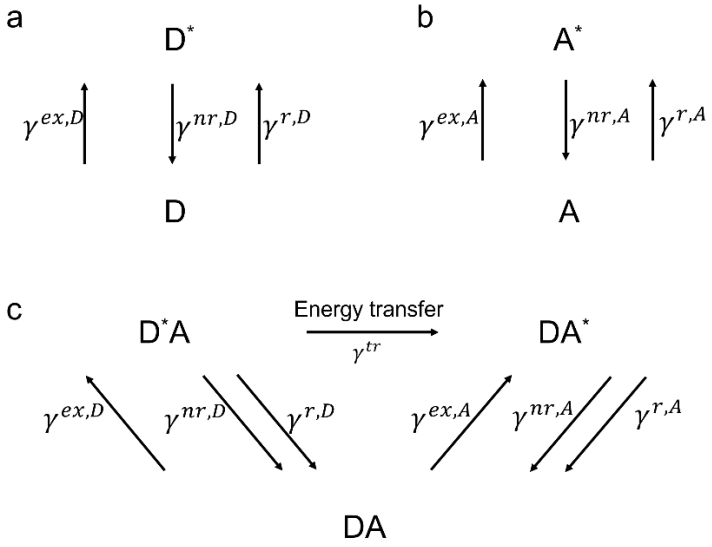

Figure 2.7. Schematic representation of the kinetic model of fluorescence and FRET. a) Donors (D), in the absence of acceptor (A). **b)** Acceptors in the absence of donor, and **c)** Donors and acceptors together (i.e., FRET). Figure is adapted with permission from reference [80].

Now, for a single donor in the presence of n acceptors, if the acceptors are excited both directly by the light and through FRET, then the kinetic model of FRET (Fig. 2.7c) gives.

$$\gamma^{ex,D} p_{Da} - (\gamma^{r,Da} + \gamma^{nr,Da}) p_{D^*a} - \sum_{j=1}^{n} \gamma_j^{tr} \left(1 - \mathrm{p_{A^*d,j}}\right) p_{D^*a} = \frac{dp_{D^*a}}{dt}, \tag{2.53}$$

$$\gamma^{ex,A}\left(1 - p_{A^*d,j}\right) + \gamma_j^{tr}\left(1 - p_{A^*d,j}\right) p_{D^*a} - (\gamma^{r,A} + \gamma^{nr,A}) p_{^*d,j} = \frac{dp_{A^*d,j}}{dt}, \tag{2.54}$$

where p_{Da}, p_{D^*a}, $p_{A\,d,j}$, and $p_{A^*d,j}$, are the probabilities of finding donors and acceptors in their excited or unexcited states in the presence of each other, whereas γ^{tr} is the rate of transfer of energy from excited donor to each of the n acceptors. These probabilities obey the relations $p_{Da} + p_{D^*a} = 1$ and $p_{A\,d,j}, + p_{A^*d,j} = 1$. For single-photon excitation, the excitation rates of the fluorophore obey the following relation.

$$\gamma^{ex,X} = I\mathcal{E}^{\mathrm{x}}(\lambda_{ex}), \tag{2.55}$$

where X stands for A or D and *I* is the intensity of the excitation light with wavelength λ_{ex}, whereas $\mathcal{E}^{\mathrm{x}} = \varepsilon^X(\lambda_{ex}) ln(10) \lambda_{ex} (hcN_A)^{-1}$ with ε^X the extinction coefficient, h Plank's constant, c the speed of light, and N_A Avogadro's number, is an instrumental factor associated with the optics. This shows that for the single-photon excitation the excitation rate of fluorophore linearly relates to the extinction coefficient. However, in the case of two-photon excitation the excitation coefficient depends on the second power of the excitation light intensity, the effect is only the different value of excitation rate but not the kinetic behavior.

2.3.2. Fluorescence emission with and without FRET

In FRET measurements the quantum yield (Q) of donors and acceptors in the presence or absence of each other and the efficiency of energy transfer (or RRET efficiency, E) are the

fundamental quantities. In general, quantum yield is the fraction of de-excitation (energy decay) through radiative decay, i.e., the number of photons emitted divided by the total number of excitations, that determines the efficiency of the emission of the photon. The total number of excitations is equal to the sum of excitation lost through the radiative and non-radiative processes. So, the quantum yield of donors (Q^D) and quantum yield of acceptors (Q^A) in the absence of FRET and quantum yield of donors in the presence of FRET (Q^{Da}) can be expressed as,

$$Q^D = \frac{\int_{t_0}^{t} \gamma^{r,D} p_{D^*} dt}{\int_{t_0}^{t} (\gamma^{r,D} + \gamma^{nr,D}) p_{D^*} dt}, \tag{2.56}$$

$$Q^A = \frac{\int_{t_0}^{t} \gamma^{r,A} p_{A^*} dt}{\int_{t_0}^{t} (\gamma^{r,A} + \gamma^{nr,A}) p_{A^*} dt}, \tag{2.57}$$

$$Q^{Da} = \frac{\int_{t_0}^{t} \gamma^{r,D} p_{D^*a} dt}{\int_{t_0}^{t} \left[(\gamma^{r,D} + \gamma^{nr,D}) p_{D^*a} + \sum_{j=1}^{n} \gamma_j^{tr} \left(1 - p_{A^*d,j}\right) p_{D^*a} \right] dt}. \tag{2.58}$$

In the same way, the FRET efficiency (E), the number of excitations transferred from donors to acceptors divided by the total number of excitations of the donors can be expressed as,

$$E = \frac{\int_{t_0}^{t} \sum_{j=1}^{n} \gamma_j^{tr} p_{D^*a} p_{Ad,j} \, dt}{\int_{t_0}^{t} \left[(\gamma^{r,D} + \gamma^{nr,D}) p_{D^*a} + \sum_{j=1}^{n} \gamma_j^{tr} \left(1 - p_{A^*d,j}\right) p_{D^*a} \right] dt}. \tag{2.59}$$

Since the different excited-state de-excitation rates are all constant, Eq. 2.59 become,

$$Q^D = \frac{\gamma^{r,D}}{\gamma^{r,D}+\gamma^{nr,D}}, \tag{2.60}$$

$$Q^A = \frac{\gamma^{r,A}}{\gamma^{r,A}+\gamma^{nr,A}}, \tag{2.61}$$

$$Q^{DA} = \frac{\gamma^{r,D} P_{D^*A}}{(\gamma^{r,D}+\gamma^{nr,D}) p_{D^*A} + \sum_{j=1}^{n} \gamma_j^{tr} P_{D^*A,j}}, \tag{2.62}$$

$$E = \frac{\sum_{j=1}^{n} \gamma_j^{tr} p_{D^*a} p_{Ad,j}}{(\gamma^{r,D} + \gamma^{nr,D}) p_{D^*a} + \sum_{j=1}^{n} \gamma_j^{tr} \left(1 - p_{A^*d,j}\right) p_{D^*a}}. \tag{2.63}$$

Solving, we get,

$$E = 1 - \frac{(\gamma^{r,D} + \gamma^{nr,D}) p_{D^*}}{\gamma^{r,D} p_{D^*}} \frac{\sum_{j=1}^{n} \gamma_j^{tr} p_{D^*a} p_{Ad,j}}{(\gamma^{r,D} + \gamma^{nr,D}) p_{D^*a} + \sum_{j=1}^{n} \gamma_j^{tr} \left(1 - p_{A^*d,j}\right) p_{D^*a}}.$$

Now, plugging Eq. 2.60 and 2.62 in above equation, we get:

$$E = 1 - \frac{Q^{DA}}{Q^D}. \tag{2.64}$$

This is a commonly used form of the FRET efficiency.

2.3.3. FRET efficiency for ensembles of pure oligomers

An oligomer is a group of multiple molecules coupled through weak interactions or covalent bonds. To obtain the FRET efficiency and the experimentally measured quantities for pure oligomer (i.e., in the absence of free monomers), we use equation 2.64 in different forms.

So, here we introduce steady-state integrated emission [80] of D or A per molecule in the absence of FRET:

$$\Phi^D = \varepsilon^D \Pi_D Q^D, \tag{2.65}$$

$$\Phi^A = \varepsilon^A \Pi_A Q^A, \tag{2.66}$$

where $\Pi_A = \int_{t_0}^{t} p_A I(t)dt$ and $\Pi_D = \int_{t_0}^{t} p_D I(t)dt$.

Similarly, the integrated emission per donor in the presence of FRET,

$$\Phi^{Da} = \varepsilon^D \Pi_{Da} Q^{Da} . \tag{2.67}$$

With Eq. 2.64 the above Eq. 2.67 becomes,

$$\Phi^{Da} = \varepsilon^D \Pi_{Da} Q^D - \varepsilon^D \Pi_{Da} E Q^D. \tag{2.68}$$

Similarly, the integrated emission of acceptor in the presence of FRET can be expressed as,

$$\Phi^{Ad} = \varepsilon^A Q^A \sum_{j=1}^{n} \Pi_{Ad,j} + \varepsilon^D \Pi_{Da} E Q^A . \tag{2.69}$$

Now, using Eq. 2.65 and Eq. 2.67 in Eq. 2.64 and solving we get,

$$E = 1 - \frac{\Phi^{Da} \Pi_D}{\Phi^D \Pi_{Da}} . \tag{2.70}$$

Now, for constant excitation intensity $\Pi_A = \int_{t_0}^{t} p_A I(t)dt = P_D I$ and $\Pi_{Da} = \int_{t_0}^{t} p_{Da} I(t)dt = P_{Da} I$, so with this above equation becomes.

$$E = 1 - \frac{\Phi^{Da} P_D}{\Phi^D P_{Da}}. \tag{2.71}$$

Now for the case of ultrashort-pulse excitation, $\Pi_D = \Pi_{Da}$, Eq. 2.71 becomes,

$$E = 1 - \frac{\Phi^{Da}}{\Phi^D}. \tag{2.72}$$

This equation only applies to pulsed excitation and is expected to give somewhat erroneous results if used for continuous (CW) excitation, as in the case with wide-field or confocal microscopes. Additionally, to avoid the acceptors bleaching or the use of multiple wavelengths excitation while measuring the donor's emission, we can combine Eq. 2.68 and 2.69 in the absence of the acceptor's direct excitation, and we get:

$$Q^D = \frac{1}{\varepsilon^D \Pi_{Da}} \left(\Phi^{Da} + \frac{Q^D}{Q^A} \Phi^{Ad} \right). \tag{2.73}$$

Now, plugging Q^D from Eq. 2.73 and Q^{Da} from Eq. 2.67 into Eq. 2.64 we get

$$E = \left(1 + \frac{Q^A}{Q^Q} \frac{\Phi^{Da}}{\Phi^{Ad}} \right)^{-1}. \tag{2.74}$$

This expression for FRET efficiency has been purposed previously and has been utilized successfully in various applications [8, 66, 81]. Because this equation is not dependent on probabilities, it is independent of the excitation level regardless of whether excitation is performed using CW or pulse laser excitations. Along with that, it does not require additional excitation using different wavelengths.

2.3.4. FRET efficiency for mixtures of oligomers and free monomers

2.3.4.1 Determination of FRET efficiency using single wavelength excitations

Now, for the case of mixtures of oligomers and free oligomers, to estimate the emission intensity for ensembles of excited donors and acceptors, we have to multiply the previously obtained results for Φ by the total concentration of acceptors or donors' presence in the sample volume, as appropriate. Here, we consider the more general case which consists of free donors and acceptors, D-only and A-only oligomers, and we replace the probabilities with the concentration. With that Eqs. 2.68 and 2.69 can be modified in the following form.

$$F^{Da} = \varepsilon^D Q^D \{[D] + [D]_d\}\Pi_D + \varepsilon^D Q^D [D]_a \Pi_{Da} - \varepsilon^D E_{oligo} Q^D \mu_{oligo} \Pi_{Da}, \quad (2.74)$$

$$F^{Ad} = \varepsilon^A Q^A \{[A] + [A]_a\}\Pi_A + \varepsilon^A Q^A [A]_d \Pi_{Ad} - \varepsilon^D E_{oligo} Q^A \mu_{oligo} \Pi_{Da}, \quad (2.75)$$

where F^{Da} and F^{Ad} are the fluorescence of donor in the presence of acceptor and the total fluorescence of acceptor in the presence of donor. $[D]_a$ and $[A]_a$ are the concentration of donors within oligomers with acceptors and the concentration of acceptors in oligomers with donors, respectively. Whereas RR $[D]$ and $[D]_d$ are the concentration of the free donors and donors in complex with donors, respectively, and $[A]$ and $[A]_a$ are the concentration of the free acceptors and acceptors in complex with acceptors, respectively.

For simplification, let us introduce some notations:

$$F^{D'} \equiv \varepsilon^D Q^D \{[D] + [D]_d\}\Pi_D + \varepsilon^D Q^D [D]_a \Pi_{Da}, \quad (2.76)$$

$$F^{A'} \equiv \varepsilon^A Q^A \{[A] + [A]_a\}\Pi_A + \varepsilon^A Q^A [A]_d \Pi_{Ad}, \quad (2.77)$$

$$F^D_{FRET} \equiv \varepsilon^D E_{oligo} Q^D \mu_{oligo} \Pi_{Da}, \quad (2.78)$$

and

$$F^A_{FRET} \equiv \varepsilon^D E_{oligo} Q^A \mu_{oligo} \Pi_{Da}. \quad (2.79)$$

Here, we introduce the idea of apparent FRET efficiency, $E_{app,}$ of a mixture of free as well as associated donors and acceptors, which is expressed by (ref 12,15),

$$E_{app} \equiv \frac{\mu_{oligo}}{[D] + [D]_d + [D]_a} E_{oligo} \equiv \frac{\mu_{oligo}}{[D]_T} E_{oligo}, \quad (2.80)$$

where $[D]_T = [D] + [D]_d + [D]_a$, introduced for simplicity. This expression connects the FRET efficiency to the oligomeric size and configuration of the complexes.

Now, with these notations Eq. 2.74 and Eq. 2.75 become.

$$F^{Da} = F^{D'} - F^{D}_{FRET}, \tag{2.81}$$

$$F^{Ad} = F^{A'} + F^{A}_{FRET}, \tag{2.82}$$

Solving Eq. 2.78 and 2.79 we get

$$F^{A}_{FRET} \equiv \frac{Q^A}{Q^D} F^{D}_{FRET}, \tag{2.83}$$

Now, from Eq. 2.82 and 2.83, we get

$$F^{Ad} = F^{A'} + \frac{Q^A}{Q^D} F^{D}_{FRET}, \tag{2.84}$$

With this, the FRET efficiency can be defined as the extent to which the donors are quenched by acceptors due of FRET, that is:

$$E_{app} \equiv \frac{F^{D}_{FRET}}{F^D} = 1 - \frac{F^{Da}}{F^D}, \tag{2.85}$$

Assuming that the acceptors are only excited through the FRET, i.e., $F^{A'} \approx 0$, with these solving equations 2.81, 2.82, and 2.83 leads to the following expression

$$F^{D'} = F^{Da} + \frac{Q^D}{Q^A} F^{Ad}, \tag{2.86}$$

Now, solving Eq. 2.84 and 2.85, we obtain,

$$E'_{app} = \frac{1}{\left[1 + \frac{F^{Da}}{F^{Ad}} \frac{Q^A}{Q^D}\right]} = \left[1 + \frac{F^{Da}}{F^{Ad}} \frac{Q^A}{Q^D}\right]^{-1}. \tag{2.87}$$

This equation determines the apparent FRET efficiency, E_{app}, at each pixel in a fluorescence image obtained from micro-spectroscopy measurements using single wavelength excitation. Eq. 2.87 will be utilized in Chapter 4 to measure the FRET efficiency of oligomeric complexes in living cells for single wavelength excitation.

2.3.4.2. Determination of E_{app} using two-wavelength excitations

Using a single wavelength excitation with the application of FRET provides an experimental way to predict the most probable quaternary structure. Along with the estimation of FRET efficiency and the quaternary structure, there is also other information that can be achieved by using a successive second-wavelength excitation. The total signal emitting from donors and acceptors in the absence of each other can be estimated when the donor and acceptors both were present in the sample using a second, successive excitation [80]. These values alone do not provide critical information but, combined with other known measurable quantities, can allow for theoretical estimation of molar concentration [82-84]. The second excitation also addresses some potential errors associated with the direct excitation of acceptors, which is neglected in the theoretical formulation of the single wavelength excitation method. Let rewrite Eq. 2.81 and 2.84 for two-wavelength excitations methods.

$$F_1^{Da} = F_1^{D'} - F_{FRET,1}^{D}, \tag{2.88}$$

$$F_1^{Ad} = F_1^{A'} + \frac{Q^A}{Q^D} F_{FRET,1}^{D}, \tag{2.89}$$

$$F_2^{Da} = F_2^{D'} - F_{FRET,2}^{D}, \tag{2.90}$$

$$F_1^{Ad} = F_2^{A'} + \frac{Q^A}{Q^D} F_{FRET,2}^{D}, \tag{2.91}$$

where the subscripts "1" and "2" stand for the first and second excitation wavelength. Based on the notation given in Eq. 2.91, we introduce the following new notations:

$$\rho^{ex,D} = \frac{F_1^{D'}}{F_2^{D'}} \tag{2.92}$$

$$\rho^{ex,A} = \frac{F_1^{A'}}{F_2^{A'}}. \tag{2.93}$$

Hence, for a mixture of molecules in different oligomeric states, $\rho^{ex,D}$ and $\rho^{ex,A}$ can be determined by measuring F^{D} or F^{A} with the cells transformed with only the donor or only acceptor fluorophores at the two wavelengths. Note, this holds only for the pulsed excitation for which $\Pi_D = \Pi_{Da} = \Pi_A = \Pi_{Ad} = 1$ and therefore $\rho^{ex,D} = \frac{\varepsilon_1^D}{\varepsilon_2^D}$ and $\rho^{ex,A} = \frac{\varepsilon_1^A}{\varepsilon_2^A}$.

Now, dividing Eq. 2.88 by Q^D and Eq. 2.89 by Q^A and adding up the expressions, we get:

$$\frac{F_1^{Da}}{Q^D} + \frac{F_1^{Ad}}{Q^A} = \frac{F_1^{D'}}{Q^D} + \frac{F_1^{A'}}{Q^A}. \tag{2.94}$$

Similarly, from Eq. 2.90 and Eq. 2.91, we obtain:

$$\frac{F_2^{Da}}{Q^D} + \frac{F_2^{Ad}}{Q^A} = \frac{F_2^{D'}}{Q^D} + \frac{F_2^{A'}}{Q^A}. \tag{2.95}$$

Plugging $\mathrm{F}_1^{\mathrm{D}'}$ and $\mathrm{F}_1^{\mathrm{A}'}$ from Eq. 2.92 and 2.93, respectively, into Eq. 2.94 and dividing the resulting equation by $\rho^{\mathrm{ex,D}}$, we get:

$$\frac{F_1^{Da}}{Q^D}\frac{1}{\rho^{ex,D}} + \frac{F_1^{Ad}}{Q^A}\frac{1}{\rho^{ex,D}} = \frac{F_2^{D'}}{Q^D} + \frac{F_1^{A'}}{Q^A}\frac{\rho^{ex,A}}{\rho^{ex,D}}. \tag{2.96}$$

Then, subtracting Eq. 2.95 from Eq. 2.94 and rearranging the terms, we get:

$$F_2^{A'} = (F_2^{Ad} - F_1^{Ad}\frac{1}{\rho^{ex,D}} + F_2^{Da}\frac{Q^A}{Q^D} - F_1^{Da}\frac{1}{\rho^{ex,D}}\frac{Q^A}{Q^D})(1 - \frac{\rho^{ex,A}}{\rho^{ex,D}})^{-1}.. \tag{2.97}$$

For pulse excitation, $\Pi_D = \Pi_{Da} = 1$, which yiled (using equation 32a and S2a) $F_1^{Da}/F_2^{Da} = \rho^{ex,D}$, for this case Eq. 2.97 becomes.

$$F_2^{A'} = (F_2^{Ad} - F_1^{Ad}\frac{1}{\rho^{ex,D}})\left(1 - \frac{\rho^{ex,A}}{\rho^{ex,D}}\right)^{-1} . \quad (2.98)$$

Further, by solving Eq. 2.94 for $F_1^{D'}$ and plugging $F_1^{A'}$ from Eq. 2.93, we obtain

$$F_1^{D'} = F_1^{Da} + F_1^{Ad}\frac{Q^D}{Q^A} - F_2^{A'}\rho^{ex,A}\frac{Q^D}{Q^A} . \quad (2.99)$$

Now by inserting $F_1^{D'}$ from Eq. 2.99 into Eq. 2.85, we obtain:

$$E'_{app} = \left(1 + \frac{F_1^{Da}}{F_1^{Ad} - F_2^{A'}\rho^{ex,A}}\frac{Q^A}{Q^D}\right)^{-1} , \quad (2.100)$$

where $F_2^{A'}$ is determined from experiments with Eq. 2.98. For pulse excitation, we may substitute $F_2^{A'}$ from Eq. 2.98 into Eq. 2.100 and obtain:

$$E'_{app} = \left(1 + \frac{F_1^{Da}\left(1 - \frac{\rho^{ex,A}}{\rho^{ex,D}}\right)^{-1}}{F_1^{Ad} - F_2^{Ad}\rho^{ex,A}}\frac{Q^A}{Q^D}\right)^{-1} . \quad (2.101)$$

Using Eq. 2.201, we can determine the FRET efficiency in the presence of the direct excitation of acceptors using additional (i.e., second) excitation wavelength while using pulse excitation. Eq. 2.101 will be utilized in Chapter 4 to measure the FRET efficiency of oligomeric complexes in living cells using two-wavelength excitations.

2.3.5. Determination of molecular concentration

2.3.5.1. Donor concentration

To measure the donor concentration experimentally, we may use single wavelength excitation with no direct excitation of the acceptor, so the donor and acceptor are chosen in such a way that there will be no direct excitation of acceptors.

From Eq. 2.76 and 2.77, the donor-only and acceptor-only fluorescence emissions may be expressed as

$$F^{D'} = \varepsilon^{D} Q^{D} [D]_{T} \Pi_{D,} \tag{2.102}$$

$$F^{A'} = \varepsilon^{A} Q^{A} [A]_{T} \Pi_{A}. \tag{2.103}$$

After combining Eq. 2.81 and 2.83, we have:

$$F^{D'} = F^{Da} - \frac{Q^{D}}{Q^{A}} F^{Ad}. \tag{2.104}$$

Now, combining Eq. 2.102 and 2.104, we obtain:

$$[D]_{T} = \frac{1}{\varepsilon_{1}^{D} Q^{D} \xi} \left(F^{Da} - \frac{Q^{D}}{Q^{A}} F^{Ad} \right). \tag{2.105}$$

Here, we substituted $\Pi_D = 1$ for pulse excitation, the instrumental factor ξ account for detection laser excitation power, detection sensitivity, etc.

2.3.6.1. Acceptor concentration

To determine the acceptor concentration, we use two-wavelength excitations method, the first excitation wavelength chosen in such a way that $\rho = F_{1}^{A'} / F_{2}^{A'} = 0$. With this condition by combining Eq. 2.103 and Eq. 2.98, we can obtain the following expression for the acceptor concentration.

$$[A]_{T} = \frac{1}{\varepsilon_{1}^{A} Q^{A} \xi} \left(F_{2}{}^{Ad} - F_{1}^{Ad} \frac{1}{\rho^{ex,D}} \right). \tag{2.106}$$

Here, we substituted $\Pi_A = 1$ for pulse excitation, the instrumental factor ξ account for detection laser excitation power, detection sensitivity, etc. Then the total concentration can be obtained as the sum of the donor and acceptor concentration.

2.4. Prediction of FRET efficiency using kinetic theory of FRET

2.4.1. Prediction of FRET efficiency

In a protein complex containing *n* protomers, with *k* donors and *n-k* acceptors, the FRET efficiency of each individual donor, *i*, is a function of the energy transfer rates occurring between the donor and each of the acceptors in the complex, according to the following expression [85]:

$$E_{i,k,n} = \frac{\sum_{j=1}^{n-k} \Gamma_{i,j}^{FRET} / (\Gamma^{r,D} + \Gamma^{nr,D})}{1 + \sum_{j=1}^{n-k} \Gamma_{i,j}^{FRET} / (\Gamma^{r,D} + \Gamma^{nr,D})}, \quad (2.107)$$

where the summation index j represents a sum over all of the acceptors present in the oligomeric complex. $\Gamma^{r,D}$ and $\Gamma^{nr,D}$ are the rate constants of de-excitation through radiative (i.e., photon emission) and non-radiative (e.g., internal conversion) processes, respectively, and $\Gamma_{i,j}^{FRET}$ is the rate constant for FRET between the i^{th} donor and j^{th} acceptor.

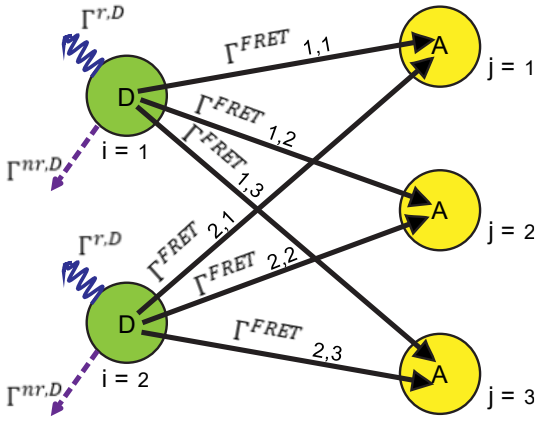

Figure 2.8. Schematic representation of a pentamer with two donors (D) and three acceptors with possible pathways for energy loss from excited donors. Green circles represent the donors (D), and yellow circles represent acceptors (A) fluorescent molecules. The various arrows indicate possible pathways through which the excited donor loses energy. Wavy arrows indicate radiative loss ($\Gamma^{r,D}$), dashed arrows indicate non-radiative loss ($\Gamma^{nr,D}$), and solid arrows pointing toward A from D depict energy transfer through FRET (Γ^{FRET}). Figure is adapted from reference [85].

The apparent FRET efficiency for a given complex can be predicted by averaging the $E_{i,k,n}$ values from each individual donor:

$$E_{pred} = \frac{1}{k}\sum_{i=1}^{k} E_{i,k,n} = \frac{1}{k}\sum_{i=1}^{k} \frac{\sum_{j=1}^{n-k} \Gamma_{i,j}^{FRET}/(\Gamma^{r,D} + \Gamma^{nr,D})}{1 + \sum_{j=1}^{n-k} \Gamma_{i,j}^{FRET}/(\Gamma^{r,D} + \Gamma^{nr,D})}. \qquad (2.108)$$

If the protein complex contains only one donor (k = 1), as is the case for all of the constructs in this study, Eq. 2.108 simplifies to [85]:

$$E_{pred} = \frac{\sum_{j=1}^{n-1} \Gamma_{1,j}^{FRET}/(\Gamma^{r,D} + \Gamma^{nr,D})}{1 + \sum_{j=1}^{n-1} \Gamma_{1,j}^{FRET}/(\Gamma^{r,D} + \Gamma^{nr,D})}. \qquad (2.109)$$

2.4.2. FRET efficiency of multimeric complexes

For multiplexes containing only one donor and more than one acceptor, the predicted FRET efficiency can be calculated using Eq. 2.109 if all the individual rates between the donor and each acceptor, $\Gamma_{1,j}^{FRET}$, are known. The relationship between the FRET efficiency of a complex containing a single D and single A and the rate of energy transfer between the D and A is given as:

$$E_j = \frac{\Gamma_{i,j}^{FRET}}{\Gamma^{r,D} + \Gamma^{nr,D} + \Gamma_{i,j}^{FRET}}, \tag{2.110}$$

Combining Eq. 2.109 with Eq. 2.110 results in:

$$E_{pred} = \frac{\sum_{j=1}^{n-1} E_j / 1 - E_j}{1 + \sum_{j=1}^{n-k} E_j / 1 - E_j}, \tag{2.111}$$

where j is the different pathway of energy transfer, i.e., different pairs of D and Acceptor present in the given multimeric complexes. FRET efficiency of multimeric complexes can be calculated using Eq. 2.111 using FRET efficiencies of all possible individual donor (D) and acceptor (A) pairs in the configuration.

2.4.3. Overview of the kinetic theory of FRET and its experimental testing

With regard to potential applications of FRET in determining the quaternary structure of macromolecules, it is important to understand how FRET behaves when multiple donor and acceptors are close proximity. The first rigorous treatment of the kinetic theory of FRET was published in 2007 [85], which was further refined in 2019 [86]. This theory provides a theoretical basis for predicting the FRET occurring in multimeric complexes. According to the theory, the FRET efficiency of an oligomer containing multiple acceptors can be predicted

based on the FRET efficiency between each individual donor-acceptor pathway within the complex.

In 2009, the first attempt of experimental testing of the kinetic theory of FRET was performed by Kaushik et al. [87] by measuring the ensemble FRET efficiency of the construct containing a single fluorescence molecule Cerulean (a donor of energy, D) and two fluorescent molecule Venus (an acceptor of energy, A), see Fig. 2.8. The FRET efficiency of the given construct was determined from measurements as well as estimated using measured FRET efficiency of individual donor-acceptor pairs present within these constructs utilizing the kinetic theory of FRET. The FRET measurements for each construct were taken from the transfected HEK 293 cells with the required construct in a culture medium. The FRET efficiency in each individual donor-acceptor pair was measured systematically by eliminating all other acceptors by introducing point mutation, a non-fluorescence place holder (N), in the original construct. In this investigation, the FRET efficiency was estimated with two methods: sFRET and E-FRET. The sFRET was performed using two-wavelength excitations based on the spectral unmixing of the spectral images, whereas, E-FRET is a method of measuring FRET efficiency based on acceptor desensitization using a one-photon excitation source [87].

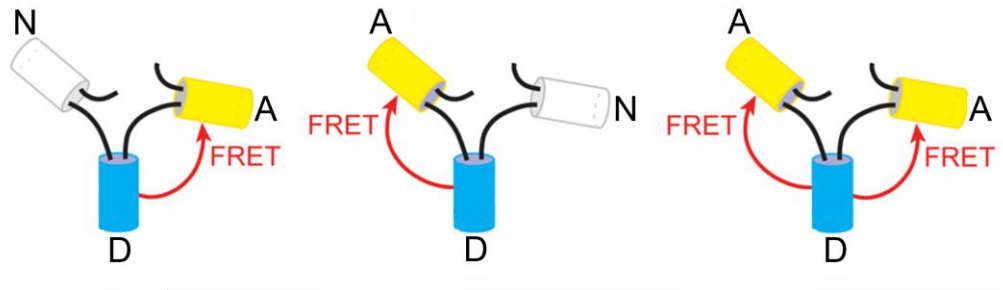

Figure 2.9. Schematic representation of cytoplasmic FRET constructs with energy transfer pathways from the excited donor to the nearby acceptors. White cylinders represent Amber (a non-fluorescent structural placeholder, N), cyan cylinders represent the fluorescent molecule Cerulean (a donor of energy, D), and yellow cylinders represent the fluorescence molecule Venus (an acceptor of energy, A). The solid arrows pointing toward A from D depict energy transfer through FRET. The figure is adapted with the permission of reference [87].

Table 2.1. Comparison of FRET efficiency of constructs ADN, NDA, and ADA measured using sFRET, E-FRET, and the acceptor to donor ratio (A/D) for each construct.

	ADN	**NDA**	**ADA**
FRET efficiency	0.44± 0.08	0.36± 0.09	0.64± 0.05
(sFRET)	Mean ± SD, n=26	Mean ± SD, n=26	Mean ± SD, n=16
FRET efficiency	0.45± 0.04	0.38± 0.03	0.69± 0.05
(E-FRET)	Mean ± SD, n=82	Mean ± SD, n=52	Mean ± SD, n= 59
A/D	0.96± 0.09	0.95± 0.097	1.96± 0.17
(E-FRET)	Mean ± SD, n=82	Mean ± SD, n=52	Mean ± SD, n=59

On the other hand, the predicted FRET efficiency of the ADA construct based on the kinetic theory of FRET using equation 2.72 is 0.58± 0.01 for sFRET and 0.59 ± 0.01 for E-FRET. Comparing the measured and predicted FRET efficiency of ADA, it is found that the amount of energy transferred to the acceptors was significantly greater than predicted using the kinetic theory of FRET. Based on these results, the authors claim that the Kinetic model of FRET failed to predict the FRET efficiency. They suggest that there might exist some additional

pathways of energy transfer between the donor and the acceptor besides FRET in the case of multiplex containing one donor and multiple acceptors.

In 2015, an experimental test was performed using the same construct by Patowary et al.[88] using two-photon excitation in conjunction with spectral FRET. They observed a much smaller discrepancy (of ~ 4 %) between measured and predicted FRET efficiency than previously reported by Koushik et al. [87]. This study reconfirmed that the kinetic theory of FRET can predict the FRET efficiency of multiplex containing one donor and multiple acceptors. This experimental test suggests that the previous study by Kaushik et al. may have overlooked some important experimental (or calibration) factors in the formulation of FRET which resulted in significant systematic errors.

Soon after, in 2017, a test of the kinetic theory of FRET was performed by King et al. [89] using Monte Carlo simulations on membrane protein receptors forming constitutive monomers, dimers, or oligomers for different values of surface density. The simulated total apparent FRET efficiency was estimated by generating 2,700 data points at random total concentrations with variable acceptor molar fractions and adding random error for each data point using Gaussian distribution. Several distinct sizes of oligomers, ranging from dimers to hexamers, were used for the simulations. For each order of the oligomerization, the simulated results were fitted with two different models; the Veatch and Stroyer model[90] and the kinetic model of FRET[85], to describe the dependence of the FRET efficiency measured in an experiment on the interpolymeric FRET due to random proximity within the bilayer and the interpolymeric FRET resulting from protein-protein interactions. It was found that the size of oligomers for dimers at high protein concentration was not predicted correctly with the Veatch and Stryer model. Whereas the fitting result with the kinetic model of FRET correctly predicted

the size of dimers or tetramers at all the concentration values of the simulated data. The agreement of the kinetic model of FRET with numerical simulation confirms the validity of the kinetic theory of FRET theoretically.

Later, in 2019, utilizing the kinetic model of fluorescence in the presence and absence of FRET, a set of rigorously derived FRET equations provided insights into the old puzzles presented in the FRET theory [86]. The in-depth analysis of the FRET relationship with measurable fluorescence quantities reveals some anticipated results and a few unexpected explanations for known experimental FRET puzzles, which helps identify the associated errors and theoretical background for optimizing measurement strategies. In the next section (i.e., in section 2.4), we will describe the systematic errors associated with the old FRET puzzles and strategies to optimize measurements based on this study [86].

2.5. Systematic errors in FRET calculations

2.5.1. Errors caused by integrated probability dependency of FRET efficiency

An oligomer (or oligomeric complex) is a group of two or more molecules associated together with the week interaction, such as, van der Walls interaction, or covalent bonds. The efficiency of energy transfer for pure oligomer under continuous wave (CW) excitation can be obtained with experimentally measured quantities using Eq. 2.71,

$$E = 1 - \frac{\Phi^{DA} P_D}{\Phi^{D} P_{DA}}.$$

where Φ^{DA} and Φ^{D} are the emission intensity of donor in the presence and in the absence of acceptor, respectively. P_D and P_{DA} are the probability of finding donors in their excited state in the absence and in the presence of acceptor, respectively. For CW excitation P_D and P_{DA} are always less than unity.

In case of ultrashort-pulse excitation there is always a chance of finding donors in their excited state i.e., $P_D = P_{DA} = 1$, with this we obtained Eq. 2.72,

$$E = 1 - \frac{\Phi^{DA}}{\Phi^{D}}.$$

This equation is a widely used equation to determine the FRET efficiency from steady-state fluorescence intensities for pulse excitation. Nevertheless, this equation can lead to an erroneous result if it is used for CW excitation. Also, we can see that for the case of pulse excitation, the FRET efficiency (i.e., in equation 2.72) is independent of the integrand probability (i.e., probability of molecules presents in their excitation state). So, the possible systematic errors associated with integrated probability dependency of FRET efficiency can be avoided by using pulse excitation

2.5.2. Potential errors in the presence of direct excitation of acceptor

As described in section 2.3.1, the FRET efficiency in the case of single-wavelength excitation method can be determined using the following equation.

$$E_{app} = \left[1 + \frac{Q^A k^{DA} w^D}{Q^D k^{AD} w^A}\right]^{-1}, \qquad (2.112)$$

where Q^D and Q^A are the quantum yield of donor and acceptor, respectively. k^{DA} and k^{AD} are the donor fluorescence in the presence of acceptor and acceptor fluorescence in the presence of donor, respectively. w^D and w^A are the integral of the emission spectrum of D and A, respectively.

In the presence of direct excitation of acceptor, Eq. 2.112 overestimates the FRET efficiency. The FRET efficiency can estimate correctly using Eq. 2.112 only if there is no or negligible direct excitation of the acceptor. So, in the single wavelength excitation method, the

excitation wavelength should be chosen in such a way that it mostly excites the donors with no or negligible direct excitation of the acceptor. To avoid such errors, we can also use two-successive wavelengths excitation method as described in section 2.3.2.

2.5.3. Errors associated with photophysical effects of FPs

In the dual-wavelength excitation method, the sample cells were excited successively with two excitation wavelengths one after another. This method overcomes associated errors caused by direct excitation of the acceptor in FRET calculation using single-wavelength excitation. In addition, the two-wavelength excitation method incorporates photophysical effects of the FP during the measurement to some extent. To include such effects in the FRET calculation, some calibration factors, such as $\rho^{ex,D}$ and $\rho^{ex,A}$, were introduced as described previously in Eq. 2.101,

$$E'_{app} = \left[1 + \frac{F_1^{Da}(1 - \rho^{ex,A}/\rho^{ex,D})}{F_1^{Ad} - F_2^{Ad}\rho^{ex,A}} \frac{Q^A}{Q^D}\right]^{-1}.$$

However, the theoretical assumptions used in the formulas used to compute FRET efficiency from experimental data may lead to systematic errors if not carefully considered in the context of the experimental protocols used. For instance, if the FRET measurements were performed in cells and the parameters (i.e., $\rho^{ex,D}$ and $\rho^{ex,A}$) were performed in an aqueous solution, where the molecules in the solution diffuse faster than inside the cell and, therefore, are less susceptible to photobleaching or photo-switching. As a result, it may cause an erroneous estimation of the FRET efficiency, which may explain the possible cause for the wider discrepancy in Koushik et al. [87]. Additionally, the two-wavelength excitations may add up more photophysical effects due to two successive excitations. These facts and puzzles suggested

possible explanations for the small but significant differences between measured and predicted FRET efficiencies in the study by Patowary et al. [88]. Our attempt at clarifying remaining differences between theory and experiment started with investigating the photophysical effects of fluorescence proteins (see Chapter 3) and continued with a systematic analysis of their effects on FRET measurements which will described in detail chapter 4.

Chapter 3. Photophysical properties of fluorescent proteins (FPs)

In this chapter, we report our investigations of the photophysical properties of several commonly used fluorescent proteins (FPs) using two-photon microscopy with spectral resolution in both excitation and emission [7, 91]. The study of photophysical effects of FPs begins with a brief introduction to the photophysics effects of some commonly used FPs and a quantitative description based on previous studies conducted under single-photon excitation, as outlined in Section 1.3 of the Chapter 1. Here in this chapter, we perform a comparative analysis of the photophysical effects induced by light of different wavelengths of these fluorescence proteins (FPs) is presented to provide general guidelines for choosing the right tag(s) for the desired experiments under two-photon excitation. This chapter contains four sections, whereas the first section presents a brief literature review on this topic. The second section describes the materials and methods utilized to study the photophysical effects of FPs under two-photon excitation conditions. Then, the results of this investigation are presented in the third section, while the fourth section presents a brief discussion of the results on their significance. Understanding the photophysical effects of FPs may help avoiding these effects and associated errors on FRET measurements. The consequences of the photophysical effects of contributing FPs on FRET measurements will be studied in detail in Chapter 4.

3.1. Photophysical properties of FPs

Fluorescent proteins (FPs) have proved to be powerful tools in applications where photolabeling and tracking targeted objects in living cells and organisms is desired. Following the discovery and purification of the wild-type green fluorescent protein (wtGFP) from the jellyfish *Aequorea victoria* [1], researchers have engineered a wide palette of GFP variants with diverse spectral

characteristics, i.e., wavelength-shifted absorbance and/or emission spectra. In addition to the proteins derived from *Aequorea Victoria*, a large number of FPs which are homologous to wtGFP have been found to occur naturally in other species, e.g., Anthozoa corals [3] and Clavularia coral [4]. In recent years, researchers have expanded the FP palette by producing many variants of coral-derived FPs [3, 4].

Each individual protein in the vast FP library exhibits a unique combination of photophysical qualities, including excitation and emission spectra, brightness, photostability, and sensitivity to external conditions such as pH. These differences have been exploited in several types of studies. For example, localization and colocalization studies in which different macromolecules are tracked within a cell need FPs with distinct spectra when the molecules of interest can be colocalized in the same pixel [5, 52, 92, 93]. In another example – that of FRET applied to the determination of protein association stoichiometry – fluorescent proteins with different spectral properties [5, 6, 11, 94-96] ensure that the emission maxima of the donor and acceptor are distinguished from each other while at the same time the emission spectrum of the donor and excitation spectrum of the acceptor overlap considerably in order for resonance energy transfer (RET) to occur [66, 97]. In other experiments, it is the propensity of the fluorescent proteins to photobleach under repeated excitation with laser light that is being exploited in order to determine molecular complex stoichiometry [98, 99].

In addition to the emission and excitation spectra, a major consideration when choosing an FP for use in a fluorescence imaging technique is the overall brightness, which is a measure of the amount of light emitted by the FP. The brightness of an FP is a function of intrinsic properties of the FP, e.g., the extinction coefficient and quantum yield, environmental factors, such as pH and temperature, and instrumentation settings, such as the excitation light intensity

and excitation wavelength [12, 59]. In order to be reliably imaged, the brightness of an FP should be chosen such that it provides sufficient signal above the background noise and cellular autofluorescence signal. Choosing an FP with a relatively high brightness value allows one to lower the excitation power or expression level (or both), which is typically advantageous in many fluorescence imaging techniques.

Over the past two decades robust imaging tools have been developed using 2p excitation [66, 100, 101], and there is an abundance of studies of 2p fluorescence, such as 2p absorption cross-section of FPs [12], fluorescence dynamics of single GFP molecules [102], and single-particle photophysical properties of commercial quantum dots [103]. However, most of the time, a newly developed fluorescent protein is characterized and advertised based on its single-photon-derived spectroscopic properties, and there is still very limited information available on photobleaching and photo-switching properties of many FPs under 2p excitation, while the 2p relative brightness of various fluorescent proteins is not consistently reported.

The relative brightness under two-photon (2p) excitation of the various FP variants, which is proportional to the 2p absorption cross-section [104], cannot be inferred directly from the relative brightness of the same FPs measured using the more common one-photon (1p) excitation. In other words, just because a particular FP is brighter than another one under 1p excitation, it is not necessarily brighter under 2p excitation. Hence, detailed measurements with 2p excitation are necessary to estimate 2p brightness, which helps researcher to choose the most appropriate FP for a 2p based fluorescence imaging technique.

While the absorption/emission spectrum and brightness are typically given the most attention when choosing the correct FP, the photostability of the FP is also an important characteristic to keep in mind when selecting the correct FP for long-term (i.e., repeated

measurements) or alternating excitation wavelengths fluorescence imaging. The photostability of an FP is its ability to emit a steady fluorescence signal by resisting photophysical (or photochemical) changes during its optical excitation. Since in an excited state a molecule may be chemically reactive, fluorescent molecules are highly likely to interact with nearby molecules, such as oxygen, and thus change their properties permanently [105]. Multiple factors contribute to the overall photostability of an FP, namely the extent to which the FP undergoes photobleaching [105, 106] and photo-switching [42, 107], which will be described in more detail next.

In fluorescence microscopy, photobleaching is a common phenomenon that occurs when a fluorophore permanently loses its ability to fluoresce due to photo-induced chemical changes. Depending upon the molecular structure and the local environment, a fluorescent molecule can go through a certain number of excitation and emission cycles before it completely loses its ability to fluoresce. Hence, a prolonged exposure to excitation light can destroy the ability of the fluorescent molecule to fluoresce [106]. Photobleaching is a complex phenomenon that depends on multiple factors, including the power of the excitation light and the time of FP exposure to it, along with whether the surrounding environment is oxidizing or reducing. Generally, photobleaching is stronger in response to excitation wavelengths corresponding to the peak of the excitation spectrum of the FP, because the FP will go through excitation and emission cycles at a higher rate using this wavelength and hence be more prone to photobleaching.

Photo-switching occurs when fluorophores undergo a change in their spectral properties in response to irradiation with light of a specific wavelength and intensity [107-109]. Photo-switchable FPs are categorized into three broad classes: irreversibly photo-switchable from a

dark to a bright state (i.e., from non-fluorescent to fluorescent), irreversibly photo-switchable from one emission color to another, and reversibly photo-switchable enabling bright-to-dark switching capability [108, 110]. In the case of irreversibly photo-switchable from a dark to a bright state, the peak wavelength of the excitation spectrum changes and, sometimes, can shift to a different excitation wavelength as the chromophore changes from the neutral (protonated) state to anionic (deprotonated) state in response to the irradiation of light of certain wavelength and intensity [110, 111].

Both attributes described above (i.e., photobleaching and photo-switching), are the two main factors that determine the photo-stability of an FP. Lack of photo-stability in an FP is often detrimental but sometimes desirable in measurements. For a gamut of fluorescence-based techniques, such as FRET [8, 97, 112], FCS [113, 114], and fluorescence intensity fluctuation (FIF) spectroscopy [101, 115], FPs with high photostability are preferable. Multiple scans or long-term scans of a fixed region of interest is common in these methods to follow the dynamic nature of the biological system of interest at the molecular level. In these techniques, it is expected that the first excitation does not significantly alter the usual behavior of the FP in the next excitation.

There are also situations when photobleaching is useful. For example, fluorescence recovery after photobleaching (FRAP) [116], which allows one to monitor the diffusion of fluorescent molecules as they diffuse into a photobleached region immediately following excitation due to high-intensity laser light. In addition, identification of the number of molecules within a supra-molecular complex has become possible by counting photobleaching steps in single-molecular complex measurements [98, 99]. Likewise, development of photo-switchable FPs has helped advance fluorescence imaging techniques and permitted optical

control of protein activity [42, 117], information storage [118], and super-resolution imaging [107]. Having a good understanding of the photophysical properties of FPs, therefore, is essential for choosing the right tag(s) for a desired experiment. Numerous studies have been published characterizing the photophysical properties of GFP variants using confocal microscopy [13, 119].

In this study, we present a comparative analysis of the photophysical properties under two-photon excitation of some widely used FPs. These investigations have been performed via two-photon micro-spectroscopy with spectral resolution in both the excitation and emission channels [7, 66], with the aim of providing guidelines for screening of FPs as tags in various 2p fluorescence microscopy applications. We used purified FPs embedded in a polyacrylamide gel, which allowed us to scan the same molecules successively a number of times in order to measure the fluorescence intensity as a function of scan number, as well as excitation and emission wavelengths. By quantifying the fluorescence intensity and monitoring changes in the emission and excitation spectra of an FP occurring due to repeated scans using a pair of excitation wavelengths, we were able to quantify the level of photobleaching for each FP as well as to determine whether a particular FP underwent photo-switching. We have also estimated the 2p brightness (relative to mEGFP) of each FP by performing z-stack acquisitions of FP-doped gels (see section 2.5 below) using an excitation wavelength that corresponds to the peak of the FP's 2p excitation spectrum. Comparing our 2p-excitation measurements to single-photon measurements reported in the literature, we conclude that not only the excitation (and sometimes emission) spectra, but also the photobleaching, photo-switching, and brightness properties of FPs may be markedly different under single-photon and two-photon excitation.

3.2. Materials and methods

3.2.1. Preparation of stock solutions

For the experiments presented herein, we prepared several stock solutions for use in making the polyacrylamide gels embedding fluorescent proteins. All reagents were either purchased from Fisher Scientific, or otherwise specified below. A 10% ammonium persulfate (AP; Sigma-Aldrich, MO) solution, prepared by dissolving 0.1 g of AP in doubly distilled (DD) water to a final volume of 1 ml, was used for inducing the polymerization of the polyacrylamide (PAA) solution. A 30% PAA stock solution was prepared by dissolving 6 g of powder polyacrylamide (PAA; Sigma-Aldrich, MO) and 0.3 g of bis-acrylamide (BAA; Sigma-Aldrich, MO) in DD water to a final volume of 20 ml of solution. This solution was then mixed thoroughly using a 3D nutating shaker (BioMixer; Benchmark Scientific Inc., NJ) for at least one hour, and thereafter the solution was degassed under a vacuum of 0.1 m^3/s for 30 minutes at room temperature. Finally, a number of different phosphate-buffered saline solutions were prepared at various pH values; the final pH of each solution was achieved by addition of NaOH or HCl to a stock solution of Dulbecco's phosphate buffered saline (DPBS; REF: 14190-144, Life Technologies, NY). All stock solutions were stored at 4°C and were used in the preparation of FP-doped polyacrylamide gel samples (see section 2.3 below) for up to two weeks after their initial preparation date.

3.2.2. Glass surface cleaning

All glass slides and coverslips were cleaned following a rigorous, multi-step process before use. A clean surface is essential to prevent undesirable signals that may arise due to excitation of unwanted surface impurities. For example, organic or inorganic matter located at the plane of

excitation (i.e., on the surface), during the fluorescence measurements. In addition, preparation of slides and coverslips in this manner also helped to prevent binding of the FPs to the surface. For this, glass slides were kept in acetone for at least 24 hours. The coverslips were kept in piranha solution (a 3:1 mixture of sulfuric acid and 30% hydrogen peroxide) for 24 hours, and then rinsed with DD water, and acetone sequentially. Next, both glass slides and coverslips were dried with clean, dry, compressed air and then treated with oxygen plasma by exposing them to the wire electrode of a plasma generating device (BD-20AC Laboratory Corona Treater; Electro-Technic Products, IL) for approximately 15 min [120, 121]. The cleaned slides were used immediately, i.e., FP-doped polyacrylamide gel (see section 2.3 below) samples were deposited on the slides within minutes after being treated with the oxygen plasma.

3.2.3. Preparation of FP-doped polyacrylamide gel samples

The fluorescent proteins mGFP2 [52, 66], mEGFP [38, 43, 122], mYFP [26], mCitrine [35, 53], SYFP2 [55], mVenus [53, 55], mTurquoise (mTq) [58], mCerulean3 [57], and mTFP1 [4] were expressed and purified using standard bacterial expression systems. Note that the "m" before the fluorophore name refers to the fact that it contains the A206K point mutation, to reduce dimerization [123]; the same mutation was incorporated also into SYFP2, although in the literature "m" is usually omitted from its name. The plasmid DNA was transformed into C41(DE3) chemically competent cells, which were then grown in LB buffer at 37 ^{o}C, in the presence of antibiotic (carbenicillin), until the culture showed an absorption optical density at 600 nm $O.D._{600}$ = 0.6. Following the growth phase, protein overexpression was induced by treating the cultured bacteria with 1mM IPTG (VWR Life Science) overnight at 25 ^{o}C. Finally, chloramphenicol was added at a final concentration of 200 μg/ml for 2 hours, to allow for

fluorophore maturation. Cells were then lysed chemically (with DNAse, RNAse, and lysozyme) and mechanically (through sonication). The soluble fraction was passed through a Ni-NTA column (Fisher Scientific), which bound the protein of interest through their polyhistidine tag. Following washing and elution with 250 mM imidazole, the protein of interest was further purified using size exclusion chromatography (AKTApure, GE with S300 column). Unless otherwise mentioned, all chemicals and competent cells were purchased from Sigma-Aldrich.

Purified proteins were then embedded separately at desired concentrations in polyacrylamide (PAA) gel following a method by Dickson et al [124] and using the stock solutions described in section 2.1. The average size of the gel pores may be tuned from 2 nm to several hundred nm in diameter [124, 125] by altering the acrylamide and cross-linker final concentrations. In all of our samples, we used final concentrations of 15% (w/w) for the acrylamide gel and 5% (w/w) cross-linker to achieve pore sizes of approximately 2 nm.

The FP-doped PAA gel was prepared by first adding 244 µL DPBS buffer of known pH, 244 µL of 30%-PAA stock solution, 12.5 µL of 40 µM FP of interest, 2.4 µL of 10% AP stock solution, and 0.5 µL Tetramethylethylenediamine (TEMED; Sigma-Aldrich, MO) sequentially to an Eppendorf tube to achieve a solution with a final FP concentration of 1 µM. Thereafter, the solution was vortexed for 5 to 10 seconds to ensure homogeneity. The gel was left undisturbed at room temperature for three minutes after vortexing, and then 7.5 µL of the gel was pipetted onto the surface of a freshly cleaned glass slide before it being sandwiched between the glass slide and a clean coverslip (see Section 2.2 above). Approximately three minutes after the sample was placed between the glass slide and coverslip, the sample was fully polymerized. In order not to avoid photobleaching of the FPs before micro-spectroscopic measurements, we covered the slide with aluminum foil.

Each FP sample was prepared and measured under the same environmental conditions. Exposure to fluorescent light with wavelengths which could potentially photobleach the FPs was avoided by preparing all samples in a room where the only illumination was from a dim yellow fluorescent light bulb. The fluorescent-protein-doped samples were measured immediately after preparation to avoid complete evaporation of water from the gel. The measurements, which took 3 to 4 hours, were performed in a dark room. Finally, positioning the FP-doped gel within the focal plane of the optical micro-spectroscope (see Section 2.4 below) was accomplished using a lower laser intensity (compared to the actual measurements) to avoid unwanted photophysical effects before the actual measurements were performed.

3.2.4. Two-photon (2p) excitation micro-spectroscopy measurements

The instrumentation used to carry out 2p excitation micro-spectroscopic measurements in this investigation has been described previously [66, 91]. Briefly, measurements were performed with a 2p optical micro-spectroscope comprised of an inverted Nikon Eclipse Ti^{TM} microscope (Nikon Instruments, Inc., Melville, NY) and an OptiMiS^{TM} scanning/detection head (Aurora Spectral Technologies, Grafton, WI) equipped with a line-scan module. A mode-locked Ti-Sapphire laser (Mai Tai^{TM}, Spectra Physics, Santa Clara, CA) which generates 100 fs pulses with central wavelengths tunable between 690 nm and 1040 nm was used for the fluorescence excitation. The excitation beam was focused into a line in the sample by an infinity corrected oil-immersion objective with 100× magnification. The OptiMiS detection head used a non-descanned detection scheme in which emitted light was spectrally resolved by passing it through a transmission grating and projecting onto a cooled electron-multiplying charge-coupled device (EMCCD) iXon Ultra 897 cameras (Andor Technologies, South Windsor, CT).

The emission wavelengths of the fluorescence were separated as a function of pixel position on the EMCCD array. For all the measurements we have used a fixed spectral resolution of 5 nm, which allowed us to capture 2D fluorescence images for 40 different wavelength channels ranging from 415 nm to 615 nm.

To characterize the photostability of the fluorescent molecules, we performed a series of micro-spectroscopic measurements (what is hereby referred to as an excitation time series) using two different excitation wavelengths; each series of measurements was performed on the same region of interest (ROI) within a particular sample. Specifically, an excitation time series was carried out on a sample by first scanning the sample ten successive times using a fixed wavelength (e.g., 960 nm for mGFP2). Then, an additional set of ten scans was performed while using a different excitation wavelength (e.g., 800 nm for mGFP2). This process of alternating between a series of ten scans at two different excitation wavelengths was repeated two (or three) additional times, meaning that each sample was scanned in the same location a total of thirty (or, in some cases, forty) times for each of the two different excitation wavelengths, to detect possible effects of photo-switching. For both excitation wavelengths, an average laser light power (measured in the sample plane) of 200 mW/line (corresponding to 0.5 mW per pixel) and integration time of 200 ms/line were used. The excitation wavelengths for a particular FP were chosen to be similar (or equal) to those previously used in FRET [9, 10, 66, 112] or other fluorescence-based studies [101, 126, 127], and which, in certain cases, have caused the FP to elicit some peculiar behavior, e.g. photo-switching. Immediately before and after each series of micro-spectroscopic measurements were performed, an excitation spectrum of the sample was acquired, in order to study the effect of successive excitations on the spectral characteristics of the FPs. The excitation spectra were acquired by scanning the sample multiple times, each time

with a different wavelength, ranging from 780 nm to 1000 nm in increments of 20 nm. The average laser power and integration time were kept constant for each excitation throughout the course of an excitation spectrum acquisition, namely at 100 mW/line and 50 ms/line, respectively. From the 2p excitation time series, the extent of photobleaching for each FP was quantified by calculating the fraction of total fluorescence lost during first 10 the first excitation scans, as follows:

$$R_{2p}^{PB} = \frac{TF_1 - TF_{10}}{TF_1} \times 100, \tag{3.1}$$

where TF_1 and TF_{10} represent the total fluorescence (integrated over the entire emission spectrum) detected after the 1st and 10th scans, respectively, of the sample using an excitation wavelength ($\lambda_{exc,max}$) corresponding to the peak wavelength of the excitation spectrum of the particular FP under study.

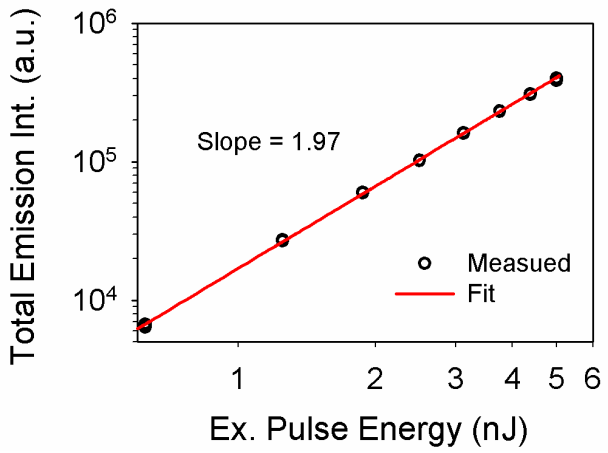

Figure 3.1. Log-log plot of the total fluorescence emission as a function of the pulse energy under two-photon excitation. The fluorescence sample is mEGFP-doped PAA gel at pH 8 with a final concentration of mEGFP of 1 µM. The measurements were taken with an excitation wavelength of 960 nm using different powers (per entire excitation line) ranging from 50 mW to 400 mW in increments of 50 mW, and a camera integration time of 50 ms. The slope of the fitted line is 1.97, nearly identical to the expected value of 2 expected for two-photon excitation.

To test for the expected quadratic dependence of the fluorescence emission vs. laser pulse energy for two-photon excitation, we used mEGFP prepared as described in Section 2.1. The sample was excited at 960 nm at several average excitation powers ranging from 50 mW per entire laser line to 400 mW/line in increments of 50 mW/line. To minimize the unwanted photobleaching we avoided taking multiple measurements from the same spot of the fluorescent sample. The resulting log-log plot (see Fig. 3.1) of total fluorescence emission as a function of the laser pulse energy exhibited a quadratic dependence, as expected.

3.2.5. Measurements of FP-doped PAA gel for two-photon relative brightness

To determine the 2p brightness (relative to mEGFP brightness) of all the FPs investigated, micro-spectroscopic measurements were performed on FP doped gel using a similar imaging system as described in Section 2.4 above, except that the OptiMiS^{TM} scanning/detection head was modified to employ a pseudo-line-scan protocol. In this protocol, the appearance of a line was generated by rapidly sweeping a point-focused laser beam along a line in the sample, while integrating the signal on the camera during the course of the sweep. The inverted microscope used in conjunction with the OptiMiS^{TM} scanning/detection head in this system was a Zeiss Axio Observer equipped with a water-immersion objective with 63× magnification and NA= 1.2.

In order to assure the FPs were uniformly distributed throughout the gel, z-stack acquisitions were performed, in which micro-spectroscopic measurements were taken at multiple planes within the FP-doped gel. Specifically, the initial measurement was taken at a plane within the gel located ~5 μm away from the coverslip-gel interface. Then, the microscope objective was moved by 2 μm in the z-direction such that the focus of the laser was moved

further into the gel, and micro-spectroscopic measurements were taken again. This process was repeated until the focus of the laser beam reached to ~5 μm away from the top gel-microscope slide interface. For all z-stack acquisitions, an average laser power of 12 mW/point and a dwell time of 195 μs/point were used. The excitation wavelengths were chosen to correspond to the peak of the FP's excitation spectra (e.g., an excitation wavelength of 960 nm was used for mEGFP and 800 nm for mGFP2).

3.2.6. Spectral unmixing and calculation of total emission intensity

Emission spectra of the FP-doped polyacrylamide (PAA) gel obtained using the micro-spectroscopic measurements described above contained contributions not only from the FPs embedded in the gel but other sources as well. For example, the polyacrylamide gel was also seen to be excited in the optical micro-spectroscope. In order to separate the FP signal from the other contributing sources of signal, a previously described spectral unmixing procedure was applied to the composite emission spectra [5] obtained from each gel sample. Briefly, a single composite emission spectrum was obtained from a micro-spectroscopic scan by averaging the intensity values over a 1000 pixels region for each wavelength channel obtained from the scan. Then the composite emission spectrum was deconvoluted into the FP and PAA components using a least-squares fitting algorithm [5, 7, 88] (implemented using Solver in Microsoft Excel^{TM}) along with separately determined elementary spectra of the FP and PAA gel. In order to determine the elementary spectra of the FP and the PAA gel, separate micro-spectroscopic measurements were performed on PAA gel alone (i.e., without FP embedded in it) and the FP in solution (i.e., not embedded in gel); each of the elementary spectra was normalized to their respective maximum intensities before being used in the unmixing algorithm.

The unmixing procedure provided two best-fit parameters, k^{FP} and k^{gel}, which are proportional to the emission intensity of the FP and PAA gel, respectively. In other words, k^{FP} and k^{gel} are the parameters multiplying each respective elementary spectrum comprising the theoretical function used to fit the measured composite emission spectrum. Once it was extracted using the unmixing procedure, the k^{FP} value was multiplied with the spectral integral of the FP (i.e., area underneath the elementary spectrum of the FP) to obtain the total emission intensity (also known as total fluorescence) of a given FP. Under certain experimental conditions – for example, in measurements using relatively low excitation powers or short exposure times (or both) –, there was no detectable contribution of the PAA gel to the emission spectra of the FP-doped PAA gel. In those situations, the FP signals were separated from the measured emission signal simply by subtracting the minimum intensity of the emission spectrum from the observed emission signals, which corresponds to the DC-bias and shot noise distribution of the camera. Then the total detected emission intensity was calculated by integrating the entire FP spectrum (after background subtraction).

3.3. Results

In order to quantify and compare the photophysical properties, i.e., the excitation and emission spectra, molecular brightness, level of photobleaching and photo-switching, and sensitivity to pH, of widely used FPs, we performed a series of two-photon (2p) micro-spectroscopic scans of FPs samples according to the procedure described in detail in Section 2.4 (and which we refer to as an excitation time series). The FPs samples were PAA gel doped with one of the following FPs: mGFP2 [52, 66], mEGFP [38, 43, 122], mYFP [26, 128], mCitrine [35], SYFP2

[55], mVenus [55], mTurquoise (mTq) [58], mCerulean3 [57], and mTFP1 [4]. These FPs were separately immobilized in PAA gel, as described in Section 2.3, to reduce their molecular diffusion [124] before and during the series of measurements.

The degree of 2p photobleaching of each FP was quantified using the relative two-photon photobleaching (R_{2p}^{PB}, see Eq. 3.1 above), which we defined as the fraction of total emission intensity lost after the first ten successive excitations using an excitation wavelength corresponding to the excitation maximum of each FP. The relative 2p photobleaching reported for a particular FP was determined by averaging the R_{2p}^{PB} over multiple sets of excitation scans performed on different samples containing the tested FP. It should be noted that for samples that exhibited strong photo-switching properties, we were not able to calculate a value for R_{2p}^{PB}, as the reduction of the total intensity during the repeated time series excitations was the result of the combined effect of photobleaching and photo-switching. All the properties investigated are first presented and discussed in detail in the following sub-sections and then summarized in Table 3.1.

3.3.1. Photostability of FPs investigated using 2p excitation time series

3.3.1.1. Green variants of GFP

Fig. 3.2 illustrates the results obtained from mGFP2-doped PAA gel samples subjected to an excitation time series consisting of ten successive excitation scans at 960 nm alternating (four times) with ten successive excitation scans at 800 nm. As seen in panel a, the total emission intensity decreased during the course of the ten successive excitation scans. The rate of decrease in the total emission intensity was higher for excitation at 800 nm in comparison to excitation at 960 nm. In addition, (*i*) the fluorescence intensities acquired upon excitation at 960 nm jumped significantly upwards when those measurements followed the excitation scans at 800 nm, (*ii*) while excitation at 960 nm had little to no effect on the results of subsequent 800 nm excitation series. This second observation suggests that, while the slight decrease in emission intensity within each set of ten 960 nm excitation scans was caused primarily by photobleaching, the marked decreasing trend in the intensities during each of the ten excitation scans at 800 nm was caused instead by photo-switching induced by excitation at 800 nm.

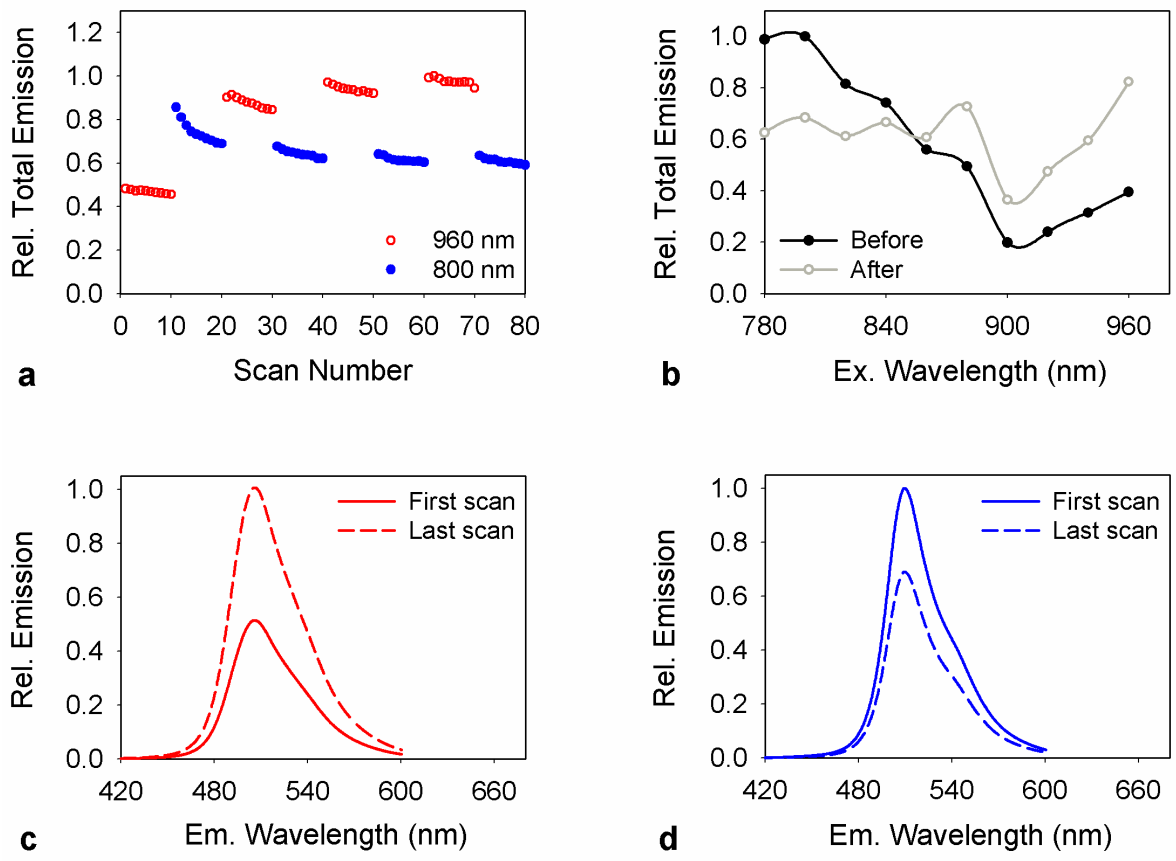

Figure 3.2. Response to repeated two-photon excitation scans of PAA gel doped with monomeric Green Fluorescent Protein 2 (mGFP2) at pH 8. **(a)** Changes in total emission intensity (integrated over all emission wavelengths) induced by acquiring time series of ten successive excitation scans at 960 nm (empty red circles), followed by ten successive excitation scans at 800 nm (filled blue circles). The couple of 960-nm/800-nm scans was repeated three additional times, for a total of forty excitation scans at each wavelength. The total emission was computed by integrating over the entire emission spectrum. **(b)** Comparison of two-photon excitation spectra, measured as emission intensity, before (—●—) and after (—○—) the sample was subjected to the entire excitation time series as shown in (a). **(c)** Emission spectra of mGFP2 observed at an excitation wavelength of 960 nm, where the red solid line represents the first and the red dashed line represents the last emission spectrum obtained from the repeated excitation time series. **(d)** Emission spectra of mGFP2 observed upon excitation at 800 nm, where the blue solid line represents the first and the blue dashed line represents the last emission spectrum obtained from the repeated time series excitations. All plots were normalized to the maximum value observed in the respective data set. The final concentration of mGFP2 in the FP-doped polyacrylamide gel was 1 μM. For repeated excitation time series, the integration time of the camera was 200 ms and the excitation power per entire excitation line was 200 mW (corresponding to an excitation energy of 100 μJ per pixel). For the excitation spectra measurements, the integration time was 50 ms and the excitation power was 100 mW/line (corresponding to an excitation energy of 12.5 μJ per pixel).

The above interpretation is also supported by the results shown in panels b, c and d of Figure 3.2, as follows. As seen by comparing the two mGFP2 excitation spectra of Fig. 3.2b (one obtained before and one after performing the excitation time series on the sample), a shift in the maximum two-photon excitation wavelength from 800 nm to 960 nm (or perhaps an even longer wavelength) occurred as a result of repeated excitation scans. Fig. 3.2c-d shows comparatively the changes in fluorescence intensities at excitation wavelengths of 960 nm (panel c) and 800 nm (panel d) at the beginning and the end of the entire excitation time series. Notice the unchanged maximum emission wavelength, which may imply that the new mGFP2 species resulting from photo-switching may in fact be different forms of the same fluorescent protein, as described below.

The cause for the photo-switching observed in the mGFP2 sample can be ascertained from previously made observations regarding wtGFP [25, 48, 129], as follows. The wtGFP chromophore exists in either a neutral (i.e., protonated) form, which has a single-photon (1p) excitation maximum at 397 nm, or an anionic form that is maximally excited at 475 nm. Upon either single photon excitation (at 397 nm) or two-photon excitation (at about 800 nm), the neutral chromophores can undergo photoisomerization and be converted to their anionic form. The equilibrium between the neutral and anionic states is regulated by a complex hydrogen-bond network which forms between the amino acids of the fluorophore and surrounding water molecules. The breaking and forming of multiple hydrogen bonds facilitates a proton transfer from the side chains of the fluorophore to the chromophore, resulting in the stabilization of the chromophore in the anionic state [48].

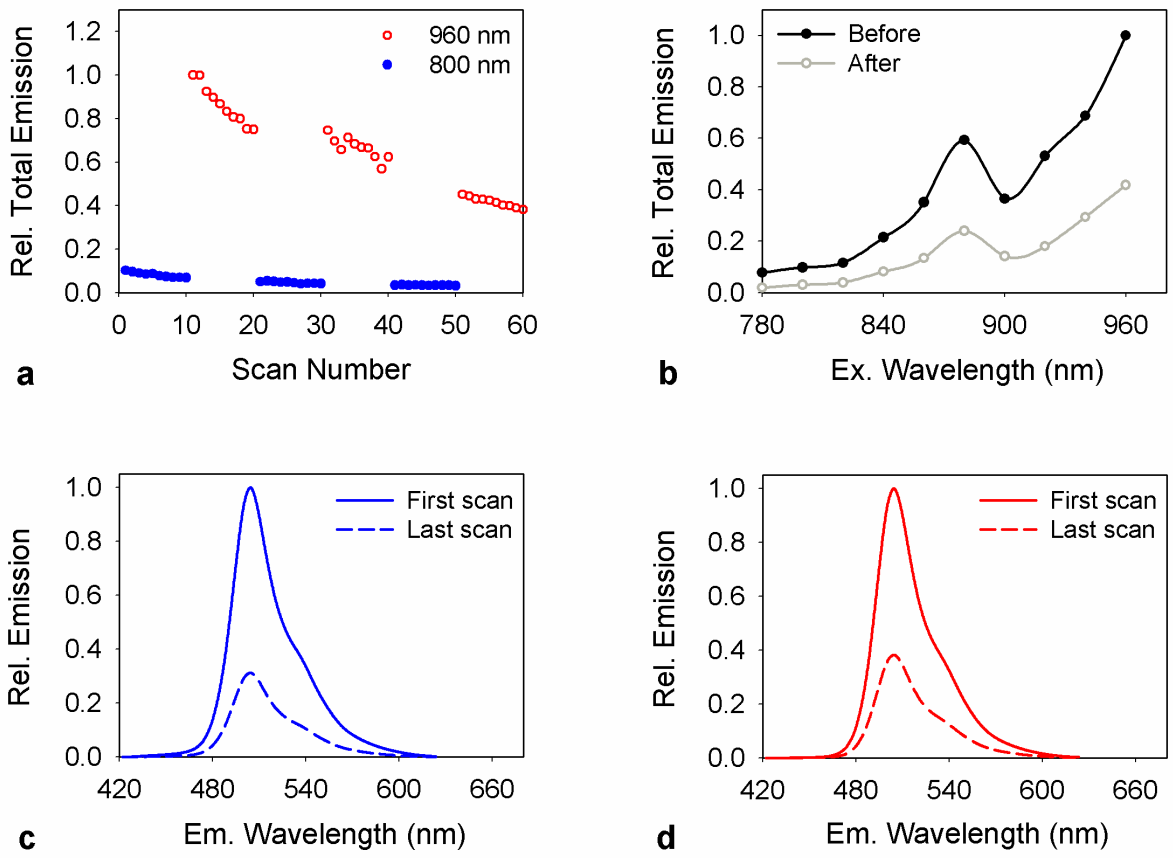

Figure 3.3. Response to repeated two-photon excitation scans of PAA gel doped with monomeric Enhanced Green Fluorescent Protein (mEGFP) at pH 8. (a) Changes in total emission intensity (integrated over the entire emission spectrum) induced by acquiring time series of ten successive excitation scans at 800 nm (solid blue circles), followed by ten successive excitation scans at 960 nm (empty red circles). The pair of 800-nm/960-nm scans was repeated two additional times, for a total of thirty excitation scans at each wavelength. The total emission intensity was computed by integrating over the entire emission spectrum. **(b)** Comparison of excitation spectra for before (—●—) and after (—○—) the entire excitation time series as shown in (a). **(c)** Emission spectra observed upon excitation at 800 nm, where the blue solid line represents the first and the blue dashed line represents the last emission spectrum obtained from the repeated time series excitations. **(d)** Emission spectra observed at an excitation wavelength of 960 nm, where the red solid line represents the first and the red dashed line represents the last emission spectrum obtained from the repeated excitation time series. All plots were normalized relatively to the maximum value observed in the respective data set. The final concentration of mEGFP in the FP-doped polyacrylamide gel was 1 µM. For repeated excitation time series, the integration time of the camera was 200 ms and the excitation power per entire excitation line was 200 mW (corresponding to an excitation energy of 100 µJ per pixel). For the excitation spectra measurements, the integration time was 50 ms and the excitation power was 100 mW/line (corresponding to an excitation energy of 12.5 µJ per pixel).

By replacing the serine amino acid at position 65 in the wtGFP sequence with threonine [130] (i.e., the S65T mutation, possessed by, e.g., the EGFP variant), the population of neutral (protonated) chromophores, and thereby the excitation peak at 397 nm, is effectively suppressed; this peak suppression occurs due to a rearrangement of hydrogen bond patterns in the nearby amino acid Glu222, which in turn suppresses the negative charge on Glu222 and allows the chromophore to assume an anionic form. We confirmed the decrease of the neutral population of chromophores due to the S65T mutation by observing the effect of applying the excitation time series to EGFP-doped PAA gel (see Fig. 3.3). It is apparent from the results shown in (see Fig. 3.3) that no photo-switching is observed during excitation time series measurements of EGFP-doped PAA gel, due to the fact that all chromophores are presumably already in the anionic form prior to being exposed to any 800 nm excitation scan. However, mGFP2, which does not have the S65T mutation and therefore maintains a population of chromophores in the neutral form (and maintains an excitation peak at 397 nm in 1p excitation and 800 nm in 2p excitation), is susceptible to ionization when excited using 2p excitation at 800 nm. This ionization causes the significant amount of photo-switching seen in Fig. 3.2a and the shift in excitation spectrum seen in Fig. 3.2b.

These results suggest that mGFP2 could be used in experiments where photo-switching is useful or necessary. Nevertheless, it needs to be used with caution in other studies where such effects might introduce challenges, such as in FRET experiments that rely on two different excitation wavelengths to determine both FRET efficiency and concentrations of donors and acceptors [10, 66, 80, 95]. To further explore the latter case, we performed experiments (illustrated in Fig. 3.4) in which the order of the wavelengths used in the excitation time series was switched. While a reduction in intensity is still seen during the repeated excitation scans,

exciting first at 800 nm appears to have photo-switched some of the fluorescent proteins to the subspecies (i.e., from protonated state to deprotonated state) the one that is excited more efficiently at 960 nm prior to the first excitation scan at 960 nm being measured. Therefore, scanning the sample using this order of excitation wavelengths (i.e., 800 nm first, and 960 nm second) may lead to a false impression that mGFP2 emits more upon excitation at 960 nm than compared to excitation at 800 nm. However, if we compare Fig. 3.4c and Fig. 3.2c, we conclude that the emission intensity at an excitation of 960 nm was actually less than that observed after the successive excitations at 800 nm. Hence, in general, for long-term measurements with multiple-wavelengths excitations, it is always better to start the measurement with the excitation wavelength that produces minimal unwanted photophysical effects (in this case, to avoid significant effects in the subsequent measurements).

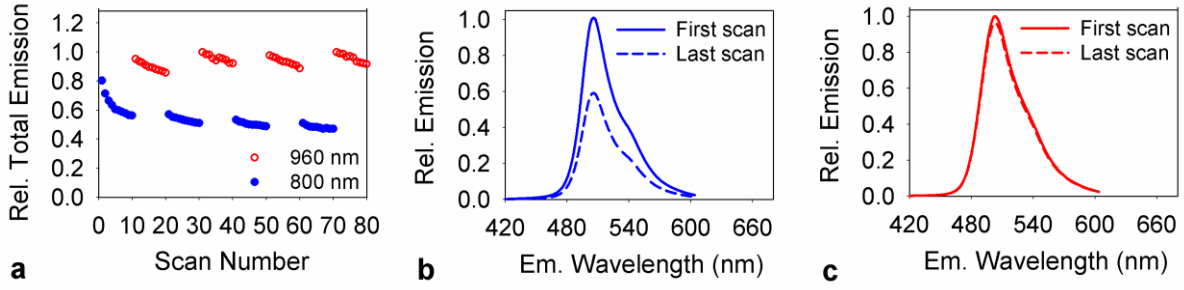

Figure 3.4. Changes in photophysical behavior of mGFP2 caused by switching the order between the two excitation wavelengths. (a) Changes in total emission intensity (integrated over the entire emission spectrum) induced by acquiring time series of ten successive excitation scans at 800 nm (filled blue circles), followed by ten successive excitations scans at 960 nm (empty red circles). The couple of 800-nm/960-nm scans was repeated three additional times, for a total of forty excitation scans at each wavelength. The total emission was computed by integrating over the entire emission spectrum. **(b)** Emission spectra of mGFP2 observed upon excitation at 800 nm, where the blue solid line was the first and the blue dashed line was the last emission spectrum obtained from the repeated time series excitations. **(c)** Emission spectra of mGFP2 observed at an excitation wavelength of 960 nm, where the red solid line represents the first and the red dashed line represents the last emission spectrum obtained from the repeated excitation time series. All resulting plots were normalized relatively to the maximum fluorescence observed in the respective data set. The final concentration of mGFP2 in the FP-doped polyacrylamide gel was 1 µM and pH value of the sample was 8. Performed using same excitation power and integration time as in Fig. 3.3.

3.3.1.2. Cyan fluorescent proteins

Unsurprisingly, not all GFP variants exhibited the same photophysical behavior. For example, a cyan variant of GFP known as monomeric Turquoise (mTq) (see Fig. 3.5), when exposed to alternating time series of excitation scans using a pair of wavelengths (920 nm and 880 nm) that correspond to the peaks in its two-photon excitation spectrum (Fig. 3.5b), underwent marked photobleaching, but no noticeable photo-switching, i.e., there was no increase in fluorescence signal under 920 nm excitation that followed 880 nm excitation scans (Fig. 3.5a), and no shift of excitation maxima (Fig. 3.5b). Similar results were obtained when switching the order of the excitation wavelengths in the excitation time series (see Fig. 3.6). The photobleaching of mTq was so pronounced – as seen from an overall signal decrease by approximately 65 % after the first ten repeated scans at 880 nm (Fig. 3.5)– that it makes it an unlikely choice for fluorescent tagging in single-molecule studies. This observation also invites caution when using mTq in any FRET studies where one expects the molecules to be immobile during their excitation (vs. molecules freely diffusing in solution), as photobleaching more significantly affects molecules that spend longer time within the excitation volume. Nevertheless, in-cell studies of fluorescence recovery after photobleaching could benefit from the propensity of mTq to photobleach.

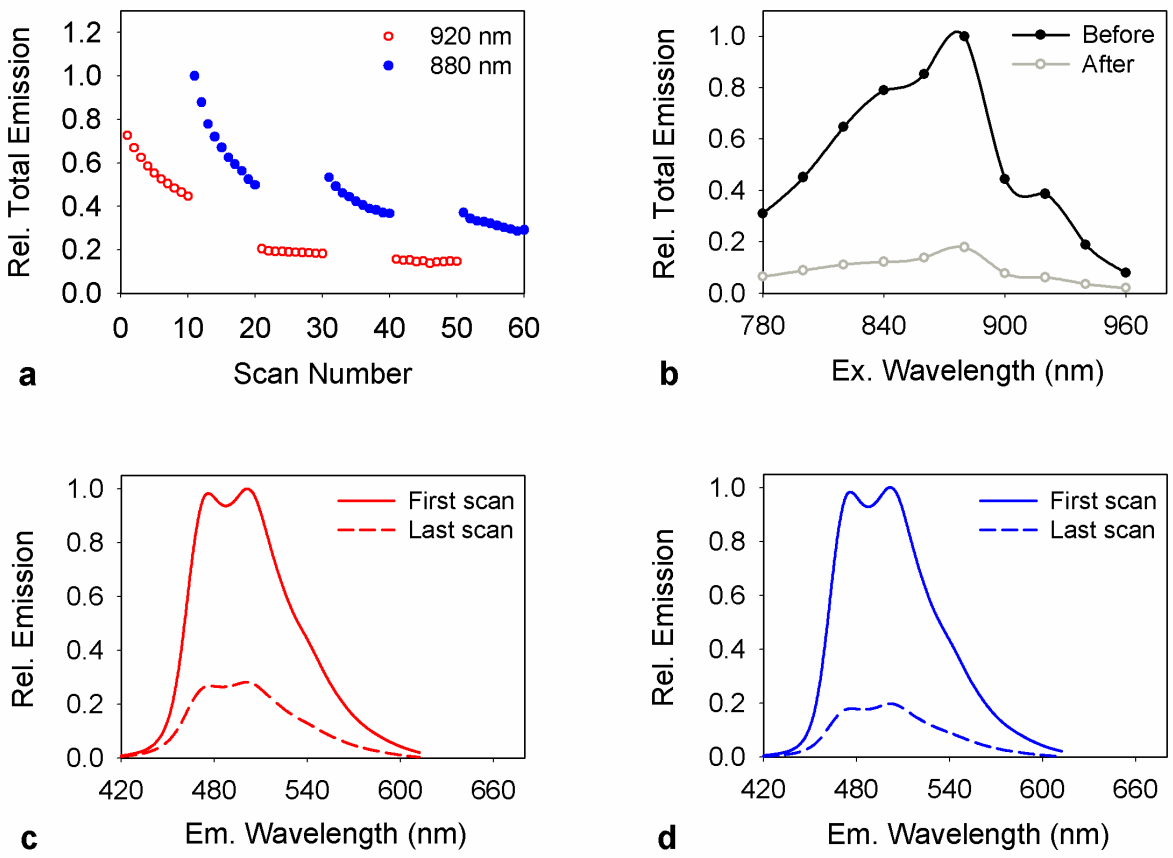

Figure 3.5. Response to repeated two-photon excitation scans of PAA gel doped with monomeric Turquoise (mTq) fluorescent proteins at pH 8. (a) Changes in total emission intensity induced by acquiring time series of ten successive excitations at 920 nm (empty red circles), followed by ten successive scans at 880 nm (filled blue circles). The couple of 920-nm/880-nm scans was repeated two additional times, for a total of thirty excitation scans at each wavelength. The total emission was computed by integrating over the entire emission spectrum. (b) Comparison of two-photon excitation spectra, measured as emission intensity, before (—●—) and after (—○—) the sample was subjected to the entire excitation time series as shown in (a). (c) Emission spectra of mTq observed at an excitation wavelength of 920 nm, where the red solid line represents the first and the red dashed line represents the last emission spectrum obtained from the repeated excitation time series. (d) Emission spectra of mTq observed upon excitation at 880 nm, where the blue solid line represents the first and the blue dashed line represents the last emission spectrum obtained from the repeated excitation time series. All plots in the figure were normalized relatively to the maximum value observed in the respective data set. The final concentration of mTq in the FP-doped polyacrylamide gel was 1 μM. For repeated excitation time series, the integration time of the camera was 200 ms and the excitation power per entire excitation line was 200 mW (energy, 100 μJ per pixel). For the excitation spectra measurements, the integration time was 50 ms and the excitation power was 100 mW/line (energy, 12.5 μJ per pixel).

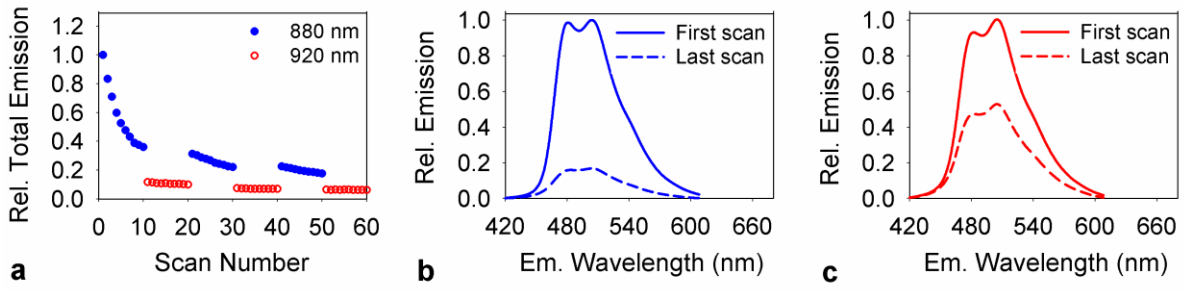

Figure 3.6. Changes in photophysical behavior of mTq caused by switching the order between the two excitation wavelengths at pH 8. (a) Changes in total emission intensity induced by acquiring time series of ten successive excitation scans at 880 nm (filled blue circles), followed by ten successive excitations scans at 920 nm (empty red circles). The pair of 880-nm/920-nm scans was repeated two additional times, for a total of thirty excitation scans at each wavelength. The total emission intensity was computed by integrating over the entire emission spectrum. **(b)** Emission spectra of mTq observed upon excitation at 880 nm, where the blue solid line was the first and the blue dashed line was the last emission spectrum obtained from the repeated time series excitations. **(c)** Emission spectra of mTq observed at an excitation wavelength of 920 nm, where the red solid line represents the first and the red dashed line represents the last emission spectrum obtained from the repeated excitation time series. All resulting plots were normalized relatively to the maximum fluorescence observed in the respective data set. The final concentration of mTq in the FP-doped polyacrylamide gel was 1 μM. For repeated excitation time series, the integration time of the camera was 200 ms and the excitation power per entire excitation line was 200 mW (energy,100 μJ per pixel).

Due to the significant amount of photobleaching observed for mTq, we investigated other FPs from the cyan family in order to gauge whether this is a property seen across this entire subfamily of wtGFP variants. Excitation time series performed on the fluorescent protein mCerulean3 (see Fig. 3.7), using the pair of excitation wavelengths 920 nm and 886 nm also demonstrations that a significant amount of photobleaching occurs after repeated scans; specifically, the total fluorescence intensity of mCerulean3 is reduced by more than 61 % after ten repeated scans at 886 nm (see Table 3.1). In addition, mCerulean3, like mTq, did not show any propensity to photo-switch under 2p excitation at either excitation wavelength.

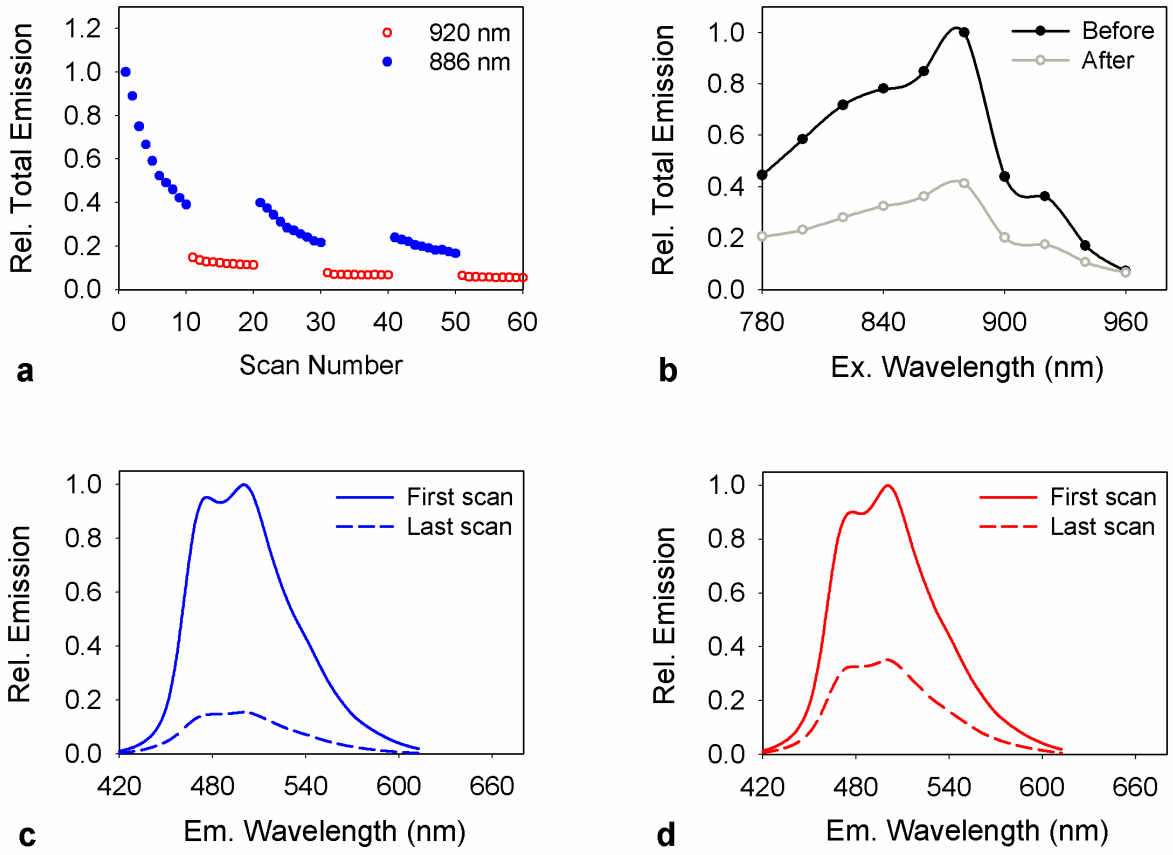

Figure 3.7. Response to repeated two-photon excitation scans of PAA gel doped with monomeric Cerulean3 (mCerulean3) Fluorescent at pH 8. (a) Changes in total emission intensity induced by acquiring time series of ten successive excitation scans at 886 nm (solid blue circles), followed by ten successive excitation scans at 920 nm (empty red circles). The pair of 886-nm/920-nm scans was repeated two additional times, for a total of thirty excitation scans at each wavelength. The total emission intensity was computed by integrating over the entire emission spectrum. **(b)** Comparison of excitation spectra for before (black line with filled circles) and after (gray line with empty circles) the entire excitation time series as shown in (a). **(c)** Emission spectra observed upon excitation at 886 nm, where the blue solid line represents the first and the blue dashed line represents the last emission spectrum obtained from the repeated time series excitations. **(d)** Emission spectra observed at an excitation wavelength of 920 nm, where the red solid line represents the first and the red dashed line represents the last emission spectrum obtained from the repeated excitation time series. All plots were normalized relatively to the maximum value observed in the respective data set. The final concentration of mCerulean3 in the FP-doped polyacrylamide gel was 1 μM. For repeated excitation time series, the integration time of the camera was 200 ms and the excitation power per entire excitation line was 200 mW (energy, 100 μJ per pixel). For the excitation spectra measurements, the integration time was 50 ms and the excitation power was 100 mW/line (energy, 12.5 μJ per pixel).

The photobleaching propensity of both mCerulean3 and mTq is potentially a result of the manner in which these FPs (and all of the cyan derivatives of wtGFP for that matter) have been engineered, i.e., by altering the covalent structure of the chromophore through the substitution of amino acids for Tyrosine at amino acid position 66.

In contrast to the wtGFP-derived cyan FPs, which have been engineered via the Y66W substitution in the wtGFP chromophore, there are a number of naturally occurring cyan FPs found in various coral species which possess an anionic tyrosine-derived chromophore that is chemically identical to that of enhanced wtGFP [131]. The challenge posed by many of these naturally occurring cyan FPs found in coral species is that they have a propensity to form strong dimers or even tetramers. Fortunately, optimization of a tetrameric cyan FP found in Clavularia coral (i.e., sp. CFP484 [4]) has led to a monomeric form of the FP, namely monomeric teal fluorescent protein (mTFP1), which is potentially a favorable alternative to wtGFP-derived CFPs with tryptophan-derived chromophores such as enhanced CFP or Cerulean [4, 131].

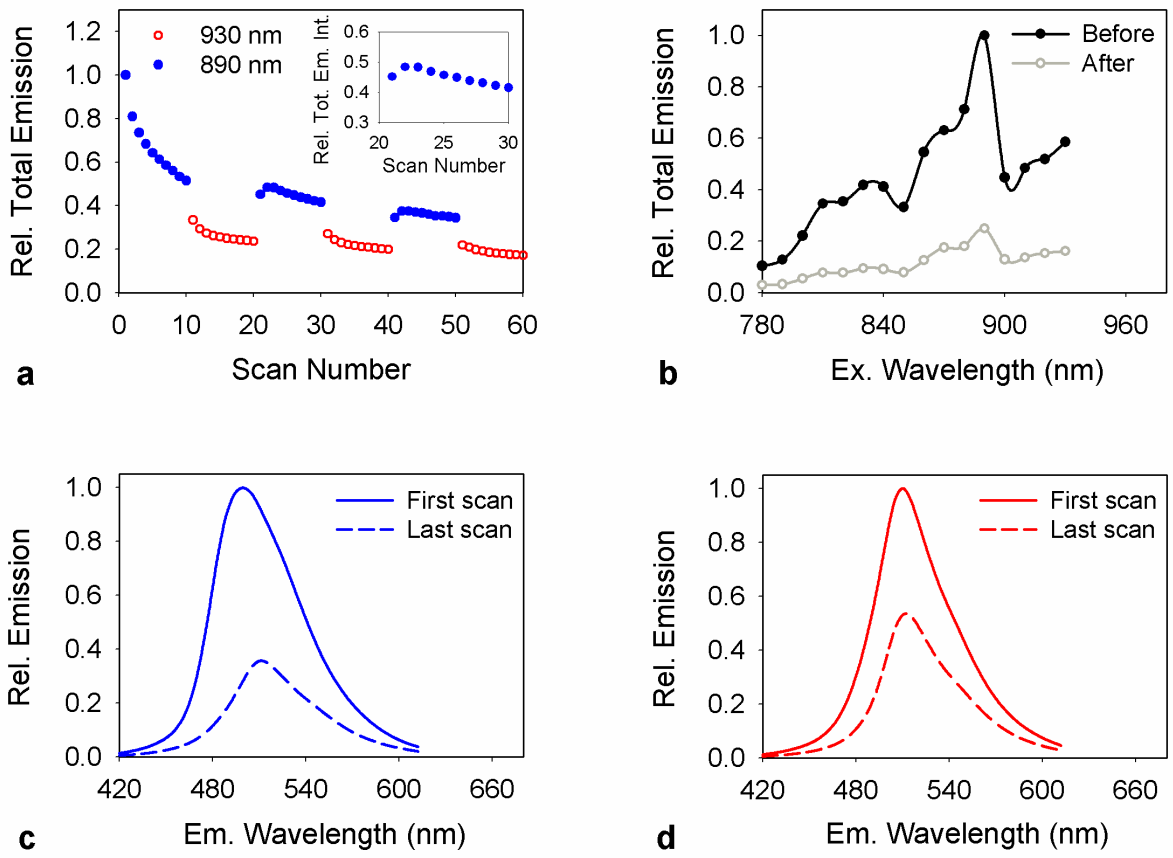

Figure 3.8. Response to repeated two-photon excitation scans of PAA gel doped with monomeric TFP1 Fluorescent Protein at pH 8. (a) Changes in total emission intensity induced by acquiring time series of ten successive excitation scans at 890 nm (filled blue circles), followed by ten successive excitation scans at 930 nm (empty red circles). The couple of 890-nm/930-nm scans was repeated two additional times, for a total of thirty excitation scans at each wavelength. The total emission was computed by integrating over the entire emission spectrum. The inset displays only the results obtained between scans 10 and scan 40 and serves the purpose of highlighting the increase in emission signal at 930 nm scan due to excitation time series at 890 nm, which most likely occurs due to photo-switching. **(b)** Comparison of two-photon excitation spectra, measured as emission intensity, before (—●—) and after (—○—) the sample was subjected to the entire excitation time series as shown in (a). **(c)** Emission spectra observed upon excitation at 890 nm, where the blue solid line represents the first and the blue dashed line represents the last emission spectrum obtained from the repeated time series excitations. **(d)** Emission spectra observed at an excitation wavelength of 930 nm, where the red solid line represents the first and the red dashed line represents the last emission spectrum obtained from repeated excitation time series. All plots were normalized relatively to the maximum value observed in the respective data set. The FP-doped polyacrylamide gel sample was prepared and measured as described in Fig. 3.2

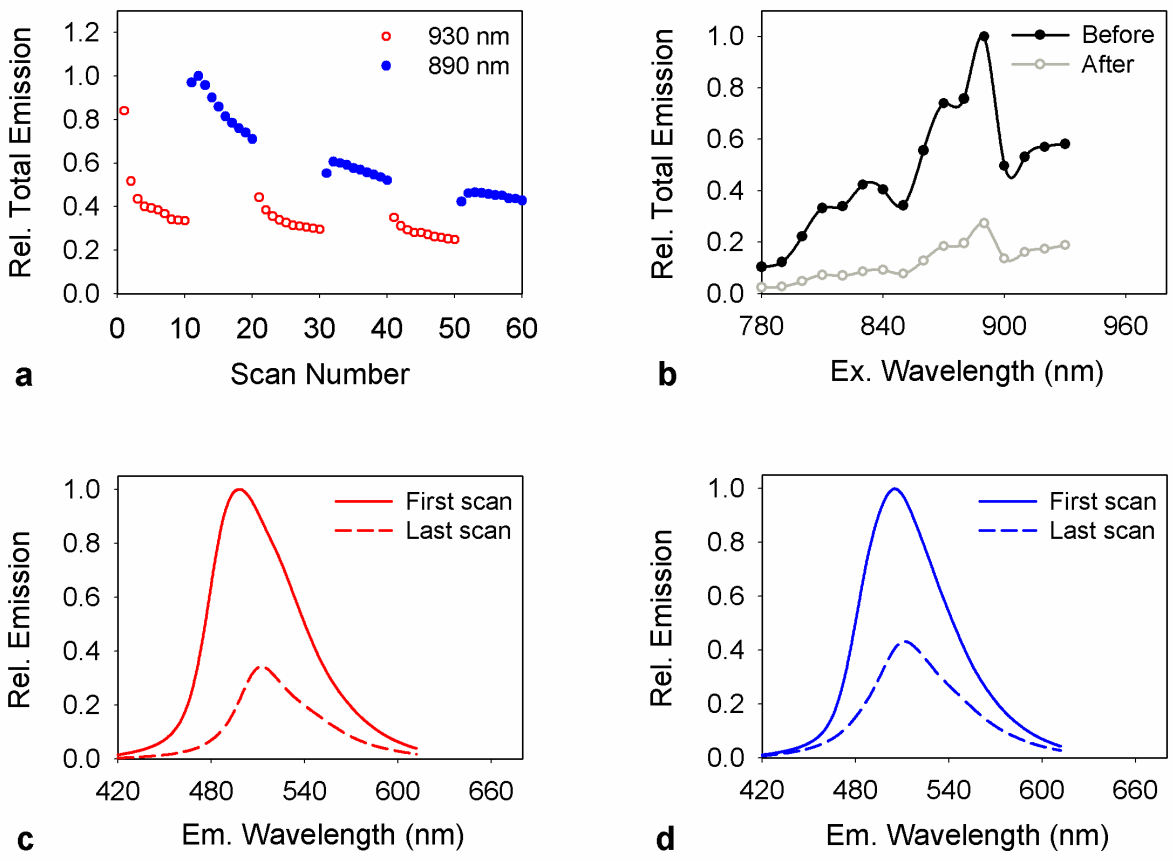

Figure 3.9. Response to repeated two-photon excitation scans of PAA gel doped with monomeric mTFP1 at pH 8. (a) Changes in total emission intensity induced by acquiring time series of ten successive excitations at 930 nm (empty red circles), followed by ten successive scans at 890 nm (filled blue circles). The pair of 930-nm/890-nm scans was repeated two additional times, for a total of thirty excitation scans at each wavelength. The total emission intensity was computed by integrating over the entire emission spectrum. **(b)** Comparison of excitation spectra before (black line with filled circles) and after (gray line with empty circles) the entire excitation time series as shown in (a). **(c)** Emission spectra of mTFP1 observed at an excitation wavelength of 930 nm, where the red solid line represents the first and the red dashed line represents the last emission spectrum obtained from the repeated excitation time series. **(d)** Emission spectra of mTFP1 observed upon excitation at 890 nm, where the blue solid line represents the first and the blue dashed line represents the last emission spectrum obtained from the repeated excitation time series. All plots in the figure were normalized relatively to the maximum value observed in the respective data set. The final concentration of mTFP1 in the FP-doped polyacrylamide gel was 1 μM. For repeated excitation time series, the integration time of the camera was 200 ms and the excitation power per entire excitation line was 200 mW (energy, 100 μJ per pixel). For the excitation spectra measurements, the integration time was 50 ms and the excitation power was 100 mW/line (energy, 12.5 μJ per pixel).

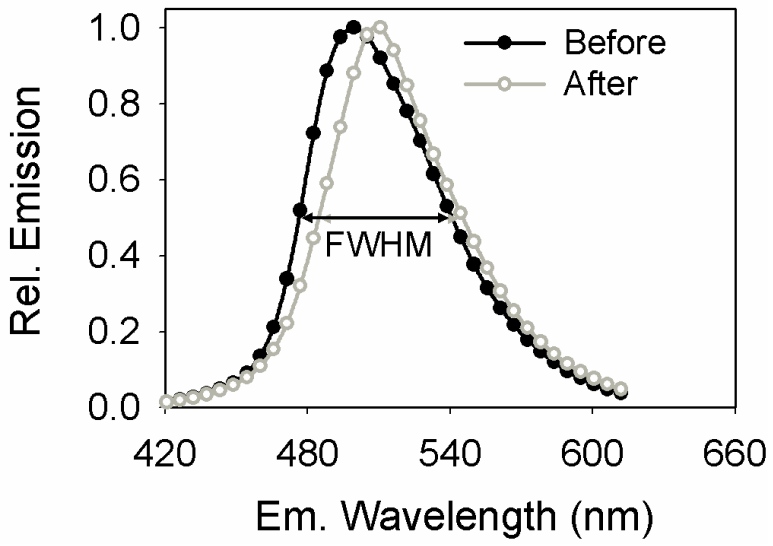

Figure 3.10. Shift in emission spectrum (normalized to its maximum value) in repeated two-photon excitation scans of PAA gel doped with monomeric mTFP1 at pH 8. Changes in total emission spectrum followed by eight successive scans at 890 nm, where —●— represents the emission spectrum before the successive scans and the —○— represents emission spectrum after the successive scans. The plots in the figure were normalized separately with respect to their maximum emission intensity. The full width half maximum of the emission spectrum before the and after the successive scans are ~ 63 nm and ~ 60 nm, respectively; the emission peaks shifted from 499 nm to 509 nm. The final concentration of mTFP1 in the FP-doped polyacrylamide gel was 1 μM.

Interestingly, a minute but noticeable, reversible photo-switching effect is also observed for mTFP1 (Fig. 3.8 and Fig. 3.9). A slight increase in fluorescence signal obtained from 930 nm excitation scans was observed after each set of 890 nm excitation scans was performed (see Fig. 3.8a). The effect of photo-switching on mGFP2, presented above, manifested itself as a change in the mGFP2 excitation spectrum (Fig. 3.2b) with no noticeable change in the emission spectrum. However, in the case of mTFP1, the reverse occurred. While no discernible change to the excitation spectrum was detected for mTFP1 (Fig. 3.8b), the emission spectrum of mTFP1 was altered as a result of repeated excitation scans at 890 nm, in that it became both narrower and red-shifted (see Fig. 3.9). Similar results were obtained after switching the order

of the excitation wavelengths in the excitation time series (see Fig. 3.10 and in ref. [14]) . A more detailed biochemical study of the crystal structures of mTFP1 is needed in order to determine the exact mechanism which causes this slightly altered photophysical behavior when compared with the cyan variants of wtGFP.

Under two-photon excitation, mTFP1 presents slightly different photophysical properties when compared to mCerulean3 and mTq. The results obtained from performing an excitation time series (using the pair of excitation wavelengths 930 nm and 880 nm) on mTFP1-doped PAA gel are shown in Fig. 3.10 As seen, mTFP1 is still appreciably photobleached after repeated scans; however, the extent of the photobleaching is noticeably less (total fluorescence intensity was reduced by 47%) compared to the reduction in fluorescence intensity of mTq (65%) and mCerulean3 (61%). Furthermore, mTFP1 was found to be significantly brighter than mTq and mCerulean3, with the relative 2p brightness (relative to mEGFP; see Table 3.1) of mTFP1 (1.56) nearly two times higher than mTq (0.85) and ~2.5 times higher than mCerulean3. Therefore, it appears that mTFP1 is a favorable alternative to some of the *Aequorea victoria* FPs in the cyan family.

3.3.1.3. Yellow variants of GFP

The final subset of GFP variants we investigated were those belonging to the yellow fluorescent protein subfamily. The photophysical properties of the monomeric yellow fluorescent protein (mYFP) were probed by exposing mYFP embedded PAA gel to an excitation time series using the pair of excitation wavelengths 960 nm and 800 nm (see Fig. 3.11). A very modest reduction in the fluorescence signal (~9 %) was observed after repeated excitations using the peak excitation wavelength (960 nm) of mYFP. Furthermore, the mYFP excitation spectrum before and after the repeated time series excitation (see Fig. 3.11) were nearly identical, both in overall shape and intensity values. These results indicate that mYFP neither photo-switches nor photobleaches significantly under 2p excitation. These results were identical, i.e., the extent of photobleaching and photo-switching, when switching the order of the excitation wavelengths in the excitation time series (see Fig. 3.12). Similar results were obtained for other yellow variants of the wtGFP, i.e., mVenus, mCitrine, and SYFP2 in that very little photobleaching was observed after subjecting the samples to excitation time series (Figures 3.13 to 3.15). Within the yellow protein subfamily, the maximum amount of photobleaching (~17%) was observed for SYFP2 after repeated excitation scans at 960 nm; this is still appreciably less than the amount of signal lost due to photobleaching for any of the cyan FPs tested or even for EGFP (see Table 3.1. for comparison). Furthermore, there was no photo-switching observed for any of the yellow FPs.

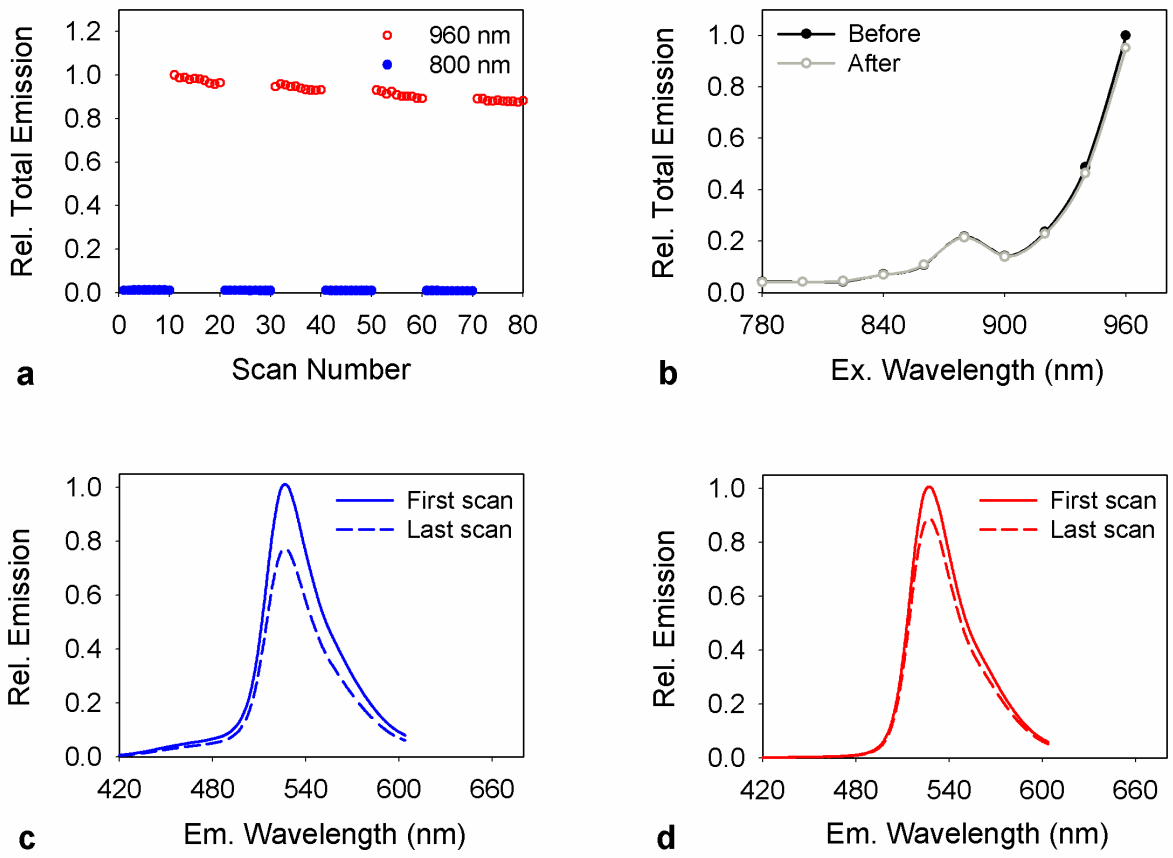

Figure 3.11. Response to repeated two-photon excitation scans of PAA gel doped with monomeric Yellow Fluorescent Protein (mYFP) at pH 8. (a) Changes in total emission intensity induced by acquiring time series of ten successive excitation scans at 800 nm (filled blue circles), followed by ten successive excitation scans at 960 nm (empty red circles). The pair of 800-nm/960-nm scans was repeated three additional times, for a total of forty excitation scans at each wavelength. The total emission intensity was computed by integrating over the entire emission spectrum. **(b)** Comparison of excitation spectra for before (—●—) and after (—○—) the entire excitation time series as shown in (a). **(c)** Emission spectra of mYFP observed upon excitation at 800 nm, where the blue solid line represents the first and the blue dashed line represents the last emission spectrum obtained from the repeated time series excitations. **(d)** Emission spectra of mYFP observed at an excitation wavelength of 960 nm, where the red solid line represents the first and the red dashed line represents the last emission spectrum obtained from the repeated excitation time series. All plots were normalized relatively to the maximum value observed in the respective data set. The final concentration of mYFP in the FP-doped polyacrylamide gel was 1 μM. For repeated excitation time series, the integration time of the camera was 200 ms and the excitation power per entire excitation line was 200 mW (energy, 100 μJ per pixel). For the excitation spectra measurements, the integration time was 50 ms and the excitation power was 100 mW/line (energy, 12.5 μJ per pixel).

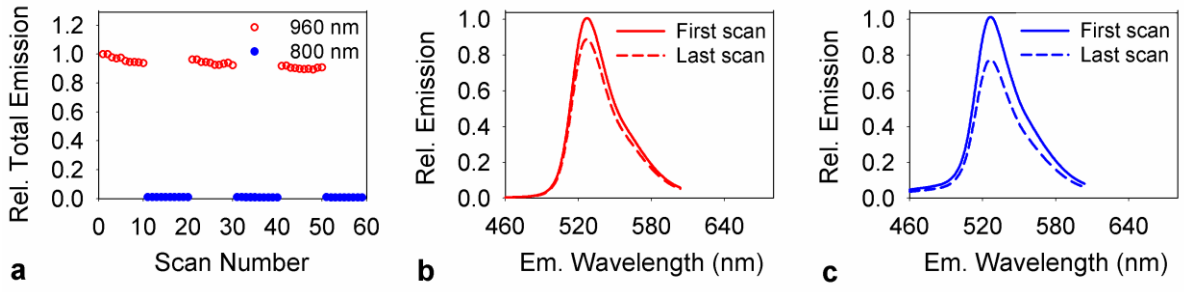

Figure 3.12. Changes in photophysical behavior of mYFP caused by switching the order between the two excitation wavelengths. (a) Changes in total emission intensity induced by acquiring time series of ten successive excitation scans at 960 nm (empty red circles), followed by ten successive excitations scans at 800 nm (filled blue circles). The pair of 960-nm/800-nm scans was repeated two additional times, for a total of thirty excitation scans at each wavelength. The total emission intensity was computed by integrating over the entire emission spectrum. **(b)** Emission spectra of mYFP observed at an excitation wavelength of 960 nm, where the red solid line represents the first and the red dashed line represents the last emission spectrum obtained from the repeated excitation time series. **(c)** Emission spectra of mYFP observed upon excitation at 800 nm, where the blue solid line was the first and the blue dashed line was the last emission spectrum obtained from the repeated time series excitations. All resulting plots were normalized relatively to the maximum fluorescence observed in the respective data set. The final concentration of mYFP in the FP-doped polyacrylamide gel was 1 μM. For repeated excitation time series, the integration time of the camera was 200 ms and the excitation power per entire excitation line was 200 mW (energy, 100 μJ per pixel).

The photo-stable behaviors of the yellow FPs (mYFP, mVenus, mCitrine and SYFP2) we have found using 2p excitation stand in direct contrast to findings of previous studies [38, 132], which have shown that the yellow variants are generally less photostable than mEGFP and the cyan variants when excited using 1p wide-field illumination. Therefore, this photostable behavior of the yellow FPs make them a strong candidate for fluorescent tagging in single-molecule studies as well as in FRET studies which utilize 2p excitation. However, it should be noted, that a major drawback to the palette of FPs in the yellow subfamily of wtGFP variants is that they typically have larger pKa values, especially mYFP (pKa value of 6.9), which make them more susceptible to pH variations in the sample when compared to other subfamilies of wtGFP, and this drawback exists regardless of the choice of excitation.

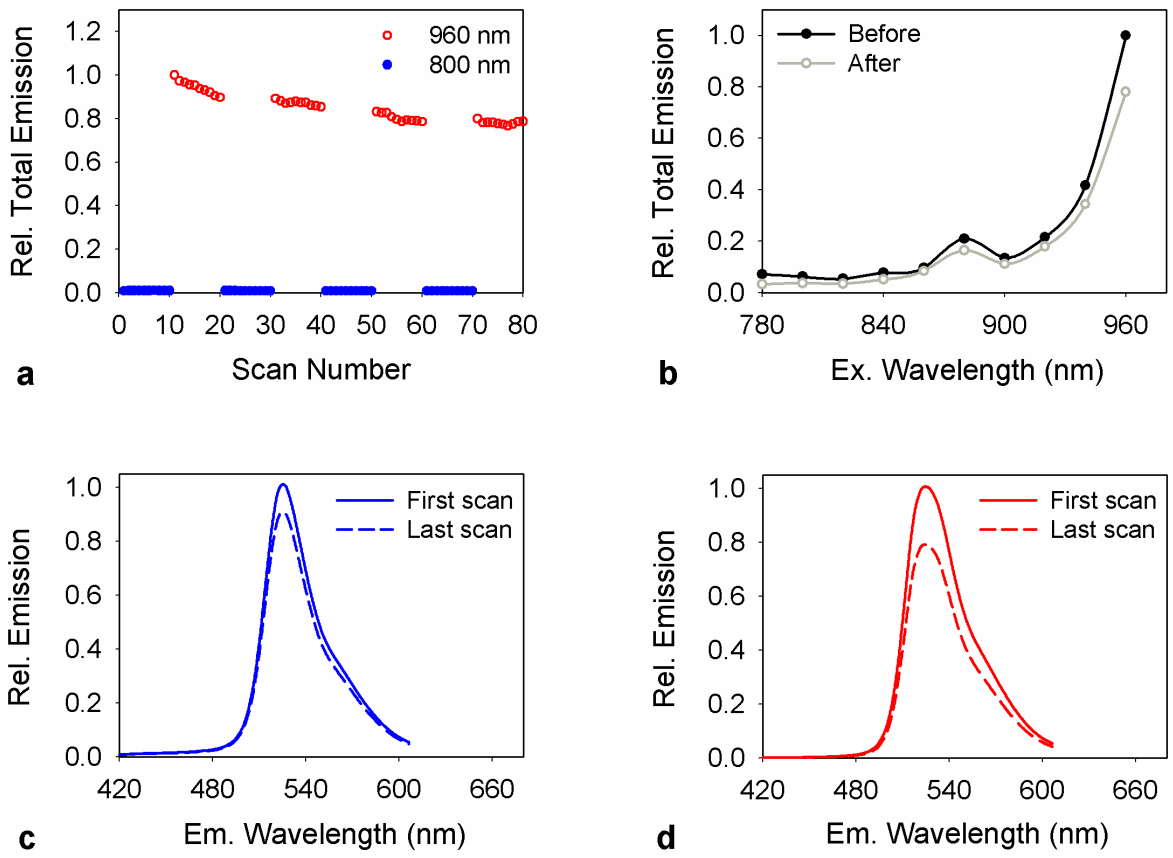

Figure 3.13. Response to repeated two-photon excitation scans of PAA gel doped with monomeric Fluorescent Protein Venus (mVenus) at pH 8. (a) Changes in total emission intensity induced by acquiring time series of ten successive excitation scans at 800 nm (filled blue circles), followed by ten successive excitation scans at 960 nm (empty red circles). The pair of 800-nm/960-nm scans was repeated three additional times, for a total of forty excitation scans at each wavelength. The total emission intensity was computed by integrating over the entire emission spectrum. **(b)** Comparison of excitation spectra for before (black line with filled circles) and after (gray line with empty circles) the entire excitation time series as shown in (a). **(c)** Emission spectra observed upon excitation at 800 nm, where the blue solid line represents the first and the blue dashed line represents the last emission spectrum obtained from the repeated time series excitations. **(d)** Emission spectra observed at an excitation wavelength of 960 nm, where the red solid line represents the first and the red dashed line represents the last emission spectrum obtained from the repeated excitation time series. All plots were normalized relatively to the maximum value observed in the respective data set. The final concentration of mVenus in the FP-doped polyacrylamide gel was 1 μM. For repeated excitation time series, the integration time of the camera was 200 ms and the excitation power per entire excitation line was 200 mW (energy, 100 μJ per pixel). For the excitation spectra measurements, the integration time was 50 ms and the excitation power was 100 mW/line (energy, 12.5 μJ per pixel).

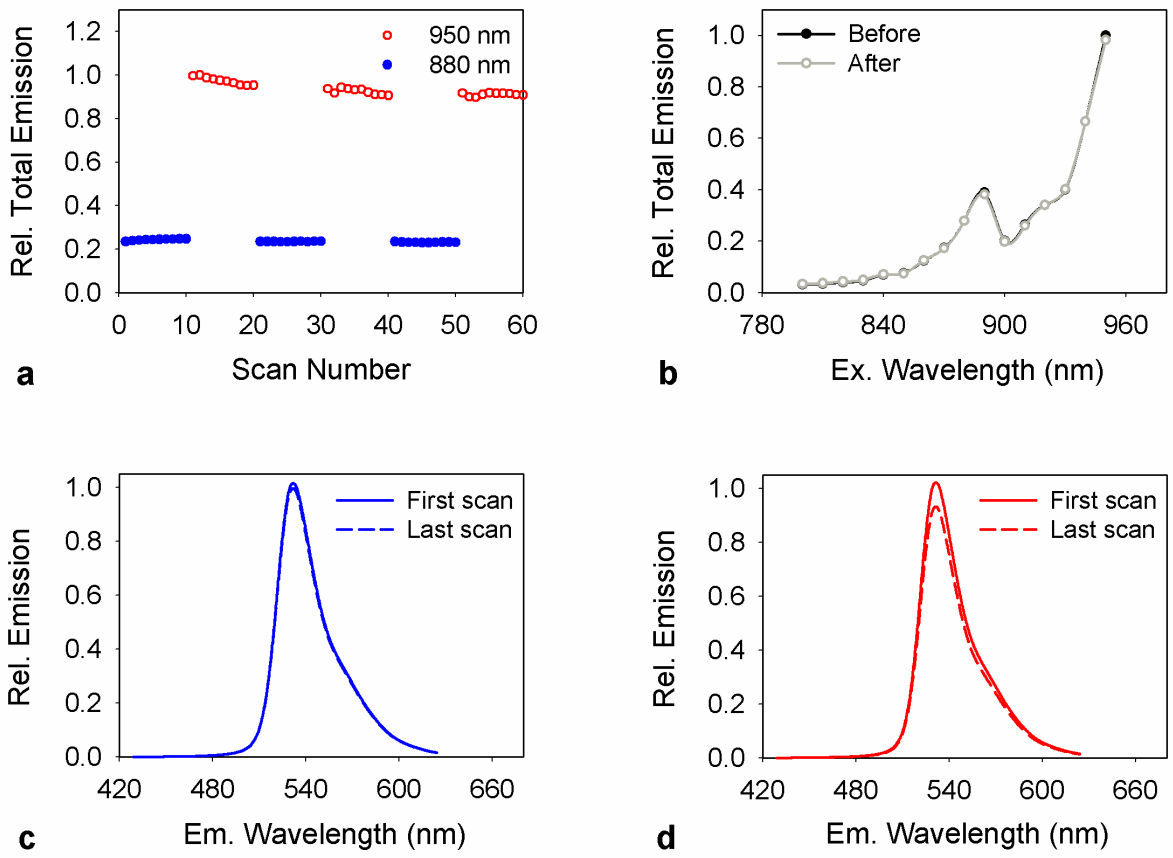

Figure 3.14. Response to repeated two-photon excitation scans of PAA gel doped with monomeric Fluorescent Protein Citrine (mCitrine). (a) Changes in total emission intensity induced by acquiring time series of ten successive excitation scans at 880 nm (filled blue circles), followed by ten successive excitation scans at 950 nm (empty red circles). The pair of 880-nm/950-nm scans was repeated two additional times, for a total of thirty excitation scans at each wavelength. The total emission intensity was computed by integrating over the entire emission spectrum. **(b)** Comparison of excitation spectra for before (black line with filled circles) and after (gray line with empty circles) the entire excitation time series as shown in (a). **(c)** Emission spectra observed upon excitation at 880 nm, where the blue solid line represents the first and the blue dashed line represents the last emission spectrum obtained from the repeated time series excitations. **(d)** Emission spectra observed at an excitation wavelength of 950 nm, where the red solid line represents the first and the red dashed line represents the last emission spectrum obtained from the repeated excitation time series. All plots were normalized relatively to the maximum value observed in the respective data set. The final concentration of mCitrine in the FP-doped polyacrylamide gel was 1 μM. For repeated excitation time series, the integration time of the camera was 200 ms and the excitation power per entire excitation line was 200 mW (energy, 100 μJ per pixel). For the excitation spectra measurements, the integration time was 50 ms and the excitation power was 100 mW/line (energy, 12.5 μJ per pixel).

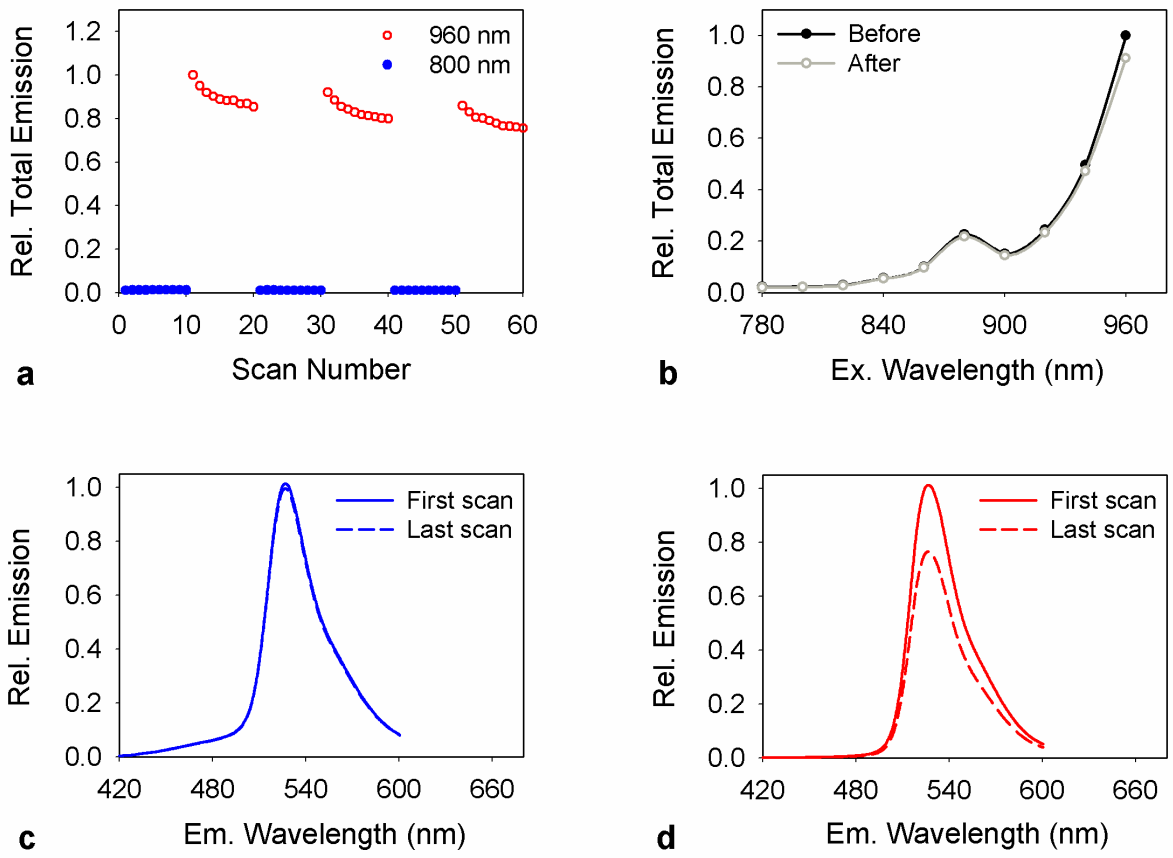

Figure 3.15. Response to repeated two-photon excitation scans of PAA gel doped with monomeric Super Yellow Fluorescent Protein 2 (SYFP2) at pH 8. (a) Changes in total emission intensity induced by acquiring time series of ten successive excitation scans at 800 nm (filled blue circles), followed by ten successive excitation scans at 960 nm (empty red circles). The pair of 800-nm/960-nm scans was repeated two additional times, for a total of thirty excitation scans at each wavelength. The total emission intensity was computed by integrating over the entire emission spectrum. **(b)** Comparison of excitation spectra for before (black line with filled circles) and after (gray line with empty circles) the entire excitation time series as shown in (a). **(c)** Emission spectra observed upon excitation at 800 nm, where the blue solid line represents the first and the blue dashed line represents the last emission spectrum obtained from the repeated time series excitations. **(d)** Emission spectra observed at an excitation wavelength of 960 nm, where the red solid line represents the first and the red dashed line represents the last emission spectrum obtained from the repeated excitation time series. All plots were normalized relatively to the maximum value observed in the respective data set. The final concentration of SYFP2 in the FP-doped polyacrylamide gel was 1 μM. For repeated excitation time series, the integration time of the camera was 200 ms and the excitation power per entire excitation line was 200 mW (energy, 100 μJ per pixel). For the excitation spectra measurements, the integration time was 50 ms and the excitation power was 100 mW/line (energy, 12.5 μJ per pixel).

3.3.2. pH dependence of the photophysical properties of mGFP2

Typical results obtained from performing an excitation time series (using the pair of excitation wavelengths 960 nm and 800 nm) on mGFP2 doped PAA gel at two different pH values (i.e., pH = 6 and pH = 4) are shown in Fig. 3.16. These results could also be compared to those obtained at pH 8, shown in Fig. 3.2. As seen, the emission intensity traces for successive excitation scans at 960 nm (open red circles in Fig. 3.16a-b) were significantly different for different pH values. For pH 6 (see Fig 3.16a), an increase was observed in total emission intensity under 960-nm excitation (i.e., photo-switching) after successive excitations at 800 nm. The effect of photo-switching at this pH was weaker than that observed at pH 8 (Fig. 3.2a) and much stronger than seen at pH 4 (see Fig 3.16b); in the latter case, the effect of photo-switching was completely eliminated, i.e., there was no increase in emission signal under 960-nm excitation following successive excitations at 800 nm. Likewise, the degree of change in the excitation spectrum (see Fig. 3.2b, 3.16c-d) decreased with pH. Overall, these changes suggest that mGFP2 chromophore switching from protonated (neutral) to anionic forms occurs less frequently when the pH of the gel was lowered from pH = 8 to pH = 6 and is completely eliminated for pH 4. This result confirms the mechanism underlying the observed photo-switching: as the pH decreases the concentration of the protonated form of GFP2, relative to the deprotonated form of the molecule will increase, due to the presence of excess H^+ in the gel at low pH. In other words, any photo-switching to the anionic version of the chromophore would be short-lived, due to the composition of the surrounding gel, and therefore the concentration of the protonated form of GFP2 will remain significantly higher than the deprotonated form, even after repeated excitations at 800 nm. Unfortunately, even though there

was less photo-switching at low pH, most FPs, including GFP2, lose fluorescence at a pH lower than their neutral pKa, and so it is not practical to use solutions with low pH.

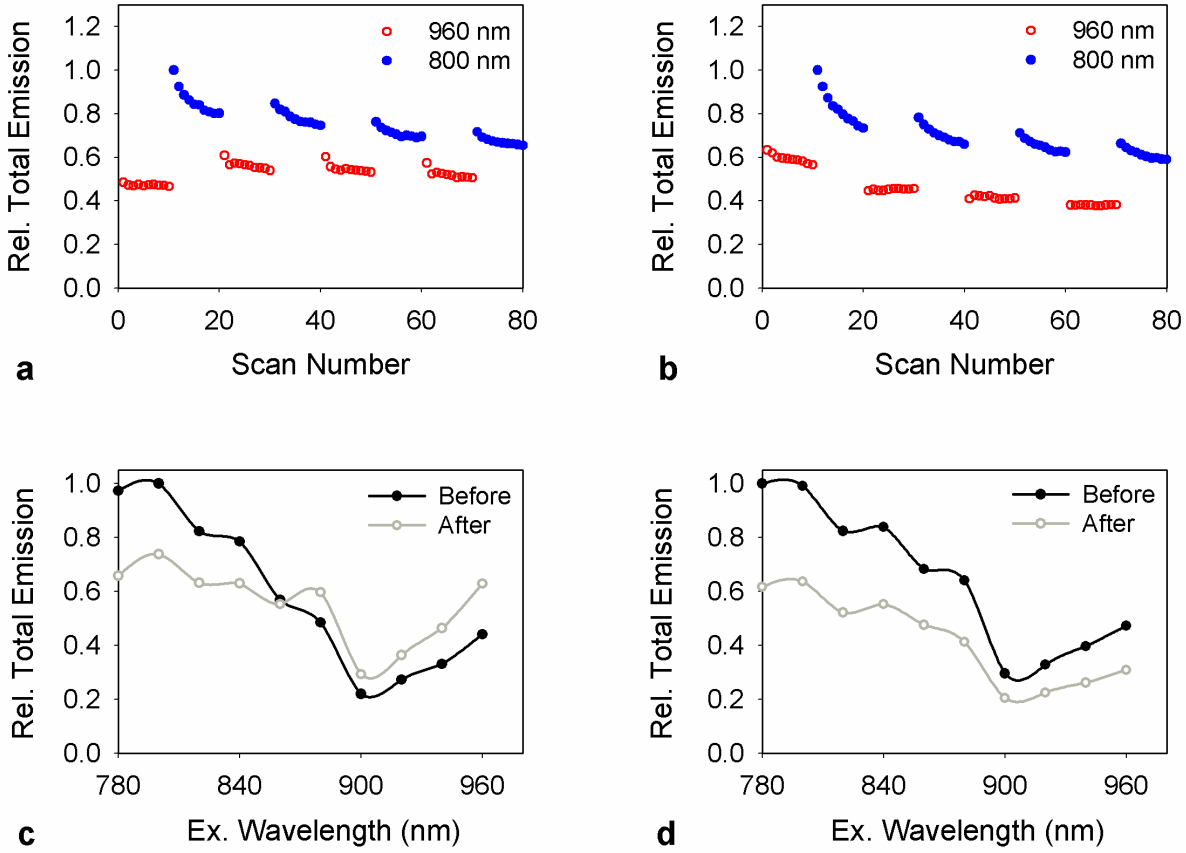

Figure 3.16. Effects of pH on photophysical properties of mGFP2 in response to repeated time series excitations. (a-b) Change in total emission intensity mGFP2 induced by acquiring time series of ten successive excitation scans at 960 nm (empty red circles), followed by ten successive excitation scans at 800 nm (filled blue circles) for mGFP2 doped PAA gel samples at pH values of 6 (panel a) and 4 (panel b), respectively. The couple of 960-nm/800-nm scans was repeated three additional times, for a total of forty excitation scans at each wavelength. **(c-d)** Comparison of excitation spectra before (—●—) and after (—○—) the entire excitation time series as in **(a-b)** for the sample at pH 6 (panel c) and pH 4 (panel d), respectively. All plots were normalized relatively to the maximum value observed in the respective data set. The final concentration of mGFP2 in the FP-doped polyacrylamide gel was 1 µM. For repeated time series excitations, the integration time of the camera was 200 ms and the excitation power per entire excitation line was 200 mW (corresponding to 0.5 mW per pixel). For repeated excitation time series, the integration time of the camera was 200 ms and the excitation power per entire excitation line was 200 mW (energy, 100 µJ per pixel). For the excitation spectra measurements, the integration time was 50 ms and the excitation power was 100 mW/line (energy, 12.5 µJ per pixel).

In contrast to the large effect pH had on the ability of mGFP2 to undergo photo-switching, we found no significant change to the extent of photobleaching for mGFP2 samples with pH (cf. Figs. 3.2 and 3.16). Specifically, repeated excitations at 800 nm caused a decrease in the total emission intensity for the samples at all three pH values, due, in part, to photobleaching of the sample. For the particular case of the mGFP2 sample, it is difficult to quantify the extent of photobleaching which is occurring as a result of the 800 nm excitations, because the decrease in emission intensity is a result of two factors, photobleaching and photo-switching of some of the chromophores to the anionic state and is difficult to decouple the effects of these two factors. Therefore, it might be the case that there is some small quantitative difference between the exact percentage of molecules which are photobleached in the three different pH cases, although, qualitatively, such differences appear to be minimal.

3.3.3. Relative brightness of FPs under 2p excitation

In addition to photostability, the intrinsic brightness, which is linearly proportional to the number of photons an FP emits per measurement period, is a vital characteristic to keep in mind when selecting the correct FP to use. The intrinsic brightness of any fluorescent molecule depends on two properties of the molecule, namely the extinction coefficient (or the excitation cross-section) of the FP, which is a measure of the ability of the FP to absorb light, and the quantum yield, which is a measure of the efficiency of photon emission once the FP is in an excited state. These properties could be affected by various environmental as well as instrumental factors such as pH, temperature, excitation light intensity, and wavelength.

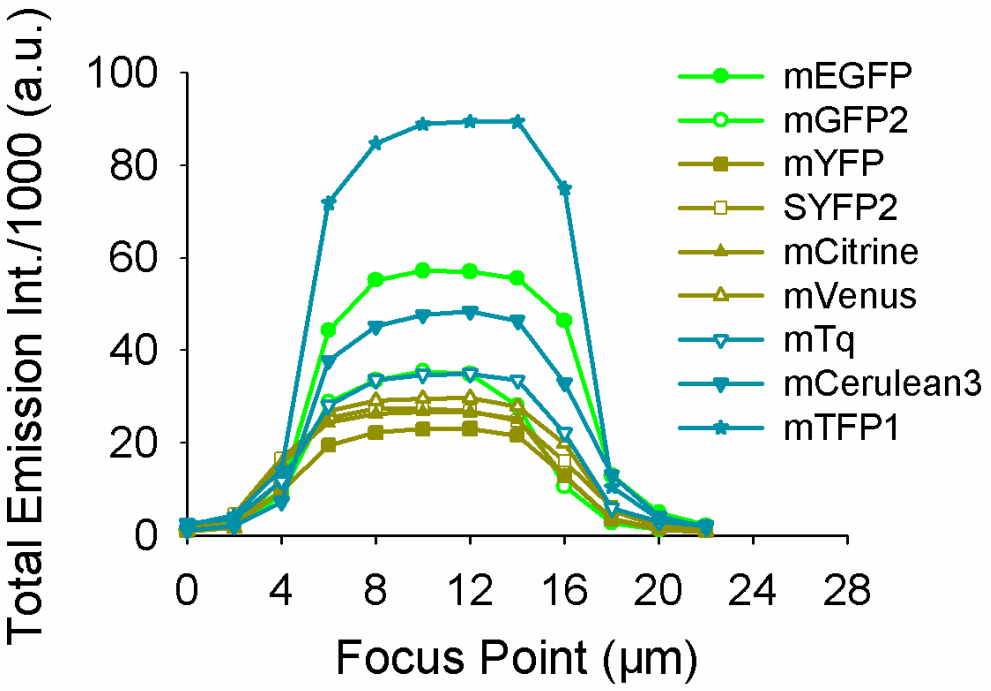

Figure 3.17. Comparison of the total emission intensity of a variety of FPs. The FP-doped polyacrylamide gel samples were prepared using DPBS buffer (pH = 8) with a final FP concentration of 1 µM. Z-stack acquisitions (see Methods section) were taken for each FP sample with an average power of 12 mW/point and at integration time of 100 ms (corresponding to an excitation energy of 0.75 µJ per pixel). The excitation wavelength chosen for the z-stack acquisitions corresponded to the peak of the respective FP's excitation spectra, as described above.

Because the brightness of an FP depends on an array of different parameters, in this work, we sought to determine the relative 2p brightness of all the FPs which have been investigated in this study by using the same acquisition settings and sample preparation protocol for each. In order to accomplish this, each prepared sample of PAA gel-embedded FP was scanned by focused light at different depths and the fluorescence intensity determined at each depth, to create a "sample uniformity curve" (see Fig. 3.17). The purpose of the uniformity curve was to assure that the FPs were not distributed inhomogeneously throughout the sample, which would negate one of the crucial parameters which needs to remain constant for a proper comparison of brightness values, i.e., the concentration of the sample. Only emission intensity

profiles were used for further analysis that formed a plateau which consisted of at least four approximately equal total emission intensity values acquired from consecutive planes in the center of the gel sample. The decrease in intensity on both sides of the plateau was due to the decrease in the overlap between the point spread function of the focused light and the sample film.

We have defined the 2p relative brightness to be the ratio of total emission intensity of an FP to that of mEGFP, whereas total emission intensity was found by averaging the results of the multiple measurements along the plateau of the uniformity curve. Based on the total emission intensities, the fluorescent protein mTFP1 is the brightest of the measured FPs followed by mEGFP, mCerulean3, mTq, mGFP2, mVenus, SYFP2, mCitrine, and mYFP (see Fig. 3.17). The results of this assay are summarized in Table 3.1, alongside with those regarding photobleaching and photo-switching described in previous sections. Interestingly, the results shown in Table 3.1 reveal that the relative brightness of the various FP subfamilies using 2p excitation are significantly different than the relative brightness values of the FPs determined using 1p excitation. For example, the yellow subfamily of proteins is the brightest using 1p excitation, but the dimmest using 2p excitation.

Table 3.1. Summary of photophysical properties of FPs investigated in this study. Values resulting from 2p excitation were determined as described in this work, while those resulting from 1p excitation, as well as pKa values and lists of mutations were obtained from the literature (indicated in the column for 1p Brightness).

FP	pKa	1p Relative Brightness*	2p Relative Brightness†	2p Photo-bleaching‡	2p Photo-switching
mEGFP[a]	6.0	1.00 [4, 26]	1.00 ± 0.06	0.25 ± 0.09	No
mGFP2[b]	-	0.34 [52, 66]	0.63 ± 0.06	-	Yes
mYFP[c]	6.9	1.51 [26, 128]	0.41 ± 0.05	0.09 ± 0.07	No
mVenus[d]	6.0	1.56 [53, 55]	0.52 ± 0.04	0.11 ± 0.05	No
SYFP2[e]	6.0	2.04 [55]	0.50 ± 0.04	0.17 ± 0.09	No
mCitrine[f]	5.7	1.74 [35, 53]	0.47 ± 0.12	0.03 ± 0.02	No
mCerulean3[g]	3.3	1.03 [57]	0.85 ± 0.09	0.61 ± 0.06	No
mTq[h]	4.5	0.75 [58]	0.63 ± 0.03	0.65 ± 0.04	No
mTFP1[#]	4.3	1.60 [4]	1.56 ± 0.07	0.47 ± 0.02	Yes

Notes: *Relative to the brightness of mEGFP, which is 33,600 $m^{-1}M^{-1}$for 1p excitation. 1p brightness was calculated by multiplying the extinction coefficient (ε) and quantum yield (Q) using in Table 1.1 from Chapter 1. †Observed emission intensity for given FP at pH 8 relative to the observed emission intensity of mEGFP. ‡Fraction of total fluorescence bleached from first 10 excitation scans using the specific peak excitation wavelength of each FP. The variants of green fluorescent protein incorporated the following mutations relative to the wild-type: [a] mEGFP: F64L, S65T, A206K; [b] mGFP2: F64L, A206K; [c] mYFP: S65G, V68L, Q69K, S72A, T203Y, A206K; [d]mVenus: F46L, F64L, S65G, V68L, S72A, M153T, V163A, S175G, T203Y, A206K; [e] SYFP2: F46L, F64L, S65G, S72A, M153T, V163A, S175G, T203Y, A206K; [f] mCitrine: S65G, V68L, Q69M, S72A, T203Y, A206K; [g] mCerulean3: F64L, Y66W, S72A, Y145A, N146T, S147H, H148G, M153T, V163A, K166G, I167L, R168N, H169C, A206K; [h]mTq: F64L, Y66W, S72A, N146I, H148D, M153T, V163A, S175F, A206K. [#]mTFP1: a variant of cFP484 derived from Clavularia coral, not from jellyfish.

3.4. Discussion

Along with the experimental parameters used in the imaging system (power, wavelength, spectral resolution, and exposure time), the source of illumination and detector used in an imaging system could also alter the observed intensity of the fluorescent molecules. Our comparative analysis of the photophysical properties of a large number of widely used FPs provided some interesting insights.

Of the FPs studied in this work, we found that mEGFP is the brightest among those which have been derived from wtGFP, and it exhibited only moderate photobleaching and no noticeable photo-switching under 2p excitation. Because of these features, mEGFP is one of the best options for those fluorescence applications that require high photostability and brightness such as FRET [8, 97, 133] and Number and Brightness (N&B) analysis [134]. Nevertheless, other factors may factor in when choosing a good FRET pair for a certain experiment, including good separation between donor and acceptor emission spectra, which is necessary in imaging experiments without spectral resolution. Another green variant of wtGFP, GFP2, exhibited strong irreversible photo-switching from one sub-population (excitation state) to another, which are excited maximally by different wavelengths. This photo-switching effect significantly depends on the pH of the sample.

Cyan variants of wtGFP, namely mCerulean3 and mTq showed high propensities to photobleach with no significant effect of photo-switching. This observed result suggests that mTq and Cerulean3 could be appropriate options for the FRAP experiments because of their high propensity to photobleach. These FPs (i.e., mTq, and mCerulean3) were brighter than all the yellow variants of wtGFP measured in this study. Another Cyan FP (but derived from CFP484 [4]), mTFP1, is the brightest among the measured FPs in this investigation. Based on

our measurements, mTFP1 exhibits a pronounced effect of photobleaching; however, not as pronounced as the other cyan FPs. In addition to that, a minute but noticeable, irreversible photo-switching from one fluorescence color to another was observed under 2p excitation on PAA gel-doped mTFP1.

The yellow variants of the wtGFP measured in this investigation, namely mCitrine, mYFP, mVenus, and SYFP2 were dimmer than both green variants and cyan variants tested in this study. Among these yellow variants of wtGFP, we found mVenus is brightest and mYFP is the dimmest under 2p excitation. This entire subclass of FPs showed a small effect of photobleaching with essentially no effect of photo-switching under 2p excitations. Based on these results we conclude that yellow FPs studied here are likely to be a good choice for measurements that require strong photostability.

Based on those observations, we note that the choice of FPs depends on the specific application considered. For instance, for FRAP studies one could choose cyan variants, while for applications that require switching, GFP2 and perhaps mTFP1 could be used. At the same time, for experiments where steady, long-lasting fluorescence is needed, there are several choices available. Even in this case, FPs that exhibit photo-switching and photobleaching may still be used by choosing less intense laser light with an excitation wavelength that minimizes photobleaching and photo-switching while maintaining a relatively high brightness, if applications do not require FP immobilization under continuous excitation.

In conclusion, our study adds to the body of evidence that the specific photophysical properties of fluorescent proteins under two-photon excitation, including excitation and emission spectra, as well as their propensity to undergo light-induced changes, may not be simply inferred from one-photon excitation. Lack of knowledge or appreciation of such

properties may lead to erroneous conclusions in, e.g., FRET studies [80]. Thus, the choice of fluorescent proteins for a particular experiment depends, among other things, on whether one uses single- or two-photon excitation. The next chapter (i.e., Chapter 4) will present how FRET efficiency behaves with changing photophysical effects of fluorescent molecules utilizing both experimental measurements and numerical simulations.

Chapter 4. Impact of photobleaching of FPs on FRET

In this chapter, we investigate the impact of photophysical effects of fluorescent proteins (FPs) on FRET measurement at various experimental condition under two-photon excitation (see reference [135]). Our investigation follows the understanding gained in Chapter 1 and 3 regarding the FPs and their photophysical properties, and the underlying concept of FRET theory as discussed in Chapter 2. Expanding upon this foundation, we aim to thoroughly analyze FRET efficiencies under various excitation conditions, using dimeric and trimeric FRET constructs expressed in the cytoplasm of CHO cells. Herein, our study delved deeper by quantifying how photobleaching significantly impacts FRET measurements, and offers guidelines for conducting these measurements accurately.

4.1. Overview

Förster resonance energy transfer (FRET) is a physical phenomenon that involves the non-radiative transfer of energy between an excited fluorescent molecule, called a donor (D), and a neighboring unexcited fluorescent molecule called an acceptor (A) via dipole-dipole interaction [60, 64, 65]. FRET has been used to probe the proximity of individual molecules within protein complexes [136, 137], track complex formations [138], monitor dynamic protein interactions [7, 139], and detect conformational changes of macromolecules [133, 140-142] in living organisms. More recently, a FRET technique, called FRET spectrometry, has been developed, which can determine the relative distances between protomers within oligomeric complexes (i.e., quaternary structure) in living cells [6, 8-10, 143, 144].

In order to determine the quaternary structure of biological macromolecules using FRET, it is crucial to understand how the mechanism of FRET works when more than one acceptor are close to an excited donor, as can occur for macromolecules larger than a dimer.

Fortunately, the kinetic theory of FRET [85] provides a theoretical basis for predicting the FRET occurring in multimeric complexes. According to the theory, the FRET efficiency of an oligomer containing multiple acceptors can be predicted from the FRET efficiency occurring between each individual donor-acceptor pathway present in the complex. The theory was tested using simulated data [89] and found to accurately predict the FRET occurring in oligomeric complexes in the particular situation where proximity FRET [89] is minimal. The first experimental attempt to test the kinetic theory of FRET [87] found an ~15% discrepancy between the measured FRET efficiency of a multimeric complex consisting of a single donor and three acceptors vs. the FRET efficiency predicted by the kinetic theory. A separate investigation of the same constructs found a substantially smaller discrepancy (4%) but still concluded the discrepancy was statistically significant [88].

A recently published thorough theoretical analysis of the FRET equations identified numerous theoretical assumptions traditionally used to compute FRET efficiency from experimental data could lead to significant systematic errors if not carefully considered in the context of the experimental protocols used [80]. These improperly applied assumptions explain some of the discrepancies between measured and theoretically predicted FRET values, which were observed in experiments testing the kinetic theory of FRET. For instance, in FRET measurements performed using continuous wave (cw) excitation, the equations for determining the FRET efficiency depend on the ratio between the probability of donors to be in the ground state in the presence and absence of FRET; these probabilities have typically been set equal to one in traditional FRET applications, even though when using cw excitation, the value is significantly different than one.

The error caused by the dependence on the integrated probability can be avoided by using pulsed lasers, as it is done in systems relying on two-photon excitation. For two photon excitation of, any discrepancies between measured and theoretical FRET efficiency values are due to a general inability to assess the contributions of photophysical effects, such as photobleaching [14, 145] and photoconversion [14, 117, 146] of donors and acceptors, to the measured FRET efficiencies for chosen laser excitation powers.

In addition, since most fluorescent proteins present short Stokes shifts the excitation wavelengths available to excite the donors quite often also lead to direct excitation of the acceptor, which results in an erroneous FRET efficiency readout. Contributions of direct excitation of the acceptor to the measured FRET efficiency can be corrected for by scanning the sample of interest at two [10, 80], or sometimes three [147] different excitation wavelengths instead of one. This in turn may result in additional, caused by the additional excitation wavelengths, which are typically not taken into account but could also affect the FRET efficiency calculation as these effects inevitably change the proportion of donors and acceptors actively involved in FRET.

To avoid significant errors in FRET spectrometry studies and thus accurately determine the interprotomeric distances within oligomers, it is critically important to map out the contributions of photophysical effects to experimentally determined FRET efficiencies under a range of experimental conditions. In this work, we performed two-photon (2P) micro-spectroscopy measurements on living cells expressing FRET constructs of the type used in previous studies [88, 148, 149], consisting of single donor molecule linked to either its C- or N-terminus with one acceptor to form dimers, or linked to both termini with acceptors and therefore form FRET trimers. The kinetic theory of FRET was used to determine the range of

excitation powers and combination of wavelengths for which the correct relationship exists between the FRET efficiency of dimers and those of trimers. In addition, for comparatively higher excitation powers, we used a simple but effective numerical method to estimate the degree to which photobleaching of donors and acceptors was responsible for the observed discrepancies between the two sets of FRET efficiencies. In light of these analyses, we quantified photobleaching effects and the extent of their contributions to FRET investigations, as well as identified the general conditions for performing accurate FRET spectrometry measurements using fusion fluorescent proteins [9, 10, 143, 144].

4.2. Materials and methods

4.2.1. Fluorescent protein constructs

The plasmids for all the protein constructs used in this work are gifts from Dr. Stephen Vogel. They were expressed and localized in the cytoplasm of Chinese hamster ovary (CHO) cells (see section 2.2). The fluorescent protein fusion constructs [148] used to study FRET were made from combinations of three domains (see Fig. 4.1): Cerulean, as a donor (D) of energy, Venus, as an acceptor (A) of energy, and Amber, a non-fluorescent (N) structural place holder containing a point mutation preventing chromophore formation. Two of the constructs (denoted as NDA and ADN hereafter) are dimeric from the FRET standpoint, as they consisted of a single D and a single A involved in energy transfer. The third construct (denoted as ADA) is referred to below as a trimer, since it contains three fluorescent domains, consisting of two As and one D. Cells expressing a construct consisting of Amber fused to Cerulean (i.e., Amber-5-Cerulean, A5C) were also imaged to obtain the emission spectrum for Cerulean. Finally, the

emission spectrum of the acceptor was acquired by imaging CHO cells expressing the Venus protein, which is also localized in the cytoplasm.

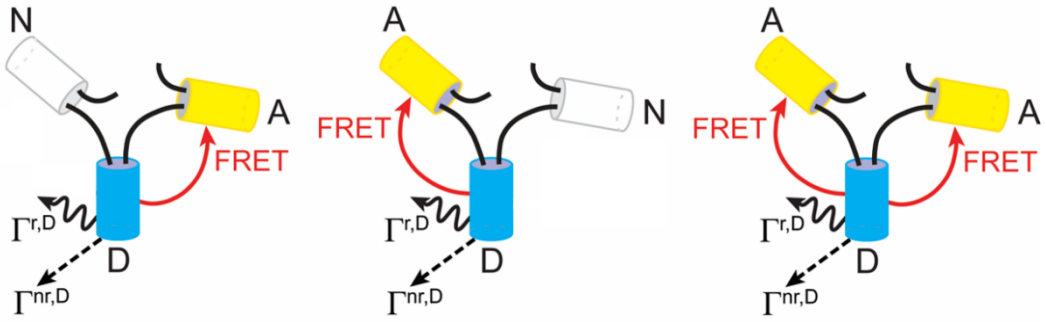

Figure 4.1. Schematic representation of cytoplasmic FRET constructs and the various pathways for energy loss from the excited donor. White cylinders represent amber (a non-fluorescent structural placeholder, N), cyan cylinders represent the fluorescent molecule Cerulean (a donor of energy, D), and yellow cylinders represent Venus (an acceptor of energy, A). The various arrows indicate possible pathways through which the excited donor loses energy. Wavy arrows indicate radiative loss ($\Gamma^{r,D}$), dashed arrows indicate non-radiative loss ($\Gamma^{nr,D}$), and solid arrows pointing toward A from D depict energy transfer through FRET (Γ^{FRET}).

4.2.2. Cell culture and protein expression

CHO cells were grown in Dulbecco's modified Eagle's medium (DMEM) supplemented with 10% fetal bovine serum, 1% L-glutamine, 1% penicillin/ streptomycin, and 1% non-essential amino acids. All reagents were purchased from Fisher Scientific unless noted otherwise. Cells were seeded onto 35-mm No. 1.5 coverglass culture dishes (Part No. NC079415, Cellvis, CA), at a density of 7×10^4 cells per dish; the dishes incubated for 48 h at 37 ^{o}C in a humidified environment with 5% CO_2. One such dish was prepared for each of the samples mentioned in section 2.1, for a total of 5 dishes. After incubation, each dish was transfected with a single plasmid encoding for one of the five constructs described above. A total of 2 µg plasmid DNA was used for the transfection procedure, along with 8 µl lipofectamine 2000 (Invitrogen,

Carlsbad, CA) and diluted in 250 µl OptiMEM (Invitrogen), according to a previously described procedure [150]. After transfection, the dishes were returned to the incubator. After 24 h, the dishes were removed from the incubator and taken for imaging. For imaging, the cell growth medium was removed, and the cells were first rinsed with Dulbecco's phosphate-buffered saline (DPBS; REF:14190-144, Life Technologies, NY) then resuspended in DPBS.

4.2.3. Spectrally resolved imaging

Spectrally resolved fluorescence images of CHO cells expressing the cytoplasmic fluorescent constructs were acquired using a previously described two-photon (2P) optical micro-spectroscope [66]. This imaging system consisted of a mode-locked Ti-Sapphire laser (Mai Tai^{TM}, Spectra Physics, Santa Clara, CA), which generated 100 fs pulses with tunable central wavelengths between 690 nm and 1040 nm and was used as the excitation source, an OptiMiS^{TM} scanning/detection head (Aurora Spectral Technologies, Grafton, WI), and an inverted Nikon Eclipse Ti^{TM} microscope (Nikon Instruments, Inc. Melville, NY) equipped with an infinity-corrected oil-immersion objective (NA=1.45, 100×). The OptiMiS detection head used a non-de-scanned acquisition scheme in which emitted fluorescence was spectrally resolved by passing it through a transmission grating and projecting it onto a cooled electron-multiplying charge-coupled device (EMCCD) camera (iXon Ultra 897; Andor Technologies, South Windsor, CT), similar to previously described systems [6, 66, 91]. The excitation beam was focused to a diffraction-limited spot which was scanned across the sample along an entire line consisting of 440 pixels (with a pixel dwell time of 35 milliseconds) while the camera integrated the fluorescence signal during the course of the entire sweep. 300 such lines were scanned, which each such line providing an entire emission spectrum for each pixel. By raster scanning

the beam across the sample in this manner, we acquired 3D fluorescence micro-spectroscopic image stacks, with two dimensions representing spatial distribution of the fluorophores and the third dimension corresponding to the emission spectrum. The spectral resolution was set at 1.1 nm.

Three different pairs of excitation wavelengths (800 nm/880 nm, 800 nm/960 nm, and 880 nm/960 nm, maintaining their order) and various excitation powers (15 mW/point, 42 mW/point, 52 mW/point, and 62 mW/point) were used to explore the impact of excitation wavelength and power on the determination of FRET efficiency. Each field of view was scanned using a single excitation power and a single pair of excitation wavelengths. For each excitation power, four to five experiments were conducted, each of which generated a complete set of measurements of all FRET constructs, acquired using all three pairs of excitation wavelengths (~10 fields of view, or about 30 cells, per excitation power per wavelength pair). All measurements were taken by focusing the laser on the cross-sections of CHO cells, particularly the parts corresponding to the cytoplasm, which were cultured on the coverslip surface as described in section 2.2.

4.2.4. Image analysis and calculation of FRET efficiency

4.2.4.1. Spectral unmixing and segmentation of intensity map

The composite emission spectrum from each pixel in the micro-spectroscopic images of cells expressing cytoplasmic trimeric FRET constructs was deconvolved (unmixed) into donor (D) and acceptor (A) components using linear regression, as described elsewhere [5, 10, 66]. The elementary spectra for Cerulean [151] (donor) and Venus [152] (acceptor) used in the unmixing procedure were obtained by imaging cells expressing A5C only and Venus only, respectively

[88]. By applying the unmixing procedure to each pixel of a fluorescence micro-spectrograph, we obtained 2D maps of donor intensity in the presence of acceptor, k^{DA}, and acceptor intensity in the presence of the donor, k^{AD}. The k^{DA} and k^{AD} values thus obtained were multiplied by the area underneath the elementary spectra of D and A, respectively, to obtain the total donor fluorescence emission in the presence of the acceptor, F^{DA}, and total acceptor fluorescence emission in the presence of donor, F^{AD}, for each image pixel. Pixel-level apparent FRET efficiency values, E_{app}, were calculated using the corresponding F^{DA} and F^{AD} at each pixel (see section 4.2.4.2). F^{DA} map were used to manually demarcate regions of interest (ROIs) in the micro-spectroscopic scans, which were then segmented into areas of ~900 pixels using a moving-square algorithm described in a previous publication [101]. The pixel locations for each segment were saved and paired to the corresponding image source. In the dual-wavelength excitation approach, segment-level FRET efficiency values were calculated using the average F^{DA} and F^{AD} obtained for the corresponding segment (see section 4.2.4.3).

4.2.4.2. E_{app} determination using single-wavelength excitation

For excitation wavelengths that do not lead to appreciable direct excitation of the acceptor, the FRET efficiency can be calculated from using the following equation [66]:

$$E_{single} = \left[1 + \frac{Q^A F^{DA}}{Q^D F^{AD}}\right]^{-1}, \tag{4.1}$$

where Q^D and Q^A are the quantum yields of the donor (D) and acceptor (A), respectively. Determining FRET efficiency values using the single-wavelength excitation method is simpler

to implement and less prone to calibration errors but it could lead to inaccurate FRET efficiency values when its underlying approximation does not hold.

Following, pixel-level E_{single} calculation, we split the ROIs in each cell into segments, as described above, and a histogram of E_{single} values was constructed for each segment using a bin size of 0.005. Then, the dominant peak of each individual segment histogram was extracted and used to create a "meta-histogram" of the dominant peak positions. The bin size used to construct the meta-histogram was chosen to be equal to 0.02, as described previously[6, 143, 144]. Finally, we extracted a measured value of the FRET efficiency, E_{single}, from the meta-histogram for each FRET construct using the dominant peak (mode) position of the meta-histogram.

4.2.4.3. E_{app} determination using single-wavelength excitation

Scanning the sample at two excitation wavelengths allowed us to obtain the concentrations of both Ds and As, and to correct the computed FRET efficiency from inadvertent contributions from direct excitation of the acceptors. Spectral unmixing of such images resulted in four separate 2D maps: the fluorescence signal of the donor obtained from the first (F_1^{DA}) and second (F_2^{DA}) excitation wavelengths and the acceptor emission at the first (F_1^{AD}) and second (F_2^{AD}) excitation wavelengths. In this case, the FRET efficiency was computed via the following equation [80]:

$$E_{dual} = \left[1 + \frac{\langle F_1^{DA}\rangle(1-\rho^{ex,A}/\rho^{ex,D})}{\langle F_1^{AD}\rangle - \langle F_2^{AD}\rangle\rho^{ex,A}} \frac{Q^A}{Q^D}\right]^{-1}, \quad (4.2)$$

where Q^D and Q^A are the quantum yields of the donor and acceptor, respectively, the subscript in $\langle F_x^{DA} \rangle$ or $\langle F_x^{AD} \rangle$ is x = 1 for the first excitation wavelength, and x = 2 for the second; while the $\langle\ \rangle$ symbol represents the average over all pixels in an ROI segment. The quantities $\rho^{ex,D}$ and $\rho^{ex,A}$ are the intensity ratio of the donors and acceptors, respectively, between the two excitation wavelengths, i.e., $\rho^{ex,y} = \langle F_1^y \rangle / \langle F_2^y \rangle$ where *y=D or A;* these ratios were obtained by scanning samples expressing only the donor or only the acceptor using the same pair of excitation wavelengths. The dual-wavelength excitation scheme compensates for any direct excitation of the acceptor and also provides the donor and acceptor concentration – which enables the straightforward calculation of the acceptor molar fraction, as described in detail in previous publication [6].

In this study, we used three different excitation wavelength pairs for the dual-wavelength excitation protocol: 800 nm/880 nm, 800 nm/960 nm, and 880 nm/960 nm. The values of $\rho^{ex,A}$ and $\rho^{ex,D}$ are dependent on the specific pair of excitation wavelengths used to implement the dual-excitation scan. Therefore, the cells expressing Venus and A5C were measured separately to acquire the calibration factors $\rho^{ex,D}$ and $\rho^{ex,A}$ for each pair of wavelengths. A single value of E_{dual} was calculated per image segment (as opposed to per pixel as described in the previous section) using the average values of F_1^{DA}, F_1^{AD}, F_2^{DA}, and F_2^{AD} from the corresponding segment, because molecules can diffuse into and out of a pixel within the time it takes to change the excitation wavelength of the laser and scan the sample again. Subsequently, we determined the measured FRET efficiency for the dual-wavelength excitation method by averaging E_{dual} values across all segments from all measurements for each specific construct.

4.2.4.4. Calculation of the weighted average and standard error of the FRET efficiency

Four to five datasets were collected for each of the three FRET constructs at each of the excitation powers and pairs of excitation wavelengths. Those results were used to compute a weighted average for each construct for a specific power and excitation wavelength pair using following equation:

$$E = \frac{\Sigma_m \frac{1}{\sigma_m^2} E_m}{\Sigma_m \frac{1}{\sigma_m^2}}, \tag{4.3}$$

where, E_m and σ_m represent the average and standard deviation, respectively, of the FRET efficiency distribution for each dataset, m.

Similarly, the variability associated with each of the weighted average of the FRET efficiency values was obtained from the weighted standard deviation of the corresponding FRET values, using following equation:

$$\mathrm{SE_w} = \left(\Sigma_m \frac{1}{\sigma_m^2}\right)^{-\frac{1}{2}}, \tag{4.4}$$

where, E_m and σ_m are the measured FRET efficiency and standard deviation, respectively, obtained for each dataset.

4.2.5. Relationship between FRET dimers and trimers

For the ADA multiplexes containing more than one acceptor, the FRET efficiency may not only be measured directly but also predicted using Eqn. (2.111) in section 2.4.2,

$$E_{ADA}^{pred} = \frac{\sum_{j=1}^{n-1} E_j/1 - E_j}{1 + \sum_{j=1}^{n-k} E_j/1 - E_j}, \tag{4.5}$$

in which n = 2, and E_j for j =1,2 are replaced by the measured FRET efficiencies of the dimeric FRET constructs NDA and ADN to obtain:

$$E_{ADA}^{pred} = \frac{E_{NDA}/(1 - E_{NDA}) + E_{ADN}/(1 - E_{ADN})}{1 + E_{NDA}/(1 - E_{NDA}) + E_{ADN}/(1 - E_{ADN})}, \tag{4.6}$$

A value of E_{ADA}^{pred} was computed using this relationship for each excitation condition (i.e., excitation wavelengths and powers) using the values obtained from separate measurements on the constructs NDA and ADN using the same imaging conditions.

The kinetic theory of FRET was tested by comparing the measured FRET efficiency of the ADA construct, E_{ADA}, with the predicted FRET efficiency of the same construct, E_{ADA}^{pred}, obtained using Eq. 4.6 and the measured FRET efficiencies of the ADN and NDA complexes. In order to gauge whether any significant difference between E_{ADA} and E_{ADA}^{pred} was found, we needed to the find the variability (error) associated with both the measured and predicted quantities. The error associated with the predicted FRET value of the ADA complex, δE_{ADA}^{pred},

was found using linear error propagation of the individual NDA and ADN measurements as follows:

$$\delta E_{ADA}^{pred} = \frac{\frac{\sigma_{E_{NDA}}}{(1-E_{NDA})^2} + \frac{\sigma_{E_{ADN}}}{(1-E_{ADN})^2}}{\left(\frac{E_{NDA}}{1-E_{NDA}} + \frac{E_{ADN}}{1-E_{ADN}}\right)\left(1 + \frac{E_{NDA}}{(1-E_{NDA})} + \frac{E_{ADN}}{(1-E_{ADN})}\right)}, \tag{4.7}$$

where $\sigma_{E_{NDA}}$ and $\sigma_{E_{ADN}}$ are the standard deviation (SD) of the measured FRET efficiency for the constructs NDA and ADN, respectively.

It should be noted that a value of E_{ADA}^{pred} was calculated for each excitation condition (i.e., for various excitation wavelengths and powers) using the values obtained from separate measurements on the constructs NDA and ADN using the exact same imaging conditions.

4.2.6. Numerical method for estimating the degree of photobleaching

To estimate the effect of D and A photobleaching on the FRET efficiency we used a protocol illustrated in Figures 4.2 and 4.3. The initial step in the numerical simulation involved randomly dispersing the trimeric FRET constructs (ADA) onto an array of 1,200 pixels, with 20 constructs assigned to each pixel. Then the construct-level fluorescence signals of donor and acceptor were computed for all possible forms of the construct, are given in the table at the top of Figure 3. These construct level fluorescence signals were determined from known absorption coefficients, quantum yields, and the measured FRET values of the constructs (E_{ADN}, E_{NDA}, and E_{ADA}) obtained at the lowest excitation power of 15 mW/point (i.e., the power at which photobleaching was minimal). Next, individual donors and acceptors in the pixel array were randomly "turned off" (i.e., photobleached), so that they do not participate in FRET. The

decision process for photobleaching relied on one of the inputs photobleaching parameters. For the first step, the parameters needed were the probabilities that a donor or acceptor undergoes photobleaching after the excitation at $\lambda 1$ was completed, i.e., $P_{\lambda 1}^{D}$ and $P_{\lambda 1}^{A}$, respectively. If the fluorescent molecule was assumed as photobleached, it was then converted into a non-fluorescent molecule, N, and the original ADA construct was reclassified as a different species. If, for example the random decision process resulted in the first A in an ADA construct being photobleached while the other two molecules remained unbleached, the resulting construct after this step became NDA. If the donor was assumed as photobleached the same construct became ANA, which is not FRET productive.

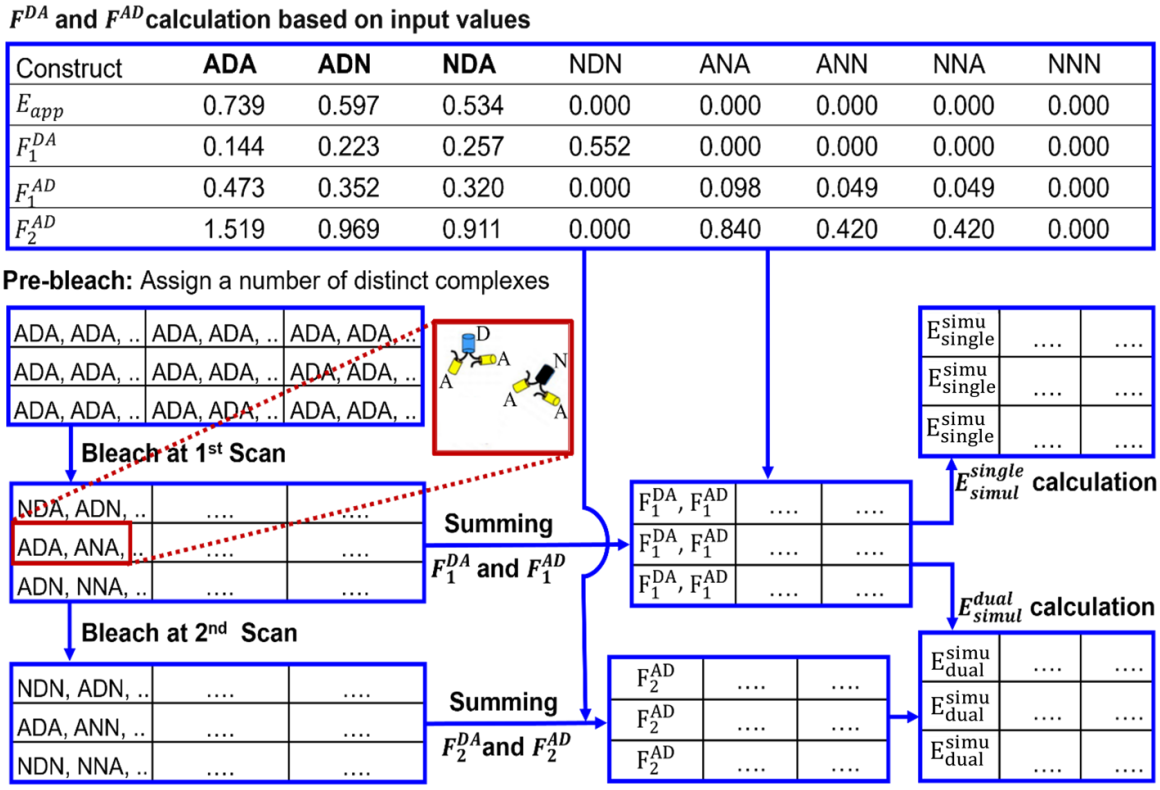

Figure 4.2. Flowchart illustrating the step-by-step process of the numerical simulation for analysing the effect of photobleaching on the FRET efficiency of a trimeric FRET construct, ADA.

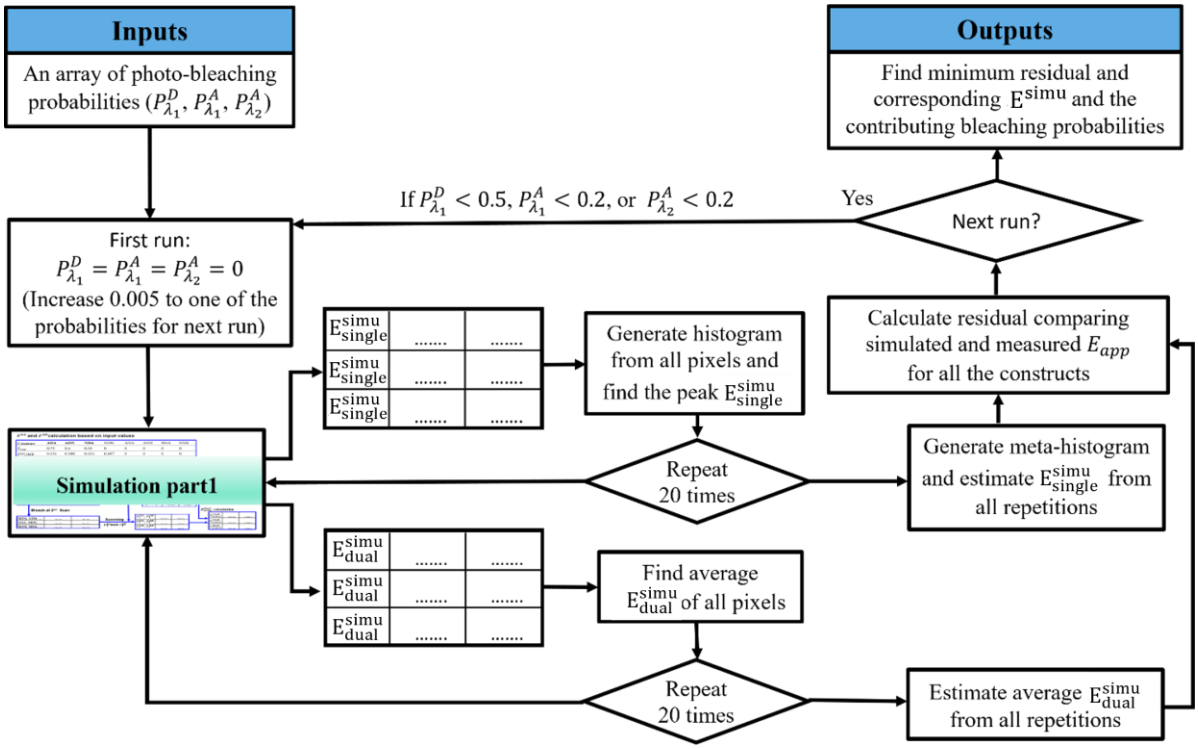

Figure 4.3. Flowchart illustrating the data fitting procedure for determining donor and acceptor photobleaching probabilities under a specific excitation condition. The procedure applied an array of photobleaching parameters to a numerical simulation of FRET complexes (workflow for the numerical simulation shown in Fig. 4.2). For each set of parameters, a FRET efficiency value was determined. These values, incorporating photobleaching probabilities, were compared with experimental FRET efficiencies using the fitting residual (Eq. 4.11). The set of parameters resulting in the minimum residual were taken as the specific contributions of donor and acceptor photobleaching in the FRET measurement under the excitation.

After repeating the process of assigning photobleached (i.e., N) status to a fraction of the molecules in each simulated pixel, we computed the total donor fluorescence signal (F_1^{DA}) and acceptor fluorescence signal (F_1^{AD}) by summing up the emitted signal from each construct in said pixel. This is akin to collecting the fluorescence intensity values resulting from the 1st excitation wavelength in the measured data. The values of F_1^{DA} and F_1^{AD} were calculated according to the following formula:

$$F_1^{DA} = \sum_l F_{1,j}^{DA} = \sum_l \left(\varepsilon_1^D Q^D N_l^D \ - \varepsilon_1^D E_l Q^D\right), \tag{4.8}$$

$$F_1^{AD} = \sum_l F_{1,j}^{AD} = \sum_l \left(\varepsilon_1^A Q^A N_l^A \ + \varepsilon_1^D E_l Q^A\right), \tag{4.9}$$

where the summation extends over all the constructs, l, in that particular pixel, and N_l^D and N_l^A are the number of D and A in a given construct arrangement, l, and E_l the FRET efficiency of said construct arrangement. Due to the possibility of undergoing photobleaching, there are $l = 8$ potential arrangements of the ADA construct which could arise due to photobleaching, i.e., ADA, ADN, NDA, NDN, ANA, ANN, NNA and NNN.

Next, we simulated the effect of random photobleaching during the second excitation step, i.e., at the second excitation wavelength. The process was similar to the first simulation step, except for utilizing a different set of input photobleaching parameters, i.e., $P_{\lambda 2}^D$ and $P_{\lambda 2}^A$. The fluorescence intensities of each pixel were calculated according to the following formula (which is similar to the one used at step 1):

$$F_2^{AD} = \sum_l F_{2,j}^{AD} = \sum_l \left(\varepsilon_2^A Q^A N_l^A \ + \varepsilon_2^D E_j Q^A\right) \tag{4.10}$$

Finally, utilizing the pixel-level fluorescence intensities, we estimated the apparent FRET efficiency for each simulated pixel. We use eq. 4.1 to estimate simulated FRET efficiency for the single-wavelength excitation (E_{single}^{simu}) method and eq. 4.2 to estimate simulated FRET efficiency for the dual-wavelength excitation (E_{dual}^{simu}) method. After calculating the FRET efficiency in each pixel of the simulated camera array using eq. 4.1, we constructed a histogram of E_{single}^{simu} values, and extracted the peak of this histogram. We also computed the average E_{dual}^{simu} value over the array of pixels using equation 4.2.

As stated above, we employed a 3D array of donor and acceptor photo-bleaching probabilities. Each point in the 3D array contained a unique combination of $P_{\lambda 1}^{D}$, $P_{\lambda 1}^{A}$, and $P_{\lambda 2}^{A}$. A separate numerical simulation was performed for each point in the 3D array of photo-bleaching probabilities. Furthermore, to reduce potential errors, we repeated the simulation 20 times for each set of photo-bleaching probabilities. For the dual-wavelength method, the value of E_{dual}^{simu} is estimated from the average of the FRET efficiencies obtained from all 20 repetitions. Whereas for single-wavelength method, the dominant peak of histogram from each repetition was extracted and used to create a "meta-histogram" of the dominant peak positions using a bin size of 0.01, similar to what was performed for the measured FRET efficiency values obtained using the single-wavelength method (described previously in the section 4.2.4.2). Ultimately, for a single set of photobleaching probabilities, we obtained an average simulated FRET efficiency for both excitation methods, single- and dual-wavelength excitation. This array of simulations was performed for all the FRET constructs, i.e., NDA, ADN, and ADA.

Once the simulated FRET efficiencies were estimated for all three FRET constructs, the predicted FRET efficiency (E_{pred}^{simu}) for the trimeric construct was also estimated utilizing simulated FRET efficiencies of dimeric constructs ADN and NDA. Thereafter, the discrepancy $\Delta E_{ADA} = E^{simu} - E_{pred}^{simu}$ was determined for the trimeric construct, similar to what we have done for the measured data.

We found a high fitting error when calculating the residual by comparing individual construct's measured and simulated FRET efficiencies. Thus, we fixed the photobleaching probabilities of donor and acceptor to the same values across both dimeric (NDA and ADN) and trimeric construct (ADA) to estimate the simulated FRET efficiencies. This was achieved by comparing the simulated FRET efficiencies of all the constructs for each set of bleaching

probabilities with those measured experimentally, by computing fitting residuals using following equation:

$$Residueal = \left[\sum_i \left(E^i_{meas,single} - E^i_{simul,single}\right)^2 + \sum_i \left(E^i_{meas,dual} - E^i_{simul,dual}\right)^2\right]^2 \quad (4.11)$$

where i is a summation index that stands for the constructs "NDA," "ADN," and "ADA," $E^i_{meas,single}$ and $E^i_{simul,single}$ are FRET efficiencies measured using the single-wavelength protocol and simulated, respectively, for each construct, while $E^i_{meas,dual}$ and $E^i_{simul,dual}$ are FRET efficiencies measured using the dual-wavelength excitation protocol and, respectively, simulated for each construct. The input photobleaching parameters were varied from 0 to 1 in steps of 0.5, as illustrated in Figs. 4.2 and 4.3. The photobleaching probabilities of D and A for a particular excitation power and excitation wavelength pair were determined based on the set of photobleaching probabilities corresponding to the lowest overall residual.

4.3. Results

4.3.1. Validation of the experimental and data analysis protocols under low excitation power

The overall goal of this study is to evaluate the impact of the excitation conditions on the photobleaching of FRET donors and acceptors and how photobleaching affects the accuracy of the results. To do this, we took advantage of important tools available to us, including: (1) Pulsed excitation light (see Methods) to avoid errors caused by the acceptors and donors being simultaneously in an excited state and therefore unable to be involved in FRET (see

Introduction). (2) A trimeric acceptor-donor-acceptor (ADA) construct that presents a high FRET efficiency that is relatively easy to determine with high accuracy, and two additional dimeric constructs, NDA and ADN (where N is a dark place holder) whose FRET efficiencies are used to predict (for comparison to experiment) the FRET efficiency of the ADA construct. (3) An optical microspectroscope with high signal-to-noise ratio, which allows us to accurately determine FRET efficiencies at low as well as high excitation powers, i.e., in the presence or absence of photobleaching, respectively.

Two methods have been used in the past to determine the FRET efficiency of oligomeric constructs: single and dual-wavelength excitation schemes. In the first approach, the FRET efficiency is determines using only one excitation wavelength that excites the donor significantly while exciting the acceptor only minimally [66, 80]. This method simplifies the process and avoids calibration errors that could be caused by an additional scan of the sample. The dual-excitation method, on the other hand, involves scanning the sample at two different wavelengths. The second excitation scan allows for both the correction of the contribution to FRET of the unintended direct excitation of the acceptor at the first excitation wavelength and the estimation of the concentration of donors and acceptors [10, 80]. In this section we compare the accuracy of these two methods using the lowest excitation power we could achieve without compromising the signal to noise levels.

For the single-wavelength excitation method, we tuned the center wavelength of the laser pulses to 800 nm. This wavelength is known to induce appreciable two-photon excitation of Cerulean but negligible excitation of Venus fluorescent proteins [14]. Typical results for the trimeric construct ADA expressed in the cytoplasm of CHO cells are illustrated in Fig. 4.4. After spectrally unmixing the composite microspectroscopic images of the samples (Fig. 4.4a

and b), the FRET efficiency was computed using Eq. (4.1) for every pixel to generate two-dimensional FRET efficiency maps (Fig. 4.4c) on which regions of interest (ROI) were manually drawn and divided into smaller segments (Fig. 4.4c) as described in Materials and Methods. A histogram was then generated from the E_{app} values of all pixels within a particular segment (Fig. 4.4d). Finally, the peak positions of each E_{app} histogram were collected and used to generate a final distribution of the frequency of occurrence of each peak value, i.e., a meta-histogram of E_{app} (Fig. 4.4a). The process was repeated for each FRET construct for all the cell samples investigated. From the peak position (i.e., mode) of each meta-histogram (Fig. 4.4e), the weighted average $E_{single}^{meas} \pm \mathrm{SD_w}$ was computed for all the ROIs for each construct using each chosen excitation power.

Average FRET efficiencies obtained in the case of single excitation wavelength (at for each of the three FRET constructs at the lowest excitation power used in this work (15 mW per point) are listed in Table 4.1, and all four excitation powers in Tables 4.5-4.7. As we it will become apparent momentarily, the FRET efficiencies obtained for the 15 mW laser power provide good reference points for the subsequent assays, in that they are minimally affected by photobleaching. We note for now that difference between the FRET efficiency value measured for the ADA fusion protein stands in good agreement with the one computed, or "predicted," from measurements of the NDA and ADN constructs using a relationship obtained from the kinetic theory of FRET (see Ref. [88] and Materials and Methods section 4.2). The overall difference is 0.027 or about 3.5%, which is within the standard deviation for these measurements.

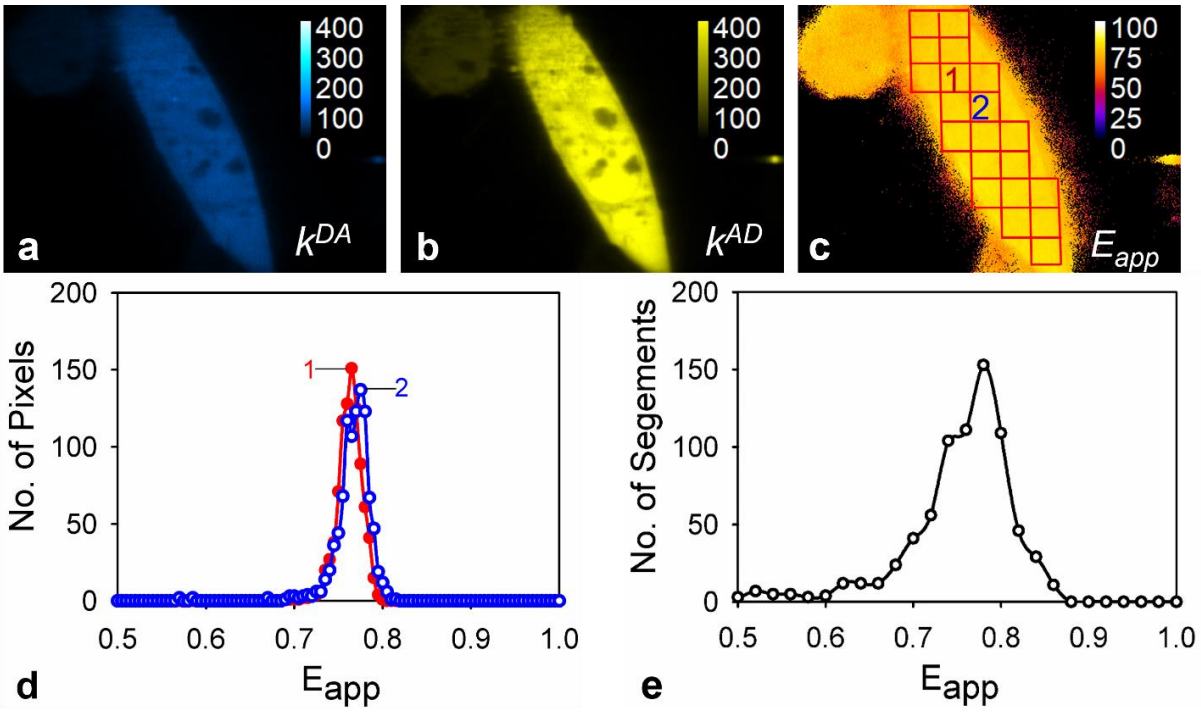

Figure 4.4. Typical result obtained from imaging CHO cells co-expressing cytoplasmic FRET constructs using two-photon excitation at 800 nm. Unmixing of the original fluorescence micro-spectrographs resulted into two-dimensional intensity maps were generated for the signal of (a) donors in the presence of acceptors, k^{DA}, and (b) acceptors in the presence of donors, k^{AD}. Apparent FRET efficiency, E_{app}, maps (c) were computed from the pixel-level values of k^{AD} and k^{DA}. Hand-drawn regions of interest for the E_{app}, maps are divided into smaller segments (red squares) using the *moving-squares* method (see Materials and Methods). Panel (d) shows individual E_{app} histograms generated (using a bin size of 0.005) for the randomly selected segments labeled with 1 (red line, filled circles) and 2 (blue line, empty circles) in c. A meta-histogram (e) obtained for the FRET construct ADA from a typical experimental dataset (~ 20 images) was generated by combining the peak positions of individual E_{app} histograms generated from each ROI segment of all the cells imaged expressing this construct.

Table 4.1. Apparent FRET efficiencies (weighted averages ± weighted standard deviation, SD_w or propagated error, δ) for cytoplasmic FRET constructs using single-wavelength excitation at 800 nm and average laser power of 15 mW/point (energy, 0.38 μJ per pixel). The total error computed by adding individual errors in quadrature is shown in parentheses.

Constructs	Apparent FRET efficiencies		
	$E_{single} \pm SD_w$	$E_{ADA}^{pred} \pm \delta E_{ADA}^{pred}$	$\Delta E_{ADA} \pm \delta \Delta E_{ADA}$
NDA	0.581 ± 0.023	—	—
ADN	0.628 ± 0.022	—	—
ADA	0.781 ± 0.040	0.754 ± 0.017	0.027 ± 0.057 (0.043)

We also computed the average FRET efficiency for each of the three constructs using Eq. 4.2, which incorporates measurements from a second excitation wavelength in the calculation. To compare the effect of photobleaching induced at different excitation wavelengths, we performed separate experiments using three pairs of excitation wavelengths: 800 nm/880 nm, 800 nm/960 nm, and 880nm/960 nm. The results obtained from all three pairs of excitation wavelengths at the lowest excitation power (of 15 mW/point) are summarized in Table 4.2. In this case, the differences between the FRET efficiency values measured for the ADA fusion protein and the ones computed, or "predicted," from measurements of the NDA and ADN constructs were even smaller than reported above (i.e., 1.9%, 1.5%, and 2.4%, for the 800 nm/880 nm, 800 nm/960 nm, and 880nm/960 nm wavelength pairs, respectively) and well within the calculated error for these quantities.

Table 4.2. Apparent FRET efficiencies (weighted averages ± weighted standard deviation, SD_w, or propagated error, δ) for cytoplasmic FRET constructs measured using the two-wavelength excitation protocol for three different pairs of wavelengths average laser powers of 15 mW/point (energy, 0.38 μJ per pixel) for all the excitation wavelengths used. Total error computed by adding individual errors in quadrature is given in parentheses.

Constructs	Wavelength pairs (nm/nm)	Apparent FRET efficiencies		
		E_{dual}± SD_w	E_{ADA}^{pred} ± δE_{ADA}^{pred}	ΔE_{ADA}± $\delta\Delta E_{ADA}$
NDA	800/880	0.539 ± 0.022	—	—
	800/960	0.532 ± 0.020	—	—
	880/960	0.530 ± 0.023	—	—
ADN	800/880	0.606 ± 0.021	—	—
	800/960	0.594 ± 0.019	—	—
	880/960	0.592 ± 0.017	—	—
ADA	800/880	0.744 ± 0.014	0.730 ± 0.017	0.014 ± 0.031 (0.022)
	800/960	0.733 ± 0.014	0.722 ± 0.016	0.011 ± 0.030 (0.021)
	880/960	0.739 ± 0.019	0.721 ± 0.016	0.018 ± 0.035 (0.025)

By comparing the results shown in Table 4.2 to those shown in Table 4.1, it becomes evident that the FRET efficiencies extracted from the single-wavelength excitation method were consistently higher (by 5% or more) than those obtained from the dual-wavelength excitation scheme, for all the constructs investigated. These differences originated from an overestimation of the E_{single}^{meas}, due to weak by non-negligible direct excitation of the acceptors at 800 nm, which is not accounted for in Eq. 4.1 but is included in Eq. 4.2 through the quantity $\rho^{ex,A}$ (see Table 4.3).

Table 4.3. The intensity ratio of the donors ($\rho^{ex,D}$) and acceptors ($\rho^{ex,A}$) between two excitation wavelengths at various excitation powers. The measurements were performed for three different excitation wavelength pairs: 800 nm/880 nm, 800 nm/960 nm, and 880 nm/960 nm and four different excitation powers: 15 mW/point (corresponding to an excitation energy 0.38 μJ per pixel), 42 mW/point (energy, 1.07 μJ per pixel), 52 mW/point (energy, 1.32 μJ per pixel), and 62 mW/point (energy,1.58 μJ per pixel).

Ex. Wavelengths	Coefficient	15 mW/point	42 mW/point	52 mW/point	62 mW/point
800 nm /880 nm	$\rho^{ex,D}$	0.46	0.55	0.60	0.61
	$\rho^{ex,A}$	0.1	0.14	0.15	0.20
800 nm /960 nm	$\rho^{ex,D}$	11.45	8.33	8.37	7.17
	$\rho^{ex,A}$	0.05	0.05	0.07	0.08
880 nm /960 nm	$\rho^{ex,D}$	23.91	19.06	17.14	13.73
	$\rho^{ex,A}$	0.37	0.42	0.43	0.46

Table 4.4. The input FRET efficiencies for numerical simulation. These values are weighted average FRET efficiencies across all excitation pairs at power 15 mW/point (energy, of 0.38 μJ per pixel).

Constructs	Avg. E_{dual} of all ex. pairs at 15 mW/point
NDA	0.534
NDA	0.597
ADA	0.739

Table 4.5. Weighted average of apparent FRET efficiencies ± SE of all datasets obtained for each FRET construct measured using both single and dual excitation methods for the experiments carried out at 800 and 880 nm. The following average excitation powers per point were used: 15 mW (energy, 0.38 μJ per pixel), 42 mW (energy, 1.07 μJ per pixel), 52 mW (energy, 1.32 μJ per pixel), and 62 mW (energy,1.58 μJ per pixel). Total error computed by adding individual errors in quadrature is given in parentheses.

Power (mW)	Constructs	Excitation Wavelength (nm)	Apparent FRET efficiencies		
			E_{meas}± SD_w	E_{pred}± δE_{pred}	ΔE_{meas} ± $\delta\Delta E$
15	NDA	800	0.556 ± 0.023	—	—
		800/880	0.539 ± 0.022	—	—
	ADN	800	0.631 ± 0.021	—	—
		800/880	0.606 ± 0.021	—	—
	ADA	800	0.778 ± 0.026	0.748 ± 0.017	0.030 ± 0.043 (0.031)
		800/880	0.744 ± 0.014	0.730 ± 0.017	0.014 ± 0.031 (0.022)
42	NDA	800	0.568 ± 0.019	—	—
		800/880	0.504 ± 0.020	—	—
	ADN	800	0.629 ± 0.020	—	—
		800/880	0.571 ± 0.020	—	—
	ADA	800	0.773 ± 0.026	0.751 ± 0.015	0.022±0.041 (0.030)
		800/880	0.696 ± 0.022	0.701 ± 0.017	-0.005±0.039 (0.028)
52	NDA	800	0.549 ± 0.029	—	—
		800/880	0.471 ± 0.027	—	—
	ADN	800	0.635 ± 0.020	—	—
		800/880	0.550 ± 0.018	—	—
	ADA	800	0.786 ± 0.025	0.747 ± 0.019	0.039±0.044 (0.031)
		800/880	0.704 ± 0.022	0.679 ± 0.019	0.025 ± 0.041 (0.029)
62	NDA	800	0.554 ± 0.026	—	—
		800/880	0.452 ± 0.033	—	—
	ADN	800	0.637 ± 0.021	—	—
		800/880	0.517 ± 0.024	—	—
	ADA	800	0.776 ± 0.028	0.750 ± 0.018	0.026 ± 0.046 (0.033)
		800/880	0.665 ± 0.035	0.655 ± 0.025	0.010 ± 0.060 (0.043)

Table 4.6. Weighted average of apparent FRET efficiencies ± SE of all datasets obtained for each FRET construct measured using both single and dual excitation methods for the experiments carried out at 800 and 960 nm. The following average excitation powers per point were used: 15 mW (energy, 0.38 μJ per pixel), 42 mW (energy, 1.07 μJ per pixel), 52 mW (energy, 1.32 μJ per pixel), and 62 mW (energy,1.58 μJ per pixel). Total error computed by adding individual errors in quadrature is given in parentheses.

Power (mW)	Constructs	Excitation Wavelength (nm)	Apparent FRET efficiencies		
			E_{meas}± SD_w	E_{pred}± δE_{pred}	ΔE_{meas} ± $\delta\Delta E$
15	NDA	800	0.575 ± 0.021	—	—
		800/960	0.532 ± 0.020	—	—
	ADN	800	0.615± 0.017	—	—
		800/960	0.594 ± 0.019	—	—
	ADA	800	0.779 ± 0.048	0.747 ± 0.015	0.032 ± 0.063 (0.050)
		800/960	0.733 ± 0.014	0.722 ± 0.016	0.011 ± 0.030 (0.021)
42	NDA	800	0.575 ± 0.020	—	—
		800/960	0.503 ± 0.019	—	—
	ADN	800	0.629 ± 0.017	—	—
		800/960	0.577 ± 0.016	—	—
	ADA	800	0.781 ± 0.035	0.753 ± 0.014	0.028 ± 0.049 (0.038)
		800/960	0.715 ± 0.018	0.704 ± 0.015	0.011 ± 0.033 (0.023)
52	NDA	800	0.583 ± 0.026	—	—
		800/960	0.470 ± 0.027	—	—
	ADN	800	0.646 ± 0.018	—	—
		800/960	0.556 ± 0.021	—	—
	ADA	800	0.764 ± 0.023	0.763 ± 0.016	0.001 ± 0.039 (0.028)
		800/960	0.671 ± 0.021	0.681 ± 0.021	-0.010 ± 0.042 (0.029)
62	NDA	800	0.557 ± 0.024	—	—
		800/960	0.428 ± 0.027	—	—
	ADN	800	0.623 ± 0.020	—	—
		800/960	0.513 ± 0.024	—	—
	ADA	800	0.763 ± 0.030	0.744 ± 0.017	0.019 ± 0.047 (0.035)
		800/960	0.643 ± 0.035	0.643 ± 0.023	-0.000 ± 0.058 (0.042)

Table 4.7. Weighted average of apparent FRET efficiencies ± SE of all datasets obtained for each FRET construct measured using both single and dual excitation methods for the experiments carried out at 880 and 960 nm. The following average excitation powers per point were used: 15 mW (energy, 0.38 μJ per pixel), 42 mW (energy, 1.07 μJ per pixel), 52 mW (energy, 1.32 μJ per pixel), and 62 mW (energy,1.58 μJ per pixel). Total error computed by adding individual errors in quadrature is given in parentheses.

Power (mW)	Constructs	Excitation Wavelength (nm)	Apparent FRET efficiencies		
			E_{meas}± SD_w	E_{pred}± δE_{pred}	ΔE_{meas} ± $\delta\Delta E$
15	NDA	880	0.649 ± 0.019	—	—
		880/960	0.530 ± 0.023	—	—
	ADN	880	0.628 ± 0.022	—	—
		880/960	0.592 ± 0.017	—	—
	ADA	880	0.781 ± 0.040	0.754 ± 0.017	0.027 ± 0.057 (0.043)
		880/960	0.739 ± 0.019	0.721 ± 0.016	0.018 ± 0.035 (0.025)
42	NDA	880	0.677 ± 0.017	—	—
		880/960	0.477 ± 0.023	—	—
	ADN	880	0.713 ± 0.015	—	—
		880/960	0.565 ± 0.020	—	—
	ADA	880	0.839 ± 0.019	0.821 ± 0.011	0.018 ± 0.030 (0.022)
		880/960	0.683 ± 0.026	0.688 ± 0.018	-0.005 ± 0.044 (0.032)
52	NDA	880	0.670 ± 0.020	—	—
		880/960	0.460 ± 0.026	—	—
	ADN	880	0.732 ± 0.016	—	—
		880/960	0.536 ± 0.021	—	—
	ADA	880	0.849 ± 0.019	0.826 ± 0.012	0.022 ± 0.031 (0.022)
		880/960	0.658 ± 0.027	0.667 ± 0.021	-0.010 ± 0.048 (0.034)
62	NDA	880	0.680 ± 0.019	—	—
		880/960	0.436 ± 0.030	—	—
	ADN	880	0.716 ± 0.014	—	—
		880/960	0.513 ± 0.024	—	—
	ADA	880	0.850 ± 0.020	0.823 ± 0.011	0.027 ± 0.031 (0.023)
		880/960	0.645 ± 0.033	0.646 ± 0.024	-0.001 ± 0.057 (0.041)

Overall, the above observations support the notion that the use of the second excitation wavelength is warranted and confirm the validity of measurement method based on two excitation wavelengths.

4.3.2. Effect of higher excitation power on FRET efficiency

Having established the accuracy of the method in the absence of significant photobleaching of the donors or acceptors, we next wanted to use it to explore the effect on the FRET efficiency values of increased excitation power and, hence, the likelihood that the molecules are photobleached. We performed measurements using three additional excitation powers (42 mW/point, 52 mW/point, and 62 mW/point) for both the single and the dual-wavelength excitation schemes. The measured FRET efficiency values of the ADA construct for all excitation wavelength pairs, presented in Fig. 4.5, decreased significantly with increasing the excitation power, due to photobleaching of either the donor or the acceptor. (The specific degree of photobleaching of the donors and acceptors has been assessed using computer simulations and will be discussed in the next section.) By contrast, the gray solid circles representing FRET efficiencies for single-excitation at 800 nm only show no significant effect of the increased power on FRET. The results for the other two FRET constructs (ADN and NDA), shown in Tables 4.5-4.7, showed similar behavior for all the excitation wavelengths used. These changes suggest that the acceptors were photobleached during the measurement process through direct excitation, energy transfer, or both.

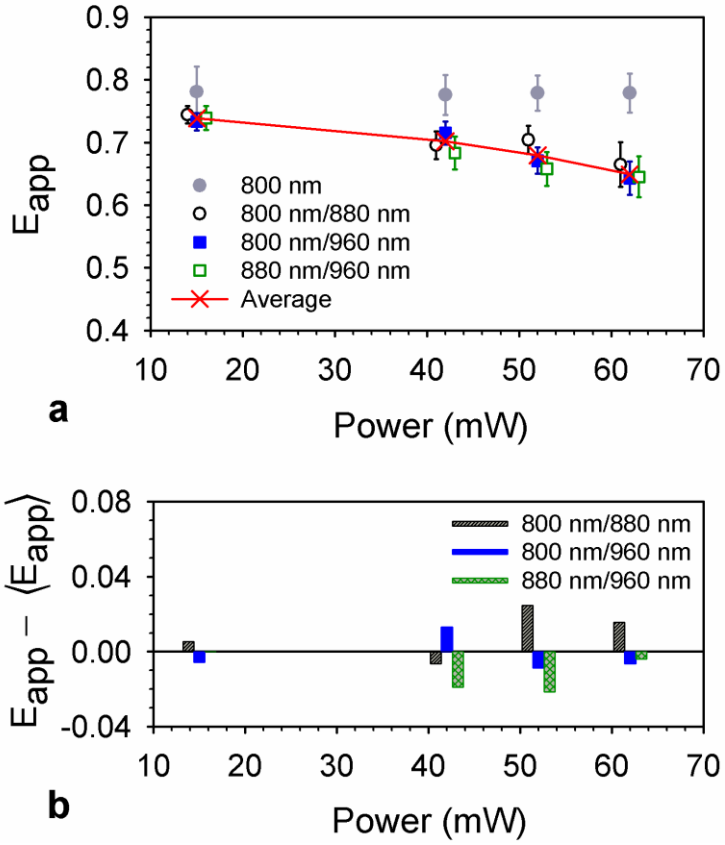

Figure 4.5. Apparent FRET efficiencies (E_{app}) obtained using single- and dual-wavelength excitation methods at various powers for the cytoplasmic FRET construct, ADA. The experiments involved four excitation schemes; single-wavelength excitation at 800 nm, and dual-wavelength excitation at three pairs of wavelengths: 800 nm/880 nm, 800 nm/960 nm, and 880 nm/960 nm. (a) The measured FRET efficiencies using various schemes of excitation, gray solid circles represent the FRET efficiencies for single-wavelength excitation at 800 nm, black empty circles represent the FRET efficiencies excitation pair 800 nm/880 nm, blue solid squares represent for excitation pair 800 nm/960 nm, green empty squares represent for excitation pair 880 nm/960 nm, and the red symbols × with red line represent the weighted average FRET efficiencies across all three pairs of excitation wavelength utilizing dual-wavelength excitation method. The FRET efficiency for each excitation scheme was estimated from the weighted average FRET efficiencies of four or five different experiments obtained for that scheme at a distinct power. (b) Difference between FRET efficiencies of individual excitation pair and the weighted average FRET efficiencies across all excitation pairs. Black striped bars, blue solid bars, and green hatched bars represent the variance of FRET efficiency for excitation pairs 800 nm/880 nm, 800 nm/960 nm, and 880 nm/960 nm, respectively, from their combined weighted average indicated by the red dashed symbols in a. To enhance the legibility of the results, symbols for some measurement schemes were slightly shifted to the right or to the left of the actual power point marked by the red symbol ×.

Interestingly, analysis of the data in Table 4.5-4.7 suggests that there is virtually no effect of the excitation power on the discrepancy between the measured (i.e., E_{ADA}) and predicted (E_{ADA}^{pred}) FRET efficiency for both excitation methods. In addition, for the dual-wavelength excitation method, the rate of FRET efficiency decrease with the increase in excitation power was similar for both the dimeric (NDA and ADN) and the trimeric (ADA) constructs (see Table 2 and Tables 4.5-4.7). This is because, although currently the kinetic theory of FRET does not incorporate photobleaching effects, its contribution to dimeric FRET efficiencies is simply transferred to the FRET efficiency of the trimeric construct via the mathematical formula used (see section 4.2.5 and Ref [88]).

Also quite remarkably, for the single-wavelength excitation method using 800 nm laser light, the FRET efficiency remained the same for both the dimeric and the trimeric constructs across all four powers, although we have established that photobleaching must have occurred. By contrast, when the single excitation wavelength was 880 nm, the single-wavelength excitation method produced FRET efficiencies that increased with the average excitation power (see Table 4.7). We hypothesize that these changes were caused by generation of acceptor-only complexes via photobleaching of donors, which were directly excited to a modest but significant degree (see above) by the laser light at 800 nm, and to a higher degree when the single excitation wavelength was 880 nm. The additional acceptor signal produced by those acceptors was the inadvertently taken as contributing to the emission caused by excitation via FRET, therefore compensating for the loss of signal due to photobleaching of acceptors residing within complexes with fluorescently active donors.

We will provide a more quantitative analysis of all the above observations in the next section.

4.3.3. Modeling the power dependence of the FRET efficiency using numerical simulation

To model the dependence of the measured FRET efficiency on the average excitation power (see Fig. 4.5), we performed numerical simulations to compute pixel-level FRET efficiencies for a population of FRET constructs residing at each pixel, which used a range of different photobleaching probabilities. The photobleaching probabilities represent the likelihood of a single fluorophore in the simulation transitioning from an active to a dark state for each excitation wavelength. The resultant FRET efficiency of the population of constructs residing at a pixel was recorded for each different set of photobleaching probabilities and compared to the actual measured FRET efficiency for the construct, using a fitting residual defined as the sum of the squares of the differences between measured and simulated FRET efficiencies (see Eq. 4.11).

We generated three-dimensional plots with the three photobleaching probabilities (corresponding to D photobleaching during the first scan, A photobleaching during the first scan, and A photobleaching during the second scan) on the three axes and the fitting residual represented via a color code as the fourth dimension. Individual plots are displayed in Fig. 4.6 for three different sets of experimental powers (42 mW, 52 mW, and 62 mW) obtained for dual excitation at 800 nm and 960 nm (additional fitting residual distributions generated for 800/880 nm and 880/960 nm wavelength pairs are displayed in Fig. 4.7 and Fig. 4.8. The lowest residual values correspond to the dark blue or black regions of the plots (see scale bar inset of Fig. 4.6). Fig. 4.9 compares the best-fit simulated FRET efficiencies, which incorporate the possibility of both D and A undergoing photobleaching at different probabilities, with the experimentally obtained values for each excitation power using the excitation wavelength pair of 800nm and

960nm (equivalent plots generated for 800/880 nm and 880/960 nm wavelength pairs are displayed in Fig. 4.10 and Fig. 4.11. The results showed a good agreement between simulations and experiments, indicating that the change in FRET efficiencies is explained well by differing photobleaching levels of D and A, which are collected in Table 4.8.

Inspection of the photobleaching values in Table 4.8 indicates wide variability between different and even the same experimental conditions (such as the same λ_2), due to the fact that the donor photobleaching at the second wavelength only affected an already small correction term in Eq. (4.2). Therefore, this minor effect is not discussed any further.

Overall, our simulations revealed a clear pattern of increasing photobleaching probability of both donor during the first scan at higher power, with donors exhibiting a wider range of photobleaching probabilities depending on the excitation power (see Table 4.8).

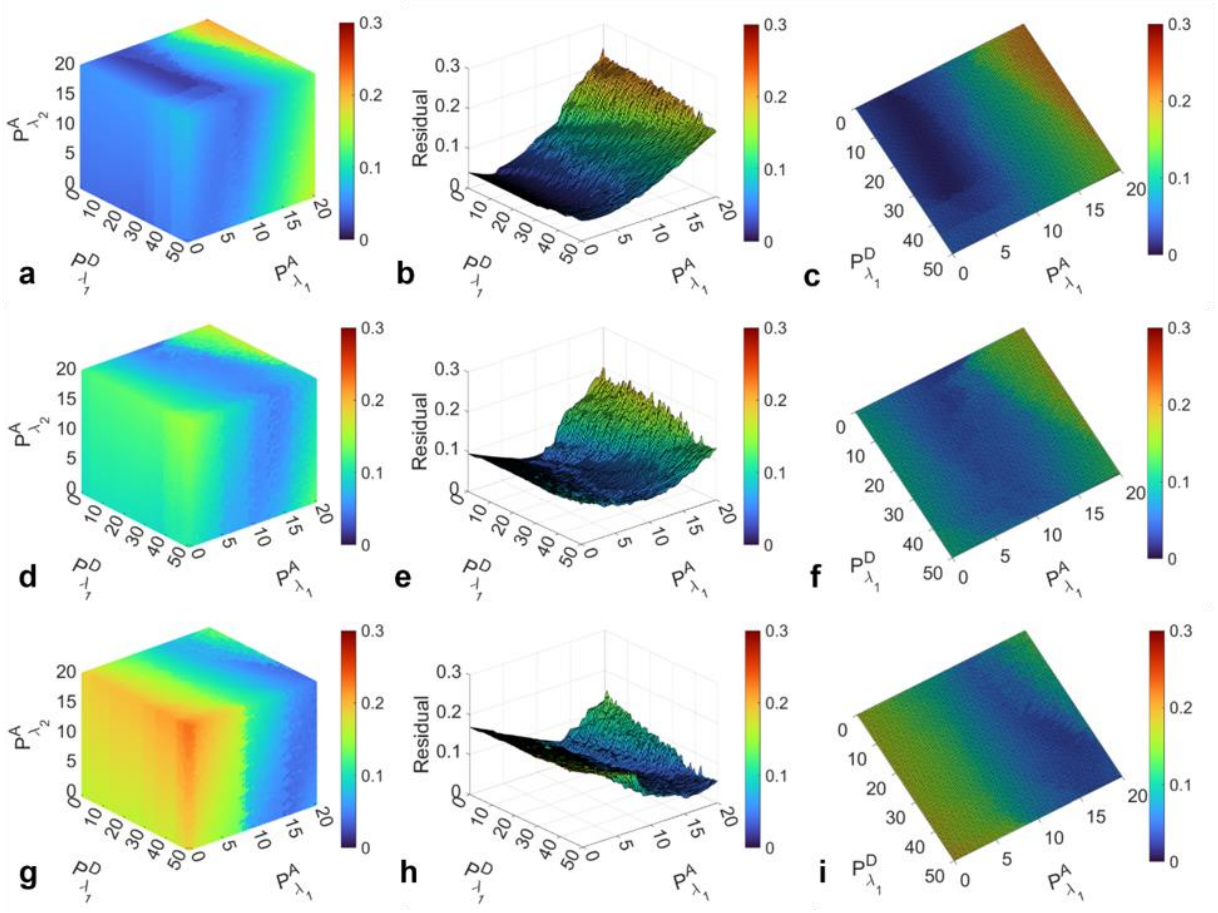

Figure 4.6. Distribution of fitting residual as a function of photobleaching probabilities, calculated comparing simulated and measured FRET efficiencies of all three constructs under 800 nm/960 nm excitation for three different excitation powers. (a) 3D residual map that show probability of donor bleaching at the first wavelength along x-axis, the probability of acceptor bleaching at the first wavelength along y-axis, and the probability of acceptor bleaching at a second wavelength along z-axis, with color gradients indicating the magnitude of residuals. (b) The modified version of panel a by substituting the vertical axis with residual values, offering a refined analysis of residual distribution keeping the probability of acceptor bleaching at second wavelength fixed corresponding to minimum residual. (c) Top view of panel b, highlighting residual distribution in 2D map. The figure is organized into rows corresponding to different excitation powers: the top row (a-c) for excitation power 42 mW/point, the middle row (d-f) for 52 mW/point, and the bottom row (g-i) for 62 mW/point, showcasing how variations in excitation power influence the photobleaching dynamics and FRET efficiency residuals.

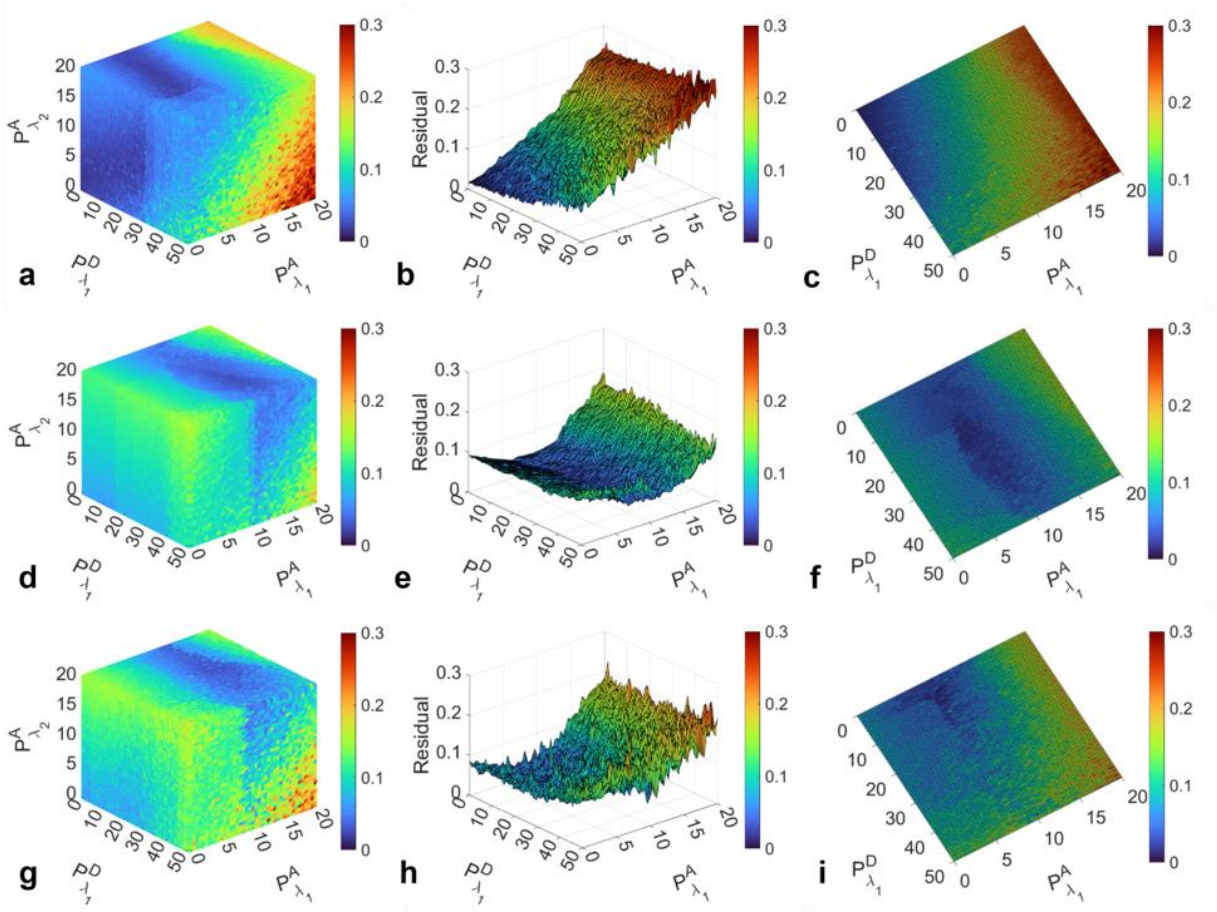

Figure 4.7. Distribution of fitting residual as a function of photobleaching probabilities, calculated comparing simulated and measured FRET efficiencies of all three constructs under 800 nm/880 nm excitation for three different excitation powers. (a) 3D residual map that show probability of donor bleaching at the first wavelength along x-axis, the probability of acceptor bleaching at the first wavelength along y-axis, and the probability of acceptor bleaching at a second wavelength along z-axis, with color gradients indicating the magnitude of residuals. **(b)** The modifies version of panel a by substituting the vertical axis with residual values, offering a refined analysis of residual distribution keeping the probability of acceptor bleaching at second wavelength fixed corresponding to minimum residual. **(c)** Top view of panel b, highlighting residual distribution in 2D map. The figure is organized into rows corresponding to different excitation powers: the top row **(a-c)** for excitation power 42 mW/point (corresponding to an excitation energy of 0.38 μJ per pixel), the middle row **(d-f)** for 52 mW/point (corresponding to an excitation energy of 1.07 μJ per pixel), and the bottom row **(g-i)** for 62 mW/point (corresponding to an excitation energy of 1.58 μJ per pixel), showcasing how variations in excitation power influence the photobleaching dynamics and FRET efficiency residuals.

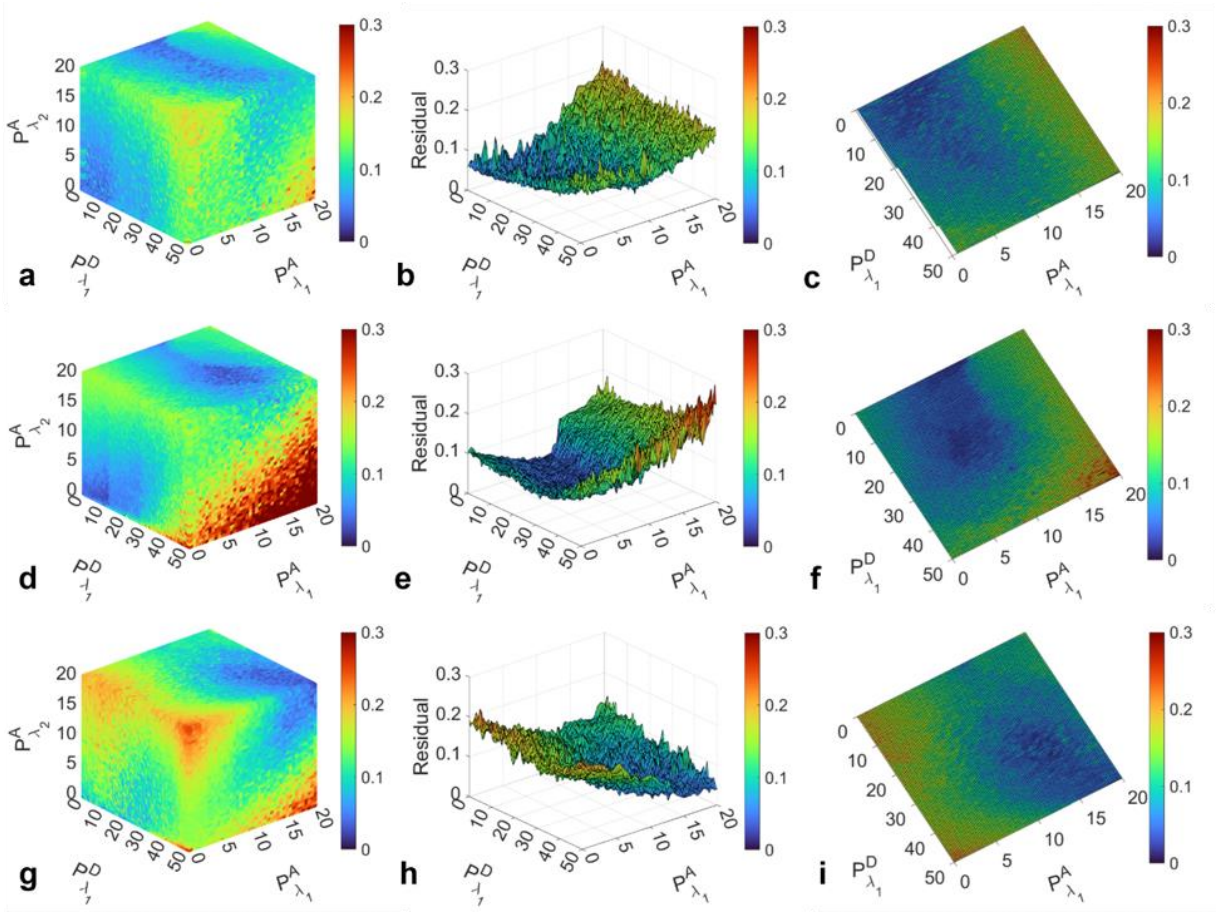

Figure 4.8. Distribution of fitting residual as a function of photobleaching probabilities, calculated comparing simulated and measured FRET efficiencies of all three constructs under 880 nm/960 nm excitation for three different excitation powers. (a) 3D residual map that show probability of donor bleaching at the first wavelength along x-axis, the probability of acceptor bleaching at the first wavelength along y-axis, and the probability of acceptor bleaching at a second wavelength along z-axis, with color gradients indicating the magnitude of residuals. **(b)** The modifies version of panel a by substituting the vertical axis with residual values, offering a refined analysis of variance between measured and simulated data keeping the probability of acceptor bleaching at second wavelength fixed corresponding to minimum residual. **(c)** Top view of panel b, highlighting residual distribution in 2D map. The figure is organized into rows corresponding to different excitation powers: the top row **(a-c)** for excitation power 42 mW/point (corresponding to an excitation energy of 0.38 μJ per pixel), the middle row **(d-f)** for 52 mW/point (corresponding to an excitation energy of 1.07 μJ per pixel), and the bottom row **(g-i)** for 62 mW/point (corresponding to an excitation energy of 1.58 μJ per pixel), showcasing how variations in excitation power influence the photobleaching dynamics and FRET efficiency residuals.

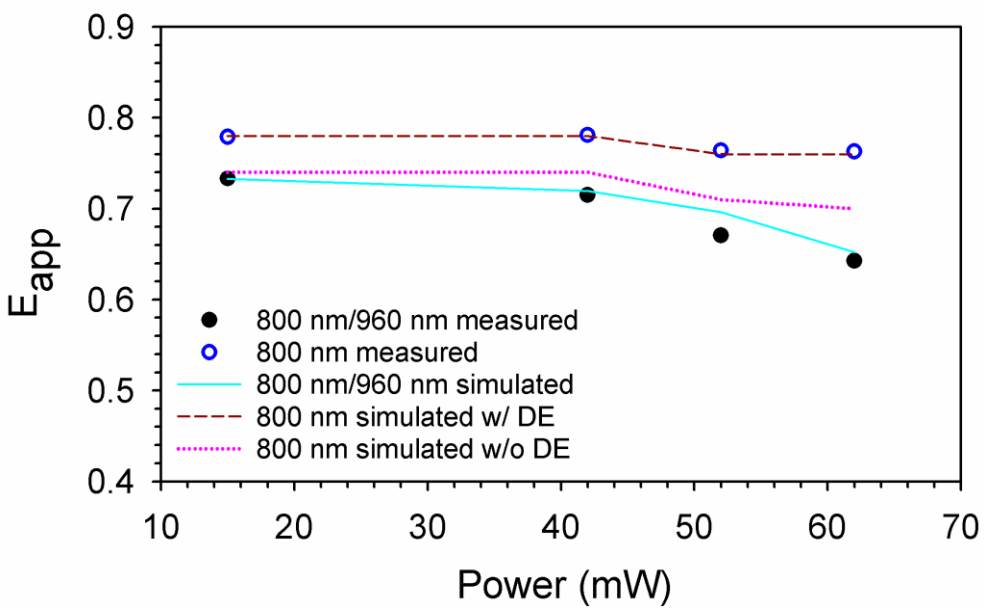

Figure 4.9. Comparison of measured and simulated FRET efficiencies (E_{app}) for the cytoplasmic FRET construct, ADA, obtained using 800 nm/960 nm at various excitation powers per point. The black solid circles represent the measured FRET efficiencies using dual-wavelength excitation method with 800 nm/960 nm. Blue empty circles represent the measured FRET efficiencies for single-wavelength excitation at 800 nm. Whereas, cyan solid line represents the simulated FRET efficiencies curve for excitation pair 800 nm/960 nm. Dark red dashed line represents the simulated FRET efficiencies using single excitation at 800 nm with (w/) direct excitation (De) of acceptor. Pink dotted line represents the simulated FRET efficiencies using single excitation at 800 nm without (w/o) direct excitation of acceptor.

This analysis explained a second key trend observed in our experimental data, that the FRET efficiency values obtained from the single-wavelength excitation method remained constant regardless of excitation power. While this trend might initially suggest that the single-wavelength FRET values are impervious to photobleaching, a closer examination of the data shown in Fig. 4.9 reveals otherwise: Fig. 4.9 also displays the best-fit simulated FRET efficiency values obtained using the single-wavelength approach, with the contribution from acceptor direct excitation (DE) subtracted and plotted as a pink dotted line. This curve does

indicate a monotonous decrease in E_{app} with increase in excitation power, which parallels the results of the dual-excitation scheme (compare the pink dotted line to the solid cyan line).

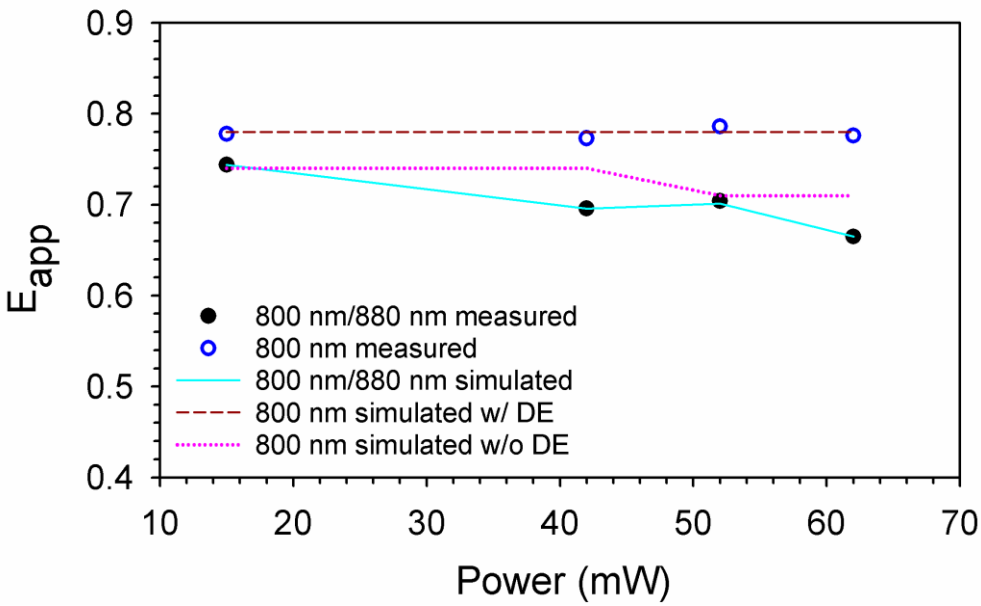

Figure 4.10. Comparison of measured and simulated FRET efficiencies (E_{app}) for the cytoplasmic FRET construct, ADA, obtained using 800 nm and 880 nm at various excitation powers per point. The black solid circles represent the weighted average FRET efficiencies across all measurements performed using dual-wavelengths excitation method at 800 nm and 880 nm. Blue empty circles represent the weighted averaged FRET efficiencies across all the measurements for single-wavelength excitation at 800 nm. The cyan solid line represents the best-fit simulated FRET efficiencies for the excitation pair 800 nm/880 nm. Dark red dashed line represents the simulated FRET efficiencies using single excitation at 800 nm with (w/) direct excitation (De) of acceptor. Pink dotted line represents the simulated FRET efficiencies using single excitation at 800 nm without (w/o) direct excitation of acceptor.

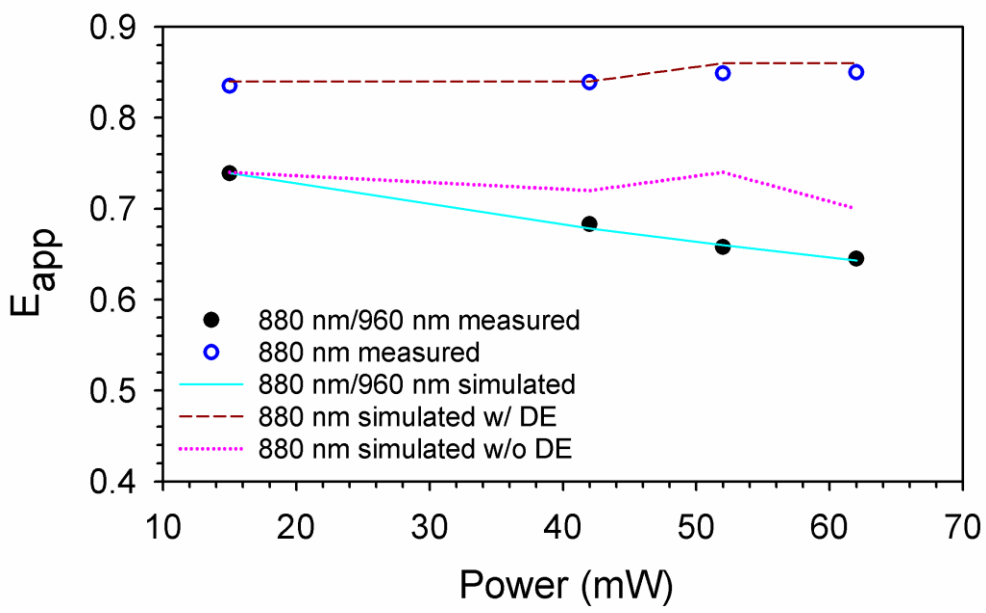

Figure 4.11. Comparison of measured and simulated FRET efficiencies (E_{app}) for the cytoplasmic FRET construct, ADA, obtained using 880 nm and 960 nm at various excitation powers per point. The black solid circles represent the weighted average FRET efficiencies across all measurements performed using dual-wavelengths excitation method at 880 nm and 960 nm. Blue empty circles represent the weighted averaged FRET efficiencies across all the measurements for single-wavelength excitation at 880 nm. The cyan solid line represents the best-fit simulated FRET efficiencies for the excitation pair 880 nm/960 nm. Dark red dashed line represents the simulated FRET efficiencies using single excitation at 880 nm with (w/) direct excitation (De) of acceptor. Pink dotted line represents the simulated FRET efficiencies using single excitation at 880 nm without (w/o) direct excitation of acceptor.

The apparent stability of the FRET efficiency across different excitation powers in the single-wavelength excitation method (brown dashed line) is deceiving and can be attributed to a balancing act: Increased excitation power leads to more donor photobleaching, which increases the number of free acceptors by inactivating the donor from the construct. This raises the measured FRET efficiency value due to the direct excitation of free acceptors. However, increased power also causes more acceptor photobleaching due to FRET, which tends to reduce FRET efficiency. Thus, in the single-wavelength excitation method, the increase in E_{app} caused by direct excitation balances out the decrease from acceptor photobleaching, resulting in a stable FRET efficiency across different power levels (see grey solid circles in Fig. 4.5).

Table 4.8. Summary of photobleaching probabilities, based on numerical simulation for three schemes of excitation pairs, at various excitation powers per point. The probabilities were estimated by fitting experimental results with simulated FRET efficiencies.

Ex. Pairs	Power (mW)	$P_{\lambda_1}^{D}$	$P_{\lambda_1}^{A}$	$P_{\lambda_2}^{A}$
800 nm - 880 nm	42	0.0	0.0	1.5
	52	18.0	8.0	9.5
	62	10.5	8.0	4.5
800 nm - 960 nm	42	3.5	4.0	0.0
	52	10.0	9.0	0.0
	62	34.5	16.5	4.5
880 nm - 960 nm	42	2.0	6.5	7.5
	52	24.0	6.0	11.5
	62	39.0	14.0	17.0

In contrast, in the dual-excitation method, corrections were made for the possible overestimation of FRET value caused by the direct excitation of the acceptor. However, acceptor photobleaching at the first excitation wavelength still leads to reduced FRET efficiency as excitation power increases. This is particularly relevant in FRET experiments, as FRET provides an extra pathway for acceptor photobleaching [153, 154].

4.4. Discussion

One of the key findings in this study was the impact of the excitation power on FRET efficiency. With increasing the power, the FRET efficiency steadily decreased across all constructs and when measured and analyzed appropriately. This observation underlined the role of photobleaching in FRET experiments. Our constructs were comprised of the fluorescent proteins Cerulean (donor) and Venus (acceptor). Based on available information, the fluorescent protein Cerulean may be rather easily photobleached under direct excitation by light

[14]. At the same time, while Venus is quite stable under direct excitation by light [14], in our study it was photobleached significantly through excitation by FRET, which is in agreement with the existing literature [153, 154].

The inadvertent decrease in FRET efficiency following excitation with relatively high laser powers (in our case, powers above 42 mW/point) may be erroneously interpreted as a larger distance between donor and acceptor molecules. This may have significant implications for applications where the actual distance between molecules is of interest, such as in studies focused on determination of the quaternary structure of protein oligomers [8, 10, 155]. Fortunately, at comparatively lower excitation powers, such as those corresponding to the first two datapoints in Fig. 4.9, both the single- and the dual-excitation wavelength methods provide results that are accurate within a few percent. To be meticulous, however, the single-wavelength excitation scheme may suffer from small systematic errors caused by the direct excitation of acceptors, which may be reduced by proper choice of acceptors.

Besides using low excitation powers, photobleaching may be reduced by reducing the dwell time of the excitation beam and developing fluorescent tags with better photostability. In addition, the present study also highlighted the importance of selecting the right excitation wavelengths. Excitation at 800 nm minimized direct excitation of the acceptor (Venus) while still efficiently exciting the donor (Cerulean). In contrast, the simulations indicated that the photobleaching of the donor and acceptor was relatively high when using 880 nm as the first excitation wavelength compared to 800 nm. Furthermore, while results from the dual-wavelength excitation method confirmed a consistent trend of decreasing FRET efficiency with higher excitation power across all excitation wavelength pairs, the pair 800 nm/960 nm showed the most consistent overall weighted average FRET efficiency.

Another path forward would be to extend the kinetic theory of FRET, by incorporating photobleaching rates in addition to spontaneous emission and energy transfer rates, so that one can tease apart the contributions of these effects to the FRET efficiencies determined from data affected by photobleaching. Once available, this could be used together with methods described above for reducing photobleaching or just by itself. Such a theoretical undertaking will require a good understanding of all the photophysical and photochemical phenomena involved. This process, initiated through the computer simulations presented in this paper, needs more rigorous treatment in the future and will benefit from analysis of existing [153, 154] and future experimental studies. This will allow experimentalists to use the theory as a means of obtaining correct results from experiments rather than as a toll of assessing the errors introduced by harsh experimental conditions.

Chapter 5. Vista conclusions and suggestions for future research

5.1. Conclusions regarding the photophysical properties of FPs investigations

In chapter 3, we presented a detailed comparative analysis of the photophysical properties of some widely used FPs under two-photon excitation condition. This analysis aimed to establish guidelines for screening FPs as fluorescent tags in various fluorescence applications. For this investigation, we used purified FPs embedded in a polyacrylamide gel. This approach allowed us to scan the same molecules repeatedly several times using the time series excitation. With this, we were able to quantify the fluorescence intensity and monitoring changes in the emission and excitation spectra of an FP occurring during the repeated scans. Specifically, we were able to accurately estimate the level of photobleaching and determine whether a specific FP exhibited photo-switching properties. Furthermore, we estimated the 2p brightness using an excitation wavelength that corresponds to the peak of the FP's excitation spectrum.

Based on these investigations, we concluded that mEGFP is the brightest variant of wtGFP measured in our investigation. It exhibited only moderate photobleaching and no noticeable photo-switching under 2p excitation. Another green variant of wtGFP, GFP2, exhibited strong irreversible photoswitching from one sub-population (excitation state) to another, which are excited maximally by different wavelengths. This photoswitching effect significantly depends on the pH of the sample. In the case of cyan variants of wtGFP, mCerulean3 and mTq showed high propensities to photobleach with no significant effect of photoswitching. Another Cyan FP (but derived from CFP484 [4], mTFP1, is the brightest among the measured FPs in this investigation. In contrast, the yellow variants of the wtGFP measured in our investigation, namely mYFP, SYFP2, and Citrine, showed a small effect of photobleaching with essentially no effect of photoswitching under 2p excitations. This entire

subclass is more stable but dimmer compared to both the green and cyan variants tested in this study.

Our study adds to the body of evidence that the specific photophysical properties of fluorescent proteins under two-photon excitation, including excitation and emission spectra, as well as their propensity to undergo light-induced changes, may not be simply inferred from one-photon excitation. A lack of knowledge or appreciation of such properties may lead to erroneous conclusions in, for example, FRET studies [80]. Therefore, the choice of fluorescent proteins for a particular experiment depends, among other things, on whether one uses single- or two-photon excitation.

5.2. Conclusions regarding the effect of photobleaching on FRET measurements

In the investigation presented in Chapter 4, we measured the fluorescence from dimeric (NDA and ADN) and trimeric (ADA) FRET constructs expressed in the cytoplasm of CHO cells [135]. This was performed under two-photon excitation using various excitation wavelengths and powers. This methodological approach enabled us to explore the effect of photobleaching on FRET measurement under various experimental conditions, thereby assisting to establish optimize experimental conditions for the accurate for FRET measurement. Along with the measurements, we performed numerical simulation to see how FRET and the kinetic theory of FRET respond to the photophysical effects of participating FPs.

Our findings highlight the critical impact of the excitation power on the accuracy in the determination of FRET efficiency; at high excitation powers (above 42 mW/point), high photobleaching of both donor and acceptor during the first excitation was a major factor. This

led to a decrease of the FRET efficiency with increasing the excitation power. In the single-wavelength method, donor photobleaching can increase the number of free acceptors, potentially raising the FRET efficiency due to direct excitation. However, increased power also causes more acceptor photobleaching due to FRET, which tends to reduce FRET efficiency. In contrast, in dual-excitation method, corrections were made for the possible overestimation of FRET value caused by the direct excitation of acceptor. As a result, the acceptor photobleaching at the first excitation wavelength led to a decrease in FRET efficiency as the excitation power increased. The decrease in FRET efficiency observed in the dual-wavelength excitation method suggests an apparent increase in the distance between donor and acceptor molecules, especially at powers above 42 mW/point. Therefore, at higher excitation power, where photobleaching is more pronounced, the inferred size of the oligomer under study appears bigger than its actual size.

Our study also emphasizes the importance of selecting optimal excitation wavelengths. Exciting at 800 nm minimizes both acceptor and donor photobleaching compared to 880 nm, while 800 nm/960 nm pair yield the most consistent FRET efficiency under varying excitation powers.

Furthermore, our experimental results showed that even at higher excitation powers, the discrepancy between the directly measured FRET efficiency values for the trimeric construct (ADA) and that computed from its dimeric counterparts using the kinetic theory of FRET remains consistent, indicating a proportional decrease in FRET efficiency due to photobleaching for both the dimeric and trimeric constructs. The observed discrepancy between measured and predicted FRET efficiency across all excitation pairs using the dual-wavelength method is less than 2% for all excitation powers. Even with the single-wavelength excitation

method, the maximum discrepancy we observed was ~ 4.4% at a high excitation power of ~62 mW/point; however, for other used powers, the discrepancy was typically within 3.5%. Despite significant fluctuations in FRET efficiencies, the relationships between trimeric and dimeric construct efficiencies remained the same.

5.3. Suggestions for future research

Gowing forward, besides using low excitation powers, photobleaching may be reduced by reducing the dwell time of the excitation beam and developing fluorescent tags with better photostability. The present study also highlighted the importance of selecting the right excitation wavelengths. Excitation at 800 nm minimized direct excitation of the acceptor (Venus) while still efficiently exciting the donor (Cerulean). In contrast, the simulations indicated that the photobleaching of the donor and acceptor was relatively high when using 880 nm as the first excitation wavelength compared to 800 nm. Furthermore, while results from the dual-wavelength excitation method confirmed a consistent trend of decreasing FRET efficiency with higher excitation power across all excitation wavelength pairs, the pair 800 nm/960 nm showed the most consistent overall weighted average FRET efficiency.

Another path forward would be to extend the kinetic theory of FRET by incorporating photobleaching rates in addition to spontaneous emission and energy transfer rates, so that one can tease apart the contributions of these effects to the FRET efficiencies determined from data affected by photobleaching. Once available, the expanded theory could be used together with methods described above for reducing photobleaching or just by itself. Such a theoretical undertaking will require a good understanding of all the photophysical and photochemical phenomena involved. This process, while initiated through the computer simulations presented

in this thesis, needs more rigorous treatment in the future and will benefit from analysis of existing [153, 154] and future experimental studies. This will allow experimentalists to use the theory as a means of obtaining more accurate results from experiments rather than as a tool for assessing the errors introduced by harsh experimental conditions.

References

1. Shimomura, O., F.H. Johnson, and Y. Saiga, *Extraction, purification and properties of aequorin, a bioluminescent protein from the luminous hydromedusan, Aequorea.* Journal of cellular and comparative physiology, 1962. **59(3)**(1962): p. 223-239.
2. Tsien, R.Y., *The green fluorescent protein.* Annual Review of Biochemistry, 1998. **67**: p. 509-544.
3. Matz, M.V., et al., *Fluorescent proteins from nonbioluminescent Anthozoa species.* Nature Biotechnology, 1999. **17**(10): p. 969-973.
4. Ai, H.W., et al., *Directed evolution of a monomeric, bright and photostable version of Clavularia cyan fluorescent protein: structural characterization and applications in fluorescence imaging.* Biochemical Journal, 2006. **400**: p. 531-540.
5. Raicu, V., et al., *Protein interaction quantified in vivo by spectrally resolved fluorescence resonance energy transfer.* Biochemical Journal, 2005. **385**: p. 265-277.
6. Paprocki, J., et al., *In-Cell Detection of Conformational Substates of a G Protein-Coupled Receptor Quaternary Structure: Modulation of Substate Probability by Cognate Ligand Binding.* Journal of Physical Chemistry B, 2020. **124**(45): p. 10062-10076.
7. Stoneman, M.R., et al., *Fluorescence-based Methods for the Study of Protein-Protein Interactions Modulated by Ligand Binding.* Current Pharmaceutical Design, 2020. **26**(44): p. 5668-5683.
8. Raicu, V. and D.R. Singh, *FRET Spectrometry: A New Tool for the Determination of Protein Quaternary Structure in Living Cells.* Biophysical Journal, 2013. **105**(9): p. 1937-1945.
9. Mishra, A.K., et al., *Quaternary structures of opsin in live cells revealed by FRET spectrometry.* Biochemical Journal, 2016. **473**: p. 3819-3836.
10. Stoneman, M.R., et al., *Quaternary structure of the yeast pheromone receptor Ste2 in living cells.* Biochimica Et Biophysica Acta-Biomembranes, 2017. **1859**(9): p. 1456-1464.
11. Mastop, M., et al., *Characterization of a spectrally diverse set of fluorescent proteins as FRET acceptors for mTurquoise2.* Scientific Reports, 2017. **7**.
12. Drobizhev, M., et al., *Two-photon absorption properties of fluorescent proteins.* Nature Methods, 2011. **8**(5): p. 393-399.
13. Heppert, J.K., et al., *Comparative assessment of fluorescent proteins for in vivo imaging in an animal model system.* Molecular Biology of the Cell, 2016. **27**(22): p. 3385-3394.
14. Adhikari, D.P., et al., *Comparative photophysical properties of some widely used fluorescent proteins under two-photon excitation conditions.* Spectrochimica Acta Part A: Molecular and Biomolecular Spectroscopy, 2021. **262**: p. 120133.
15. Shimomura, O., *Structure of the chromophore of Aequorea green fluorescent protein.* FEBS letters, 1979. **104**(2): p. 220-222.
16. Ward, W.W., et al., *Spectral perturbations of the Aequorea green-fluorescent protein.* Photochemistry and Photobiology, 1982. **35**(6): p. 803-808.
17. Cody, C.W., et al., *Chemical structure of the hexapeptide chromophore of the Aequorea green-fluorescent protein.* Biochemistry, 1993. **32**(5): p. 1212-1218.
18. Prasher, D.C., et al., *Primary Structure of the Aequorea-Victoria Green-Fluorescent Protein.* Gene, 1992. **111**(2): p. 229-233.
19. Chalfie, M., et al., *Green Fluorescent Protein as a Marker for Gene-Expression.* Science, 1994. **263**(5148): p. 802-805.
20. Liu, H.-S., et al., *Is green fluorescent protein toxic to the living cells?* Biochemical and biophysical research communications, 1999. **260**(3): p. 712-717.
21. Haseloff, J., *GFP variants for multispectral imaging of living cells.* Methods in cell biology, 1998. **58**: p. 139-151.

22. Chiu, W.-l., et al., *Engineered GFP as a vital reporter in plants.* Current Biology, 1996. **6**(3): p. 325-330.
23. Ormö, M., et al., *Crystal structure of the Aequorea victoria green fluorescent protein.* Science, 1996. **273**(5280): p. 1392-1395.
24. Yang, F., L.G. Moss, and G.N. Phillips, *The molecular structure of green fluorescent protein.* Nature biotechnology, 1996. **14**(10): p. 1246-1251.
25. Heim, R., D.C. Prasher, and R.Y. Tsien, *Wavelength Mutations and Posttranslational Autoxidation of Green Fluorescent Protein.* Proceedings of the National Academy of Sciences of the United States of America, 1994. **91**(26): p. 12501-12504.
26. Cubitt, A.B., et al., *Understanding, Improving and Using Green Fluorescent Proteins.* Trends in Biochemical Sciences, 1995. **20**(11): p. 448-455.
27. Morise, H., et al., *Intermolecular energy transfer in the bioluminescent system of Aequorea.* Biochemistry, 1974. **13**(12): p. 2656-2662.
28. Prasher, D.C., *Using GFP to see the light.* Trends in Genetics, 1995. **11**(8): p. 320-323.
29. Chudakov, D.M., et al., *Fluorescent proteins and their applications in imaging living cells and tissues.* Physiological reviews, 2010. **90**(3): p. 1103-1163.
30. Zhang, G., V. Gurtu, and S.R. Kain, *An enhanced green fluorescent protein allows sensitive detection of gene transfer in mammalian cells.* Biochemical and biophysical research communications, 1996. **227**(3): p. 707-711.
31. Chen, Y., et al., *Molecular brightness characterization of EGFP in vivo by fluorescence fluctuation spectroscopy.* Biophysical journal, 2002. **82**(1): p. 133-144.
32. Wachter, R.M., et al., *Structural basis of spectral shifts in the yellow-emission variants of green fluorescent protein.* Structure, 1998. **6**(10): p. 1267-1277.
33. Dickson, R.M., et al., *On/off blinking and switching behaviour of single molecules of green fluorescent protein.* Nature, 1997. **388**(6640): p. 355-358.
34. Miyawaki, A. and R.Y. Tsien, *Monitoring protein conformations and interactions by fluorescence resonance energy transfer between mutants of green fluorescent protein.* Methods in enzymology, 2000. **327**: p. 472-500.
35. Griesbeck, O., et al., *Reducing the environmental sensitivity of yellow fluorescent protein - Mechanism and applications.* Journal of Biological Chemistry, 2001. **276**(31): p. 29188-29194.
36. Llopis, J., et al., *Measurement of cytosolic, mitochondrial, and Golgi pH in single living cells with green fluorescent proteins.* Proceedings of the National Academy of Sciences, 1998. **95**(12): p. 6803-6808.
37. Miyawaki, A., et al., *Dynamic and quantitative Ca2+ measurements using improved cameleons.* Proceedings of the National Academy of Sciences, 1999. **96**(5): p. 2135-2140.
38. Shaner, N.C., P.A. Steinbach, and R.Y. Tsien, *A guide to choosing fluorescent proteins.* Nature Methods, 2005. **2**(12): p. 905-909.
39. Goedhart, J., et al., *Structure-guided evolution of cyan fluorescent proteins towards a quantum yield of 93%.* Nature communications, 2012. **3**(1): p. 1-9.
40. Lelimousin, M., et al., *Intrinsic dynamics in ECFP and Cerulean control fluorescence quantum yield.* Biochemistry, 2009. **48**(42): p. 10038-10046.
41. Patterson, G., R.N. Day, and D. Piston, *Fluorescent protein spectra.* Journal of Cell Science, 2001. **114**(5): p. 837-838.
42. Chudakov, D.M., et al., *Photoswitchable cyan fluorescent protein for protein tracking.* Nature Biotechnology, 2004. **22**(11): p. 1435-1439.
43. Kneen, M., et al., *Green fluorescent protein as a noninvasive intracellular pH indicator.* Biophysical Journal, 1998. **74**(3): p. 1591-1599.
44. Elsliger, M.-A., et al., *Structural and spectral response of green fluorescent protein variants to changes in pH.* Biochemistry, 1999. **38**(17): p. 5296-5301.
45. Lammich, L., et al., *The gas-phase absorption spectrum of a neutral GFP model chromophore.* Biophysical journal, 2007. **92**(1): p. 201-207.

46. Terry, B., E. Matthews, and J. Haseloff, *Molecular characterization of recombinant green fluorescent protein by fluorescence correlation microscopy.* Biochemical and biophysical research communications, 1995. **217**(1): p. 21-27.
47. von Stetten, D., et al., *Structure of a fluorescent protein from Aequorea victoria bearing the obligate-monomer mutation A206K.* Acta Crystallographica Section F: Structural Biology and Crystallization Communications, 2012. **68**(8): p. 878-882.
48. Brejc, K., et al., *Structural basis for dual excitation and photoisomerization of the Aequorea victoria green fluorescent protein.* Proceedings of the National Academy of Sciences of the United States of America, 1997. **94**(6): p. 2306-2311.
49. Nienhaus, K. and G.U. Nienhaus, *Chromophore photophysics and dynamics in fluorescent proteins of the GFP family.* Journal of Physics-Condensed Matter, 2016. **28**(44).
50. Duan, C.X., et al., *Structural Evidence for a Two-Regime Photobleaching Mechanism in a Reversibly Switchable Fluorescent Protein.* Journal of the American Chemical Society, 2013. **135**(42): p. 15841-15850.
51. Patterson, G.H., D.W. Piston, and B.G. Barisas, *Förster distances between green fluorescent protein pairs.* Analytical biochemistry, 2000. **284**(2): p. 438-440.
52. Zimmermann, T., et al., *Spectral imaging and linear un-mixing enables improved FRET efficiency with a novel GFP2-YFP FRET pair.* Febs Letters, 2002. **531**(2): p. 245-249.
53. Shaner, N.C., *Fluorescent proteins for quantitative microscopy: Important properties and practical evaluation.* Quantitative Imaging in Cell Biology, 2014. **123**: p. 95-111.
54. Rizzo, M.A., et al., *Optimization of pairings and detection conditions for measurement of FRET between cyan and yellow fluorescent proteins.* Microscopy and microanalysis, 2006. **12**(3): p. 238-254.
55. Kremers, G.J., et al., *Cyan and yellow super fluorescent proteins with improved brightness, protein folding, and FRET Forster radius.* Biochemistry, 2006. **45**(21): p. 6570-6580.
56. Goedhart, J., et al., *Sensitive detection of p65 homodimers using red-shifted and fluorescent protein-based FRET couples.* PLoS One, 2007. **2**(10): p. e1011.
57. Markwardt, M.L., et al., *An Improved Cerulean Fluorescent Protein with Enhanced Brightness and Reduced Reversible Photoswitching.* Plos One, 2011. **6**(3): p. e17896.
58. Goedhart, J., et al., *Bright cyan fluorescent protein variants identified by fluorescence lifetime screening.* Nature Methods, 2010. **7**(2): p. 137-U74.
59. Lam, A.J., et al., *Improving FRET dynamic range with bright green and red fluorescent proteins.* Nature Methods, 2012. **9**(10): p. 1005-+.
60. Lakowicz, J.R., *Principles of fluorescence spectroscopy.* Springer Science & Business Media, 2013.
61. Masters, B., *Paths to Förster's resonance energy transfer (FRET) theory.* The European Physical Journal H, 2014. **39**(1): p. 87-139.
62. Főrster, T., *10th Spiers Memorial Lecture. Transfer mechanisms of electronic excitation.* Discussions of the Faraday Society, 1959. **27**: p. 7-17.
63. Perrin, J. and N. Choucroun, *Fluorescence sensibilisée en milieu liquide (transferts d'activation par induction moléculaire).* CR hebd Séances Acad Sci, 1929. **189**: p. 1213-1216.
64. Förster, T., *Energy migration and fluorescence [Energiewanderung und fluoreszenz].* Naturwissenschaften, 1946. **33.166-177**.
65. Stryer, L., *Fluorescence energy transfer as a spectroscopic ruler.* Annual Review of Biochemistry, 1978. **47:819-846**.
66. Raicu, V., et al., *Determination of supramolecular structure and spatial distribution of protein complexes in living cells.* Nature Photonics, 2009. **3**(2): p. 107-113.
67. Clegg, R., *Fluorescence resonance energy transfer.* Fluorescence imaging spectroscopy and microscopy, 1996. **137**: p. 179-251.

68. Deniz, A.A., et al., *Single-pair fluorescence resonance energy transfer on freely diffusing molecules: observation of Förster distance dependence and subpopulations.* Proceedings of the National Academy of Sciences, 1999. **96**(7): p. 3670-3675.
69. Medintz, I.L. and N. Hildebrandt, *FRET-Förster Resonance Energy Transfer: From Theory to Applications*. 2013: John Wiley & Sons.
70. Raicu, V. and A. Popescu, *Integrated molecular and cellular biophysics*. Vol. 10. 2008: Springer.
71. Ma, L., F. Yang, and J. Zheng, *Application of fluorescence resonance energy transfer in protein studies.* Journal of molecular structure, 2014. **1077**: p. 87-100.
72. Perrin, J., et al., *CR Acad Sci.* Paris, 1927. **184**: p. 1097.
73. Iqbal, A., et al., *Orientation dependence in fluorescent energy transfer between Cy3 and Cy5 terminally attached to double-stranded nucleic acids.* Proceedings of the National Academy of Sciences, 2008. **105**(32): p. 11176-11181.
74. Jackson, J.D., *Classical electrodynamics*. 1999, American Association of Physics Teachers.
75. Förster, T., *Zwischenmolekulare energiewanderung und fluoreszenz.* Annalen der physik, 1948. **437**(1-2): p. 55-75.
76. Dirac, P.A.M., *The quantum theory of the emission and absorption of radiation.* Proceedings of the Royal Society of London. Series A, Containing Papers of a Mathematical and Physical Character, 1927. **114**(767): p. 243-265.
77. Valeur, B. and M.N. Berberan-Santos, *Molecular fluorescence: principles and applications*. 2012: John Wiley & Sons.
78. Shankar, R., *Principles of quantum mechanics*. 2012: Springer Science & Business Media.
79. Singh, D.R., *Investigation of the quaternary structure of an ABC transporter in living cells using spectrally resolved resonance energy transfer*. 2012, The University of Wisconsin-Milwaukee.
80. Raicu, V., *Ab inito derivation of the FRET equations resolves old puzzles and suggests measurement strategies.* Biophysical Journal, 2019. **116, 1313-1327**.
81. Raicu, V., *Extraction of information on macromolecular interactions from fluorescence micro-spectroscopy measurements in the presence and absence of FRET.* Spectrochimica Acta Part A: Molecular and Biomolecular Spectroscopy, 2018. **199**: p. 340-348.
82. Mishra, A.K., et al., *Quaternary structures of opsin in live cells revealed by FRET spectrometry.* Biochem. J., 2016. **473**: p. 3819-3836.
83. King, C., et al., *Fully quantified spectral imaging reveals in vivo membrane protein interactions.* Integr. Biol., 2016. **8**: p. 216-229.
84. Stoneman, M.R., et al., *Quaternary structure of the yeast pheromone receptor Ste2 in living cells.* Biochim. Biophys. Acta Biomembr. , 2016. **12**(008): p. 1456-1464.
85. Raicu, V., *Efficiency of resonance energy transfer in homo-oligomeric complexes of proteins.* Journal of Biological Physics, 2007. **33**(2): p. 109-127.
86. Raicu, V., *Ab initio derivation of the FRET equations resolves old puzzles and suggests measurement strategies.* Biophys. J., 2019. **116**(7): p. 1313-1327.
87. Koushik, S.V., P.S. Blank, and S.S. Vogel, *Anomalous Surplus Energy Transfer Observed with Multiple FRET Acceptors.* Plos One, 2009. **4**(11).
88. Patowary, S., et al., *Experimental Verification of the Kinetic Theory of FRET Using Optical Microspectroscopy and Obligate Oligomers.* Biophysical Journal, 2015. **108**(7): p. 1613-1622.
89. King, C., V. Raicu, and K. Hristova, *Understanding the FRET Signatures of Interacting Membrane Proteins.* Journal of Biological Chemistry, 2017. **292**(13): p. 5291-5310.
90. Veatch, W. and L. Stryer, *The dimeric nature of the gramicidin A transmembrane channel: conductance and fluorescence energy transfer studies of hybrid channels.* Journal of molecular biology, 1977. **113**(1): p. 89-102.
91. Biener, G., et al., *Development and Experimental Testing of an Optical Micro-Spectroscopic Technique Incorporating True Line-Scan Excitation.* International Journal of Molecular Sciences, 2014. **15**(1): p. 261-276.

92. Zinchuk, V., O. Zinchuk, and T. Okada, *Quantitative colocalization analysis of multicolor confocal immunofluorescence microscopy images: Pushing pixels to explore biological phenomena.* Acta Histochemica Et Cytochemica, 2007. **40**(4): p. 101-111.
93. Ariotti, N., et al., *Modular Detection of GFP-Labeled Proteins for Rapid Screening by Electron Microscopy in Cells and Organisms.* Developmental Cell, 2015. **35**(4): p. 513-525.
94. Singh, D.R., et al., *The EphA2 receptor is activated through induction of distinct, ligand-dependent oligomeric structures (vol 1, 15, 2018).* Communications Biology, 2018. **1**.
95. King, C., et al., *Fully quantified spectral imaging reveals in vivo membrane protein interactions.* Integrative Biology, 2016. **8**(2): p. 216-229.
96. Vu, V., et al., *P120 catenin potentiates constitutive E-cadherin dimerization at the plasma membrane and regulates trans binding.* Current Biology, 2021.
97. Jares-Erijman, E.A. and T.M. Jovin, *FRET imaging.* Nature Biotechnology, 2003. **21**(11): p. 1387-1395.
98. Shivnaraine, R.V., et al., *Single-Molecule Analysis of the Supramolecular Organization of the M-2 Muscarinic Receptor and the G alpha(i1) Protein.* Journal of the American Chemical Society, 2016. **138**(36): p. 11583-11598.
99. Chen, Y., et al., *Molecular counting by photobleaching in protein complexes with many subunits: best practices and application to the cellulose synthesis complex.* Molecular Biology of the Cell, 2014. **25**(22): p. 3630-3642.
100. Wang, Z.F., et al., *Fluorescence correlation spectroscopy investigation of a GFP mutant-enhanced cyan fluorescent protein and its tubulin fusion in living cells with two-photon excitation.* Journal of Biomedical Optics, 2004. **9**(2): p. 395-403.
101. Stoneman MR, Biener G, Ward RJ, Pediani JD, Badu D, Eis A, Popa I, Milliagn G, Raicu V., *A general method to quantify lignad-driven oligomerization from fluorescence-based images.* Nat Methods, 2019. **16**(JUNE 2019): p. 493-496.
102. Cotlet, M., et al., *A comparison of the fluorescence dynamics of single molecules of a green fluorescent protein: One- versus two-photon excitation.* Chemphyschem, 2006. **7**(1): p. 250-260.
103. Grecco, H.E., et al., *Ensemble and single particle photophysical proper-ties (Two-Photon excitation, anisotropy, FRET, lifetime, spectral conversion) of commercial quantum dots in solution and in live cells.* Microscopy Research and Technique, 2004. **65**(4-5): p. 169-179.
104. Drobizhev, M., et al., *Absolute Two-Photon Absorption Spectra and Two-Photon Brightness of Orange and Red Fluorescent Proteins.* Journal of Physical Chemistry B, 2009. **113**(4): p. 855-859.
105. Grigorenko, B.L., et al., *A Light-Induced Reaction with Oxygen Leads to Chromophore Decomposition and Irreversible Photobleaching in GFP-Type Proteins.* Journal of Physical Chemistry B, 2015. **119**(17): p. 5444-5452.
106. Bernas, T., et al., *Loss of image quality in photobleaching during microscopic imaging of fluorescent probes bound to chromatin.* Journal of Biomedical Optics, 2005. **10**(6): p. 064015.
107. Zhou, X.X. and M.Z. Lin, *Photoswitchable fluorescent proteins: ten years of colorful chemistry and exciting applications.* Current Opinion in Chemical Biology, 2013. **17**(4): p. 682-690.
108. Lippincott-Schwartz, J. and G.H. Patterson, *Photoactivatable fluorescent proteins for diffraction-limited and super-resolution imaging.* Trends in Cell Biology, 2009. **19**(11): p. 555-565.
109. Bourgeois, D. and V. Adam, *Reversible photoswitching in fluorescent proteins: A mechanistic view.* Iubmb Life, 2012. **64**(6): p. 482-491.
110. Lukyanov, K.A., et al., *Photoactivatable fluorescent proteins.* Nature Reviews Molecular Cell Biology, 2005. **6**(11): p. 885-891.
111. van Thor, J.J., et al., *Characterization of the photoconversion of green fluorescent protein with FTIR spectroscopy.* Biochemistry, 1998. **37**(48): p. 16915-16921.

112. Ahmed, F., et al., *The Biased Ligands NGF and NT-3 Differentially Stabilize Trk-A Dimers.* Biophysical Journal, 2021. **120**(1): p. 55-63.
113. Krichevsky, O. and G. Bonnet, *Fluorescence correlation spectroscopy: the technique and its applications.* Reports on Progress in Physics, 2002. **65**(2): p. 251-297.
114. Widengren, J. and R. Rigler, *Review - Fluorescence correlation spectroscopy as a tool to investigate chemical reactions in solutions and on cell surfaces.* Cellular and Molecular Biology, 1998. **44**(5): p. 857-879.
115. Stoneman, M.R., G. Biener, and V. Raicu, *Reply to: Spatial heterogeneity in molecular brightness.* Nature Methods, 2020. **17**(3): p. 276-278.
116. Sprague, B.L. and J.G. McNally, *FRAP analysis of binding: proper and fitting.* Trends in Cell Biology, 2005. **15**(2): p. 84-91.
117. Chudakov, D.M., S. Lukyanov, and K.A. Lukyanov, *Tracking intracellular protein movements using photoswitchable fluorescent proteins PS-CFP2 and Dendra2.* Nature Protocols, 2007. **2**(8): p. 2024-2032.
118. Adam, V., et al., *Data storage based on photochromic and photoconvertible fluorescent proteins.* Journal of Biotechnology, 2010. **149**(4): p. 289-298.
119. Cranfill, P.J., et al., *Quantitative assessment of fluorescent proteins.* Nature Methods, 2016. **13**(7): p. 557-562.
120. Haubert, K., T. Drier, and D. Beebe, *PDMS bonding by means of a portable, low-cost corona system.* Lab on a Chip, 2006. **6**(12): p. 1548-1549.
121. Stoneman, M., et al., *Real-time monitoring of two-photon photopolymerization for use in fabrication of microfluidic devices.* Lab on a Chip, 2009. **9**(6): p. 819-827.
122. Cormack, B.P., R.H. Valdivia, and S. Falkow, *FACS-optimized mutants of the green fluorescent protein (GFP).* Gene, 1996. **173**(1): p. 33-38.
123. Zacharias, D.A., et al., *Partitioning of lipid-modified monomeric GFPs into membrane microdomains of live cells.* Science, 2002. **296**(5569): p. 913-916.
124. Dickson, R.M., et al., *Three-dimensional imaging of single molecules solvated in pores of poly(acrylamide) gels.* Science, 1996. **274**(5289): p. 966-969.
125. Weber, K. and M. Osborn, *SDS-PAGE to determine the molecular weight of proteins: The work of Klaus Weber and Mary Osborn - The reliability of molecular weight determinations by dodecyl sulfate-polyacrylamide gel electrophoresis (reprinted from J.Biol. Chem. vol. 244, pg. 4406-4412, 1969).* Journal of Biological Chemistry, 2006. **281**(24).
126. Marsango, S., et al., *A Molecular Basis for Selective Antagonist Destabilization of Dopamine D-3 Receptor Quaternary Organization.* Scientific Reports, 2017. **7**(1): p. 1-17.
127. Ward, R.J., et al., *Chemokine receptor CXCR4 oligomerization is disrupted selectively by the antagonist ligand IT1t.* Journal of Biological Chemistry, 2021. **296**: p. 100139.
128. McAnaney, T.B., et al., *Protonation, photobleaching, and photoactivation of yellow fluorescent protein (YFP 10C): A unifying mechanism.* Biochemistry, 2005. **44**(14): p. 5510-5524.
129. Patterson, G.H. and J. Lippincott-Schwartz, *A photoactivatable GFP for selective photolabeling of proteins and cells.* Science, 2002. **297**(5588): p. 1873-1877.
130. Heim, R., A.B. Cubitt, and R.Y. Tsien, *Improved Green Fluorescence.* Nature, 1995. **373**(6516): p. 663-664.
131. Ai, H.W., et al., *Hue-shifted monomeric variants of Clavularia cyan fluorescent protein: identification of the molecular determinants of color and applications in fluorescence imaging.* Bmc Biology, 2008. **6**.
132. Day, R.N. and M.W. Davidson, *The fluorescent protein palette: tools for cellular imaging.* Chemical Society Reviews, 2009. **38**(10): p. 2887-2921.
133. Parsons, M., B. Vojnovic, and S. Ameer-Beg, *Imaging protein-protein interactions in cell motility using fluorescence resonance energy transfer (FRET).* Biochemical Society Transactions, 2004. **32**: p. 431-433.

134. James, N.G., et al., *Number and Brightness Analysis of LRRK2 Oligomerization in Live Cells.* Biophysical Journal, 2012. **102**(11): p. A41-A43.
135. Adhikari, D.P., M.R. Stoneman, and V. Raicu, *Impact of photobleaching of fluorescent proteins on FRET measurements under two-photon excitation.* bioRxiv, 2024.
136. Gonzalez, J.E. and R.Y. Tsien, *Voltage Sensing by Fluorescence Resonance Energy-Transfer in Single Cells.* Biophysical Journal, 1995. **69**(4): p. 1272-1280.
137. Chen, Q. and B.R. Lentz, *Fluorescence resonance energy transfer study of shape changes in membrane-bound bovine prothrombin and meizothrombin.* Biochemistry, 1997. **36**(15): p. 4701-4711.
138. An, S.J. and W. Almers, *Tracking SNARE complex formation in live endocrine cells.* Science, 2004. **306**(5698): p. 1042-1046.
139. Demarco, I.A., et al., *Monitoring dynamic protein interactions with photoquenching FRET.* Nature Methods, 2006. **3**(7): p. 519-524.
140. Pearce, L.L., et al., *Role of metallothionein in nitric oxide signaling as revealed by a green fluorescent fusion protein.* Proceedings of the National Academy of Sciences of the United States of America, 2000. **97**(1): p. 477-482.
141. Hink, M.A., T. Bisseling, and A.J.W.G. Visser, *Imaging protein-protein interactions in living cells.* Plant Molecular Biology, 2002. **50**(6): p. 871-883.
142. Heyduk, T., *Measuring protein conformational changes by FRET/LRET.* Current Opinion in Biotechnology, 2002. **13**(4): p. 292-296.
143. Mishra, A., et al., *Determination of Quaternary Structure of Rhodopsin at Room and Body Temperature using Spectral FRET.* Biophysical Journal, 2013. **104**(2): p. 577a-577a.
144. Singh, D.R., et al., *Determination of the quaternary structure of a bacterial ATP-binding cassette (ABC) transporter in living cells.* Integrative Biology, 2013. **5**(2): p. 312-323.
145. Loing, S.H.E.J., Young, I. T., Tank, H. J., *Photobleaching Kinetics of Fluorescein in Quantitative Fluorescence Microscoph.* Biophysical Journal, 1995. **68**.
146. Mongin, O., et al., *Synthesis and photophysical properties of new conjugated fluorophores designed for two-photon-excited fluorescence.* Organic Letters, 2002. **4**(5): p. 719-722.
147. Chen, H., H.L. Puhl III, and S.R. Ikeda, *Estimating protein-protein interaction affinity in living cells using quantitative Förster resonance energy transfer measurements.* Journal of biomedical optics, 2007. **12**(5): p. 054011.
148. Koushik, S.V., et al., *Cerulean, Venus, and Venus(Y67C) FRET reference standards.* Biophysical Journal, 2006. **91**(12): p. L99-L101.
149. Trujillo, J., et al., *Implementation of FRET Spectrometry Using Temporally Resolved Fluorescence: A Feasibility Study.* International Journal of Molecular Sciences, 2024. **25**(9).
150. Pisterzi, L.F., et al., *Oligomeric size of the m2 muscarinic receptor in live cells as determined by quantitative fluorescence resonance energy transfer.* Journal of Biological Chemistry, 2010. **285**(22): p. 16723-16738.
151. Rizzo, M.A., et al., *An improved cyan fluorescent protein variant useful for FRET.* Nature Biotechnology, 2004. **22**(4): p. 445-449.
152. Nagai, T., et al., *A variant of yellow fluorescent protein with fast and efficient maturation for cell-biological applications.* Nature Biotechnology, 2002. **20**(1): p. 87-90.
153. Kong, X.X., et al., *Photobleaching pathways in single-molecule FRET experiments.* Journal of the American Chemical Society, 2007. **129**(15): p. 4643-4654.
154. Eggeling, C., et al., *Analysis of photobleaching in single-molecule multicolor excitation and Förster resonance energy transfer measurements.* The Journal of Physical Chemistry A, 2006. **110**(9): p. 2979-2995.
155. Stoneman, M.R. and V. Raicu, *Fluorescence-Based Detection of Proteins and Their Interactions in Live Cells.* Journal of Physical Chemistry B, 2023. **127**(21): p. 4708-4721.